August 2020

Anti-plane Shear of Cylinders and Layered Systems: Cohesive Fracture and Instability

yueming song
Syracuse University

Recommended Citation

song, yueming, "Anti-plane Shear of Cylinders and Layered Systems: Cohesive Fracture and Instability" (2020). *Dissertations - ALL*. 1273.
https://surface.syr.edu/etd/1273

Abstract

This research examines the mechanics of mode-III cohesive fracture by defect initiation and quasi-static growth in both cylinder and layered systems. The analysis, which is exact, is based on the solution of two fundamental elasticity problems: i) a cylinder subject to an arbitrary shear on one end cap and an equilibrating torque on the other and, ii) a layer subject to arbitrary anti-plane shear traction on one surface and an equilibrating uniform traction on the other. For a particular geometry and defect configuration, these solutions are shown to lead to a pair of interfacial integral equations whose derived cohesive surface fields capture the entire defect evolution process from incipient growth through complete failure. The anti-plane shear separation/slip process is assumed to be modeled by Needleman-type traction-separation relations (e.g., bilinear, Xu-Needleman, frictional) characterized by a *shear cohesive strength*, a *characteristic force length* and, in the case of the bilinear law, a finite *decohesion cutoff length* and possibly other parameters as well. Symmetrically arrayed cohesive surface defects are modeled by a cohesive surface strength function which varies with surface coordinate. Infinitesimal strain equilibrium solutions, which allow for rigid body movement, are found by eigenfunction approximation of the solution of the governing interfacial integral equations.

General features of the solutions to anti-plane shear cohesive fracture in both cylindrical and layered geometries indicate that quasi-static defect initiation and propagation occur under monotonically increasing load. For small values of characteristic force length, brittle behavior occurs that is readily identifiable with the growth of a sharp crack, i.e., the existence of a strong local stress concentration. At larger values of characteristic force length, ductile response occurs which is more typical of a linear "spring" cohesive surface, i.e., more distributed stress and slip distribution. Both behaviors ultimately give rise to abrupt failure of the cohesive surface. Results

for the stiff, strong cohesive surface under a small applied load show consistency with static linear elastic fracture mechanics solutions in the literature. By superimposing a frictional part onto the cohesive law, the solution can be used to predict frictional response. Both decohesion and friction dominated cases show similar quasi-static defect propagation process, stable defect growth till a maximum load is reached, then defect growth becomes dynamic and unstable. However, the difference lies in that the friction dominated cohesive surface can still sustain certain load even after response becomes dynamic, but the decohesion dominated case will not. For friction dominated cohesive surfaces, the cylinder cases have smooth deformation processes whereas the layered systems experience a noticeable displacement jump. Both cylinder and layered systems predict the principal plane (perpendicular to principal stress direction) to be close to 45 degrees which helps to explain the orientation of mode-I microcracks in layered systems and the initiation of a spiral crack plane in cylinder geometries.

The cohesive fracture solution to layered geometries can be extended to obtaining traction fields for more complicated defect geometries (array of cracks and subsurface cracks in nonuniform bilayer) which can be used to predict the sequence of defect propagation. The bifurcation analysis of the uniform two-sublayer system shows the phenomenon of non-unique slip for the same loading. The bifurcation analysis for the multi-sublayer system with such non-uniqueness gives an explanation of the asymmetric configuration. For the analysis of nonuniform multi-sublayer systems, no additional difficulty occurs in the problem-solving process. By studying different geometries and crack patterns, the current study discussed the combined effects of interlaminar and intralaminar crack interaction which are important in predicting the most vulnerable place in the system while multiple defects exist.

Anti-plane Shear of Cylinders and Layered Systems: Cohesive Fracture and Instability

By
Yueming Song

B.S., Dalian University of Technology, 2014

Dissertation
Submitted in partial fulfillment of the requirements for the degree of
Doctor of Philosophy in *Mechanical and Aerospace Engineering*

Syracuse University
August 2020

Acknowledgements

Firstly, I would like to show my deepest gratitude to Dr. Alan Levy who has been an excellent academic advisor, life mentor and friend. His dedication to work, patience to colleagues and sincerity to friends encourage me to follow his example.

I also want to express my gratitude Dr. Barry Davidson, Dr. Eric Lui, Dr. Teng Zhang, Dr. Zhao Qin and Dr. Wanliang Shan for serving in my committee and overcoming all the difficulties and inconvenience in holding a defense through online meeting.

My achievement cannot be separated from the support of my family. They cultivated my desire to embrace other cultures, respected my choice of studying abroad and free me from all kinds of worries that most young people like me are dealing with.

I also want to thank all my friends and colleagues whoever helped me in my research or my daily life. I would like to give special thanks to Mengyi Zhang, a smart beautiful young lady with strong will, she greatly boosts the abundance and colorfulness of my life.

Finally, it is such an unforgettable memory to graduate during the COVID-19 pandemic. Even though there are inconvenience, pities and even disappointments, I hold the belief that knowledge will defeat ignorance, impartiality will overcome prejudice, truth will reveal lies, voice of reason will overwhelm irrationality. Despite all odds, we will defeat the virus and return to normal in the near future.

Table of Contents

1. Introduction

Fracture mechanics gained popularity during WWII to explain failures of high strength structures under relatively low loading conditions [1]. These failures cannot be explained from the point of view of strength of materials since many cases of failure happen at loads conditions well under the design conditions. It is believed that micro-defects formed during manufacturing, or under service, lead to local stress concentrations that are responsible for structural failure under conditions when failure seems unlikely from a traditional strength point of view. Despite different theories and criteria of fracture initiation and propagation (either stress based, or energy based), obtaining the stress field is almost always the first priority and the basis for calculating derived physical quantities that describe fracture. A theoretical study of cracks in solid media under general loading, begins with the idea that the stress field at the tip of a crack can be decomposed into three components (corresponding to three types of loading as shown in Fig.1.1). These are mode-I (opening mode, loading is normal to the primary crack plane), mode-II (in-plane shearing mode, loading is parallel to primary crack plane but normal to crack front) and mode-III (anti-plane shearing mode, loading is parallel to both primary crack plane and crack front). In order to develop fundamental and consistent theories for general loading conditions, it is important to obtain uncoupled material properties that describe the materials' ability to withstand a certain kind of loading. Note that except for mode-I fracture, the geometries and loadings given in Fig.1.1 cannot be used to produce uncoupled pure mode fracture testing. Of the three fracture modes, mode-III fracture has received less attention from the research community because i) fracture of most structures under general loading are mode-I or mode-II dominated and, relatively complicated testing platforms are needed to create mode-III dominated fracture without introducing significant effects from other modes [2], ii) mode-I and mode-II fracture can be reduced to two-dimensional problems in which both mathematical representation and numerical treatment are implemented without extra effort. However, mode-III problems are irreducible three-dimensional and difficult to be simplified. Problems such as the torsion of cylindrical shafts and layered composites, subjected to anti-plane shear traction are however mode-III dominated. Furthermore, due to the well-known difficulties of pure mode-III testing, exact analysis of this fracture mode is critical to interpreting mode-III and related mixed-mode experimental results.

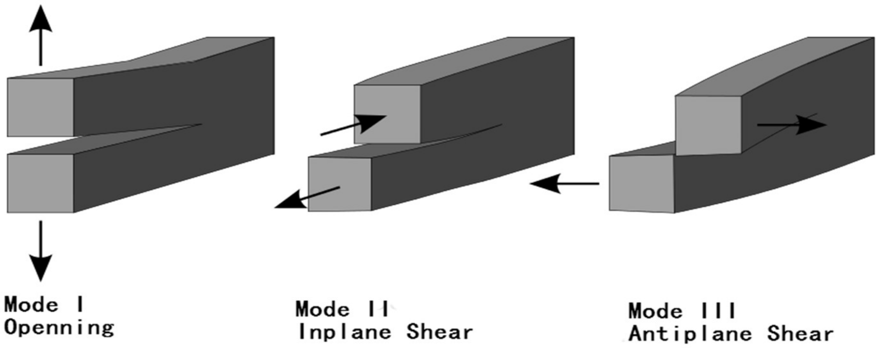

Fig.1.1 Fracture modes and relative loading direction [3].

A primary interest in the consideration of the macroscopic response of cracked structures is the critical load that leads to failure. Such analyses simplify the complicated phenomenon of detailed crack tip response by assuming the crack to be static and the crack tip to be well defined[1]. General methodologies for analyzing cracks include testing, theoretical and computational analyses of local crack tip fields, derivation and introduction of parameters for use in describing local fields and stable/unstable crack growth. Traditional linear elastic fracture mechanics (LEFM) concepts such as the stress intensity factor (SIF), the energy release rate (ERR), the crack tip opening displacement (CTOD) and the J-integral (of elastic "plastic" fracture) falls into this category [1]. However, the limitation of these methods includes, i) unphysical stress singularities, ii) restrictions to simple geometry and relatively simple material response, iii) difficulties in describing crack

---

[1] The term "crack" is used for the sharp crack of classical fracture mechanics; the term "defect" is used for the cohesive crack, i.e., the crack in the cohesive framework.

propagation processes, iv) derived quantities without real physical interpretation, etc. To resolve these issues, the cohesive zone was introduced by Barenblatt [4] based on the idea that the separation of material across a surface is governed by its own constitutive law relating force with the separation required to produce it. This kind of model, often micro-scale based, is applied to larger scales where they are interpreted phenomenologically. The cohesive fracture process is therefore governed by specific cohesive relations (cohesive force laws) that are analogous to the stress-strain relations of bulk material. The cohesive fracture framework seems to resolve many of the drawbacks of classical fracture mechanics of sharp cracks. However, cohesive fracture analysis has its own limitations such as requiring the primary fracture surface to be specified beforehand. The characterization of cohesive laws are not as straight forward and computational processes resulting from their use are often more complicated owing to the essential nonlinearity of the cohesive force laws. Because of this, much of the recent work involving CZM's uses finite element analysis (FEA). The work described in this document avoids the finite element method in favor of an exact elasticity approach. The goal is not to simulate the response of the most complicated material models and geometries, but to analyze in detail the essential mode-III cohesive fracture and stability behavior of linear elastic cylinders and layers containing single or multiple nonlinear fracture planes. The formulation presented reduces the analysis of cohesive fracture fields and stability issues to the solution of a set of nonlinear integral equations governing the interfacial separation/slip field. Where possible exact results are given and, for cases where they are not, an efficient method is developed to solve the integral equations numerically.

The following chapter (Chapter 2) is a literature review covering existing work relevant to the research outlined in this document, i.e., mode-III fracture (mostly the classical fracture theory and experimental results), an introduction to cohesive zone models and a review of certain aspects of linear and nonlinear integral equations and their use in cohesive fracture analysis. Chapters 3 to 5 presents novel solutions to two pure mode-III fracture problems: the cylindrical bar in torsion and the layered system subject to anti-plane shear traction. The basic approach is to solve the half cylinder and single sublayer component sub-problem exactly and derive the solution to interfacial integral equations governing cohesive fracture and stability behavior. The interfacial integral equations, which are necessarily nonlinear, are either solved exactly (e.g., the uniform cohesive surface or reduced by eigenfunction expansion (e.g., the nonuniform cohesive surface with initial defects) to a set of nonlinear algebraic equations which are then solved numerically by a program written by the author. Solutions are shown to govern a range of responses such as cohesive surface stability, ductile and brittle defect propagation, etc. When possible, the results are compared with classical sharp crack (SIF) results. Related issues such as mode-I micro cracking, multi-sublayer system cohesive surface stability, interlaminar and intralaminar crack interaction, crack propagation sequence and frictional cohesive surface response are analyzed and discussed as well.

2. Literature Review

2.1 Fracture mechanics in mode-III

Before presenting a new methodology, existing research is described to provide context and insight to the analysis of mode-III fracture. Traditional studies of fracture problems include, i) linear elastic fracture mechanics (LEFM) based static sharp crack solutions which generally produce the local stress field and introduce parameters that can be applied in an engineering sense for failure evaluation, ii) finite element simulations which can be easily set up at minimal cost compared to testing. It is very well suited to the analysis of more advanced problems such as elastic-plastic fracture, energy-based fracture, mixed-mode fracture, etc., iii) experimental work including bulk testing and materials characterization that reveals general behavior and microstructural details of the fracture surface. In this section, the application of these three approaches to mode-III fracture are briefly described.

2.1.1 Static crack solutions

A common engineering point of view is that structure will fail when the applied load exceeds the load limit. The local generalization of this idea is found in the science of the strength of materials which assumes that materials fail[2] when a stress measure meets/exceeds a critical value [1]. In order to apply this idea, the stress field must first be obtained by solving an elasticity problem. Thus, an analysis of the stress field near the tip of a sharp crack must be carried out before exploring critical states for crack growth initiation and the growth process. For the simplest case of an isotropic, homogeneous and linear elastic material, mode-III fracture is associated with pure anti-plane shear deformation described by only one nonvanishing displacement component given in (x, y) coordinates by,

---

[2] The term *failure* as used here means excessive permanent (plastic) deformation or complete separation across a surface.

$$u_z = u(x, y) \tag{2.1}$$

The stress-displacement relations[3],

$$\sigma_{zx} = \frac{\partial u(x,y)}{\partial x}, \ \sigma_{zy} = \frac{\partial u(x,y)}{\partial y} \tag{2.2}$$

combined with the single nontrivial stress equilibrium equation,

$$\frac{\partial \sigma_{zx}}{\partial x} + \frac{\partial \sigma_{zy}}{\partial y} = 0 \tag{2.3}$$

yields the potential (harmonic, Laplace) equation which governs the anti-plane shear problem,

$$\nabla^2 u(x, y) = 0 \tag{2.4}$$

where $\nabla^2[\bullet]$ is the Laplacian operator.

Several analytical approaches to the solution of static crack problems lead to the determination of the stress intensity factor (SIF), a measure of the strength of the singularity of the crack tip stress field which uniquely characterizes the local behavior near the crack tip. These approaches are: a) complex variable methods [6], b) integral transform methods [7] and c) continuous distributions of dislocations methods [8]. Complex variables (along with conformal mapping [9]) were introduced by mathematicians in order to solve plane harmonic and biharmonic boundary value problems in curvilinear coordinates. Mechanicians applied this work to mode-I and mode-II crack problems governed by the biharmonic equation of plane elasticity, and the mode-III crack problem governed be the potential equation of anti-plane elasticity. Integral transforms are widely used in the formulation of boundary value problems of elasticity [10] as well. Many classical crack problems, such as an elastic plane or strip with a line crack, an elastic cylinder with an infinite or

---

[3] Note that the stresses have been nondimensionalized by the shear modulus μ.

finite radius with an axisymmetric crack, may be reduced to dual integral equations by using Fourier or Hankel transforms [11]. The dual integral equations can be transformed into an Abel integral equation which in turn can be solved exactly or reduced to a Fredholm integral equation [12]. Another approach to the solution of crack problems is to formulate them in terms of a set of Cauchy singular integral equations by employing distributions of dislocations as Green's functions [13].

Mode-III fracture in an infinite plate. It can be shown that near-tip stress and displacement components for the general anti-plane problem are given by [14],

$$\begin{aligned}
\sigma_{zy} &= \frac{K_{III}}{\sqrt{2\pi r_1}}\cos\left(\frac{1}{2}\theta_1\right)\\
\sigma_{zx} &= -\frac{K_{III}}{\sqrt{2\pi r_1}}\sin\left(\frac{1}{2}\theta_1\right)\\
u_z &= \sqrt{\frac{2}{\pi}}\frac{K_{III}}{\mu}\sqrt{r_1}\sin\left(\frac{1}{2}\theta_1\right)
\end{aligned}\tag{2.5}$$

Equations (2.5) shows that the fields are functions of local polar coordinates (r_1 and θ_1, refer to Fig.2.1) and a parameter K_{III} (the mode-III stress intensity factor). K_{III} includes all unique information of the problem including crack geometry and magnitude of remote loading. The character of the field is approximated and controlled solely by the truncated trigonometric functions which imply that regardless of specific problem, the general shape of the local field is always the same. Note that (2.5) is accurate for the near-tip field only due to truncation of higher order terms and, a $r^{-1/2}$ singularity is a general feature of sharp crack solutions regardless of fracture mode.

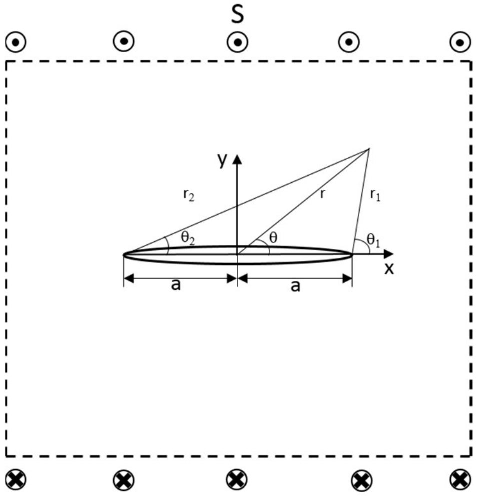

Fig.2.1 Mode-III crack of infinite plate.

Figure 2.1 shows an infinite plate with a sharp crack of finite length subjected to remote equal and opposite uniform anti-plane shear tractions *S*. For this specific geometry it can be shown that K_{III} is given by [1],

$$K_{III} = S\sqrt{\pi a} \tag{2.6}$$

Brittle fracture in a solid is governed by the stress field around the crack tip and the parameters that describe the resistance of the material to crack growth [1]. Related questions to be answered include the load to propagate the crack as a function of crack size, the maximum size of the crack as a function of applied load such that the crack remains static, etc. Note that the singularity of the stress components at the crack tip ($r_1 = 0$) is unphysical and can cause difficulties when trying to use the stress field and, the stress field cannot be used directly as an indicator to determine if the crack will propagate or not. This is because no matter how small the applied load is, the singular behavior of the stresses implies that there will always be a small region close to the crack tip where the stresses exceed a certain finite value of material strength. In the sense of stress-based criteria (or a derived energy-based criteria), this indicates that a crack will propagate under vanishingly small loads which cannot be true. However, brittle fracture is believed to be governed by the local field close to the crack tip such that only the first term in the stress field expression is enough to characterize it (Equation (2.5)). Regardless of different crack geometries and material properties, similar patterns of local stress fields are always characterized by exactly the same trigonometric functions depending on the fracture mode. The uniqueness of the local solution is solely captured by the multiplier (K_{III}),i.e., stress intensity factor (SIF). Instead of comparing the values of stresses, the failure criteria can be introduced by comparing a field based K_{III} with experimental values of K_{III} obtained at crack growth (fracture toughness) for a certain material. It is worth pointing out that the derivation of SIF's are based on linear elasticity for perfectly elastic brittle materials, but the application of this idea is not restricted to those circumstances. With certain modification, the idea can be extended to more complicated material models which give rise to elastic-plastic and creep crack tip fields [15].

Mode-III fracture in a cylindrical rod: In this problem the only one nonvanishing displacement component is the radius dependent circumferential displacement $u_\theta = u(r,z)$. The governing equation is the potential equation (2.4) in cylindrical coordinates. K_{III} for a cylindrical rod with a ring-shaped edge crack (Fig.2.2) is given in [9], obtained by using the Hankel transformation.

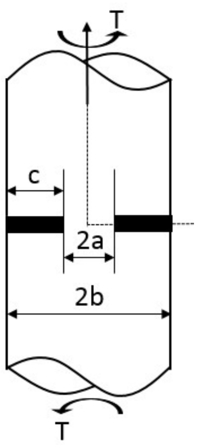

Fig.2.2 Mode-III cylindrical bar ring-shaped crack.

The solution for the near tip field is obtained by quintic interpolation and is given by,

$$\begin{aligned} \sigma_{z\theta} &= K_{III} \frac{2T}{\pi a^3} \left(\frac{ac}{b} \right)^{1/2} \frac{1}{(2r)^{1/2}} \\ K_{III} &= \frac{3}{8} \left(1 + \frac{1}{2} \frac{a}{b} + \frac{3}{8} \frac{a^2}{b^2} + \frac{5}{16} \frac{a^3}{b^3} + \frac{35}{128} \frac{a^4}{b^4} + 0.208 \frac{a^5}{b^5} \right) \end{aligned} \tag{2.7}$$

Note that, similar to the infinite plate crack problem, this solution also has a $r^{-1/2}$ singularity near the crack tip. Apart from difficulties arising from the singular stress at the tip, an artificial nonvanishing stress at the cylinder axis is erroneous and basically comes from the approximation procedure (truncation of higher order terms).

Mode-III fracture in bi-material and multi-crack systems: Problems involving bi-material elastic plates with interface cracks arise naturally from composite materials or plates with coatings (giving rise to a discontinuous material properties). Extensive work has been done in mode-I/II fracture of bi-material systems [16], [17], [18], and for these cases the crack-tip stress distribution has a $r^{-1/2} \begin{pmatrix} \sin \\ \cos \end{pmatrix} (\varepsilon \log r)$ singularity. This is unlike that of uniform material in that it predicts oscillations (including material interpenetration) near the crack tip. The corresponding mode-III problem was studied for the bi-material wedge [19] and the layered system [20]. These authors also generalized the solution to anisotropic materials by introducing an effective shear modulus which is defined to be a function of the anisotropic shear moduli. The layered solution was further generalized to the problem of mode-III cracks in tri-layer composites systems in which all three layers have distinct properties with SIFs given as [21] which is slightly different than that of the corresponding mode-I/II cases.

$$K_{III} = \tau_0 \sqrt{\frac{\pi a}{2}\left(\frac{\mu_1}{\mu_2} + \frac{\mu_1}{\mu_3}\right)} \tag{2.8}$$

Infinite plate solutions are valid when the effect of the boundaries can be neglected, i.e., when the ratio of the crack length to the plate width is very small. Generally, the boundary plays a vital role in stress redistribution (finite domain) and crack interaction. In [14], extensive work on different geometries of layered systems was carried out including work on the semi-infinite plate, the finite plate and parabolic shaped strips. Also presented were solutions with various arrays of cracks including eccentric cracks, collinear cracks, arrays of cracks combining line cracks and elliptical cracks [14].

In summary, the SIF approach is popular for its simplicity of formulation and ease of use. The applied loading, geometric parameters are contained in one parameter K_{III} which can be found, for many different geometries and loadings, in well-known handbooks (e.g., [14]). However, the SIF approach is limited by i) the stress singularity, ii) its prediction of only the close tip field and iii) its inability to account for growth. Regardless of these drawbacks, SIF has proved to be handy and accurate when the crack is sharp, and the bulk material remains linear elastic. The SIF also serves as a foundation for more sophisticated analyses such as small scale yielding, large scale yielding and plasticity, mix-mode fracture and crack dynamics as well. There have been several attempts to eliminate the unphysical stress singularity which limits the applicability of the maximum-stress hypothesis. These entirely different approaches include: adding near tip inelasticity [22], removing the infinitesimal strain assumption [23] and adopting a non-local elasticity approach [24]. Another widely used method that is utilized in this work is to dispense with the sharp crack assumption altogether and employ a cohesive crack surface.

2.1.2 Experimental work

Unlike mode-I and mode-II testing, for which mode-I or mode-II dominant loading can be readily setup, pure mode-III or mode-III dominant fracture is very difficult to create in the laboratory [25], [26]. The reason is that testing is mostly carried out by displacement control systems, however, a mode-III displacement control test cannot guarantee a pure mode-III or mode-III dominant fracture. Thus, complicated testing platforms are required often with mixed results. To avoid difficulties in testing and, to extract the most general behavior of mode-III fractures, researchers have focused on brittle materials in two types of geometries that give rise to mode-III dominant behavior. These configurations are similar to that used to analyze SIFs, i.e., torsion of long slender cylindrical rods and layered composites.

Mode-III fracture testing of rods. In [27] torsion tests are carried out on circular cylindrical rods with or without premade notches of varying shapes and sizes (Fig.2.3) and data are recorded as applied torque vs. twist angle.

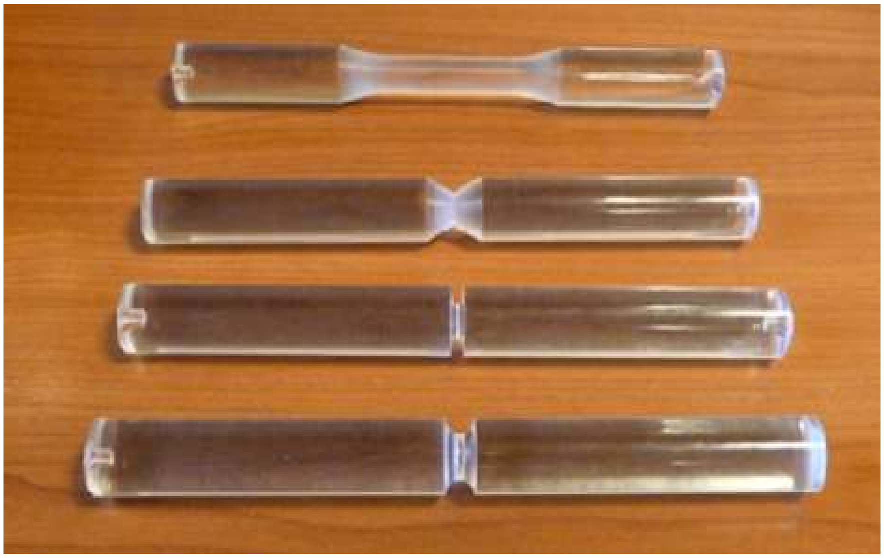

Fig.2.3 Mode III torsion testing, cylindrical testing specimen with different notches [27]

Plots of torque vs. twist angle (Fig.2.4) indicate response characterized by an initial linear elastic deformation followed by an approximate horizontal plateau leading to failure. Testing results also show that the size of the plateau is directly related to the notch shape and size such that the sharper the notch, the smaller the plateau.

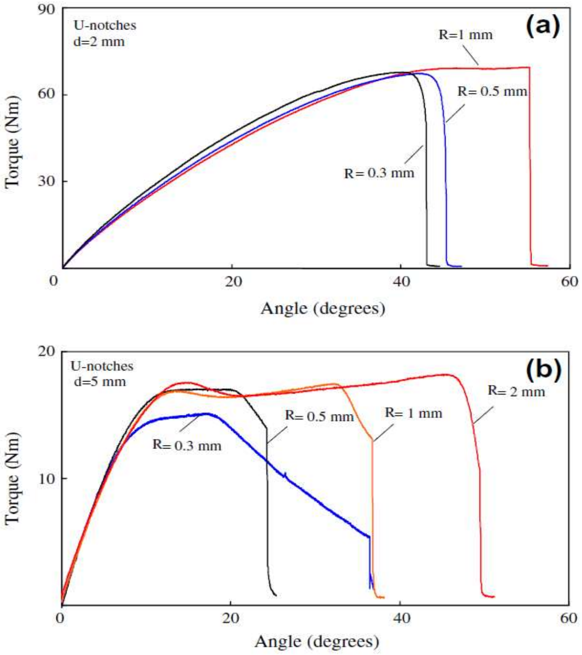

Fig.2.4 Displacement (angle) vs applied torque [27], *d* is cylinder diameter, *R* is notch radius.

Many post processing and data reduction methods can be used for fracture assessment. Among those, the most popular ones include the maximum elastic stress, the maximum elastic-plastic stress by Neuber's rule [28] or, the equivalent strain energy density criterion, nominal stress at notch tip and averaged strain energy density [29]. This testing not only answers the question about the macroscopic response of the rod (large scale yielding or slip prior to failure), but also can be applied to mixed mode I/III fracture [30], [31]. The orientation of the fracture surface of initially notched PMMA rods for different mode-mixities and initial notch sizes was explored in [32]. It was found that the mode-III dominated loading tends to create a spiral fracture surface whereas for mode-I dominated loading, the fracture surface is flatter (Fig.2.5). The transition from a spiral to a flat fracture surface is also affected by the relative notch size. Some authors [33], [34], [35] speculate that the spiral fracture surface is a consequence of the merging of micro cracks which are oriented perpendicular to the maximum principal stress. Another phenomenon related to micro cracks is the factory-roof pattern observed when specimens are subjected to torsional fatigue testing [34]. Mode-III fatigue crack propagation was studied in [36] using circular cylinder test specimens made of steel. Compared with mode-I fatigue fracture, the mode-III fatigue crack growth rate is slower. Unlike mode-I fracture, characterized by small scale yielding, mode-III fracture growth has a larger plastic zone. Growth rates of low strength materials are better approximated by some large-scale plasticity parameters.

Fig.2.5 Flat and spiral fracture surface in torsion test [32].

Mode-III fracture testing of layered media. To characterize mode-III interlaminar fracture mechanisms of layered media, testing often utilizes beam or layered systems which are used extensively in mode-I/II testing. The Edge Crack Torsion (ECT) test is widely used since an almost pure mode-III state can be achieved with a relatively simple fixture. Studies were carried out in [37] as to whether the ECT test can be developed into a standard test for mode-III fracture toughness. Their results revealed that certain difficulties such as deviation from linearity before crack initiation, and dependency of the energy release rate on insert length, restrict its further application. There are many other commonly used tests in the literature [38] all of which are designed to get standard material properties governing the fracture process (e.g., fracture toughness, critical energy release rate). Each of the above methods however have their own limitations and are only applicable under certain conditions which hinders engineers from developing a versatile standardized testing procedure for mode-III fracture.

2.1.3 Numerical simulation

Experimental work yields information specific to a particular testing configuration. In order to interpret and generalize the results, experimental studies are often coupled to numerical simulations. Analytical methods may not be appropriate for this because of their limited ability to provide exact solutions to other than the simplest problems (mostly those involving infinite or semi-infinite domains with simple crack geometries). Numerical methods, however, can be employed to treat more complicated cases although the elegance, precision and insight of the analytical solution is lost. The finite element method (FEM) is currently the most popular method for the analysis of crack problems due to its accuracy and ease of use. Due to the strong stress concentration at the crack tip, finer meshing (or special element) is needed to obtain a reasonably accurate stress field near the crack tip. However, finer meshing means that more elements and nodes are needed which increases the computational burden and takes longer times for solution convergence. A more sophisticated branch of FEM is fractal finite elements (FFEM). This method has a hierarchical mesh structure. Near the crack tip, an imagined zone containing the stress singularity is modeled by a successive refining mesh. Mode-III related work by FFEM is mostly about calculating SIFs. In [39], FFEM was employed to determine mode-III SIFs and extended into bi-material cracked /notched bodies subjected to anti-plane loading. Another well-developed FEM based numerical method (extended finite element (XFEM)) utilizes specific features from fracture mechanics solutions. The basic idea of XFEM is to add discontinuous special functions to expand the finite element space in order to capture special localized behaviors. XFEM suppresses the need for remeshing and improves accuracy and convergence rates. XFEM allows for arbitrary crack growth within an existing mesh at the cost of the restriction that the discontinuity has to be on the element edge. Other numerical methods such as boundary element method (BEM) and meshless methods have also been developed in order to obtain near tip fields.

The numerical methods mentioned above are generally based on the assumptions of LEFM, and results obtained from them have proved to be accurate in comparison to classical SIF solutions given in handbooks or other existing testing results. Numerical analyses may circumvent the difficulties in the mathematical derivation of SIF's and can be applied to more complicated geometries. In order to get continuous crack behavior such as crack propagation, additional constitutive relations that map crack surface deterioration progressively rather than in a binary description of intact or failed are needed. One of the most commonly used mechanisms is the cohesive surface governed by traction-displacement discontinuity[4] relations. This will be introduced in the following section.

---

[4] A normal (shear) displacement discontinuity is termed separation (slip).

2.2 Cohesive zone models (CZM)

Linear elastic fracture mechanics (LEFM) has proven to be a useful tool in analyzing a wide range of crack problems but it has some well-known limitations. First, even for metallic materials in the elastic regime, a highly localized nonlinear plastic zone will develop at the crack tip. LEFM is applicable only when the plastic zone is within the region where the stress singularity dominates (K-dominant zone). Second, LEFM is based on a simplified or idealized model of a crack tip that is geometrically sharp and well defined (i.e., a clear boundary between separated and unseparated regions with no gradual transition region between them). The idealized sharp crack tip introduces an unphysical stress singularity which requires that its strength be used as the parameter whose critical value determines fracture initiation. Issues such as, a) the stability of the crack propagation process, b) its speed of propagation, c) the existence of critical values of crack size prior to unstable growth, cannot be easily answered by LEFM. Other constitutive relations or assumptions are needed. To handle these problems, a natural and powerful method is to replace the linear elastic region ahead of the sharp crack tip with a general material degrading mechanism (cohesive force law) governing behavior in the process zone (a small region near the crack tip where micro defects initiate and evolve).

The concept of a cohesive zone was first proposed by Barenblatt [4] and Dugdale [5] in order to eliminate the LEFM stress singularity and to provide a separation mechanism at the crack tip. They suggested that two regions of surface within the fracture process zone are close enough to be modelled as two atomic layers held by atomic bonding forces which are separation dependent. In a continuum mechanics setting, this mechanism is characterized by relations between surface traction components and separation/slip components and, these cohesive constitutive laws are used to characterize the behavior in the process zone. Cohesive constitutive relations can be categorized as local if they are applied near the crack tip, or global if they are applied along the entire path on which a crack is assumed to grow [40]. Based on their mathematical structure, cohesive laws can be divided into nonpotential-based and potential-based models. Nonpotential based cohesive laws are relations between components of cohesive surface traction, components of displacement discontinuity across a cohesive surface (and possibly other variables related to the fracture process) and can capture different kinds of surface phenomena such as friction, fatigue, time dependent damage, etc. The limitations of non-potential based models include, i) for mixed mode fracture, nonpotential based cohesive force laws cannot account for all possible separation sequences (sequence dependent energy dissipation), and ii) possibility of non-physical cohesive interactions, e.g. positive stiffness in a softening region [41], etc. Potential-based cohesive models are structured so that the traction is the gradient (with respect to separation or slip) of a scalar potential (Ψ). These relations are usually expressed in terms of component relations normal and tangent to a surface [42]. However, the main drawback of potential based models is that they are not suitable for describing irreversible material deterioration and may lead to undesirable and unphysical cohesive surface self-healing under cyclic loading or fatigue analysis. Other limitations include, i) the introduction of repulsive normal tractions in mixed-mode conditions, and ii) a complicated formulation with parameters that are not easy to obtain experimentally, etc.

2.2.1 General structure and parameter characterization of cohesive laws

Regardless of the different cohesive zone relations that have been developed in the past few decades, a cohesive law is generally composed of two basic branches, a quasi-linear branch and a softening branch. It’s worth pointing out that, i) the area below the cohesive law curve is the fracture energy density of the material, ii) the shape of the curve is uniquely characterized by the cohesive strength, the cut-off separation (if one exists), the range of action of the force law (characteristic force length) and possibly other quantities related to the separation/slip process. The characterization of a particular cohesive force law is a complicated and laborious process including extensive testing, numerical simulations, verification and modification. Generally speaking, apart from the special methods of Digital Image Correlation (DIC) [43] and atomistic simulation [44], the most widely used method is an inverse problem approach [45], [46]. This can be summarized as, i) choosing a certain shape of cohesive relation based on experience and material type, ii) conducting experiments and measuring the load-displacement or load-crack opening displacement curve data which can be used to derive cohesive law parameters, iii) using a derived cohesive law in a FEA simulation to find the optimal parameters such that they are consistent with experiment within acceptable error. It is worth noting that there are multiple parameters characterizing a certain force law and some of them can be determined from testing or have recommended values provided by manufacturers. However, the common situation is that not all of them are independent from each other which means it is almost impossible to satisfy all the parameters provided at the same time, and some of the parameters are less important since they have little impact on the numerical simulation process. Certain compromises must be made such that some of the primary parameters are satisfied. A consensus agreed to by most researchers is that the two most important governing parameters are the cohesive strength (provided or recommended values can be found) and the fracture energy, and these two parameters are also closely related to testing. Their influence on FEA simulation have been studied by Peter et.al [47]. For mode-I (mode-II) fracture problem, standard DCB (MMB or ENF) testing and data reduction methods to obtain the critical energy release rate (G_{Ic}, G_{IIc}) have been proposed. However, a standard mode-III testing configuration for G_{IIIc} has not yet been standardized. Steven proposed SCB for G_{IIIc} but the testing is restricted by its sensitivity to specific geometries [48]. His testing results shows that G_{IIIc} generally doubles the reported value of G_{IIc} for the same material. Given values of primary parameters and shape of cohesive force law, the derived parameters can be calculated and the expression of cohesive force law is obtained [49].

2.2.2 The piecewise linear law

Barenblatt [4] and Dugdale [5] first applied a local cohesive zone to analyze brittle and elastic-ideally plastic fracture of materials in opening mode. The basic idea is to apply a softening or yielding process close to the crack tip to eliminate the stress singularity. The cohesive relations used (Fig.2.6) are the linear softening model [38] and the constant yielding model [39]. Both are relatively simple phenomenological relations since straight lines are used to capture idealized linear softening (or yielding) response.

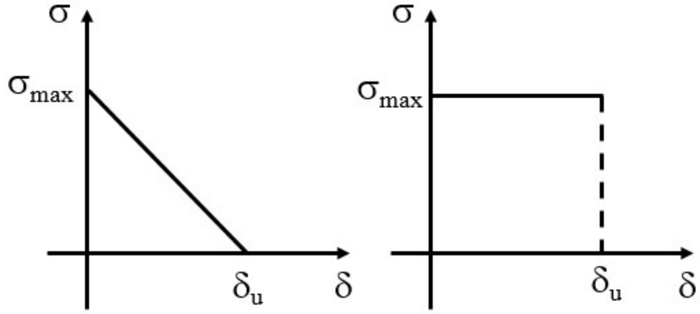

Fig.2.6 Barenblatt linear softening cohesive zone and Dugdale ideal plastic cohesive zone.

Due to increased computational power, more complicated cohesive relations were developed that are capable of capturing behaviors such as ductile and brittle fracture in uniform and bi-materials, interface delamination, fatigue fracture, viscous effects, etc. For these problems, the cohesive law is taken to apply to a finite but vanishingly thin physical interface separating two distinct materials or, to a uniform material containing a hypothetical predetermined surface along which a crack is assumed to grow. Early examples of cohesive constitutive relations are the bi-linear and trapezoidal laws [50].

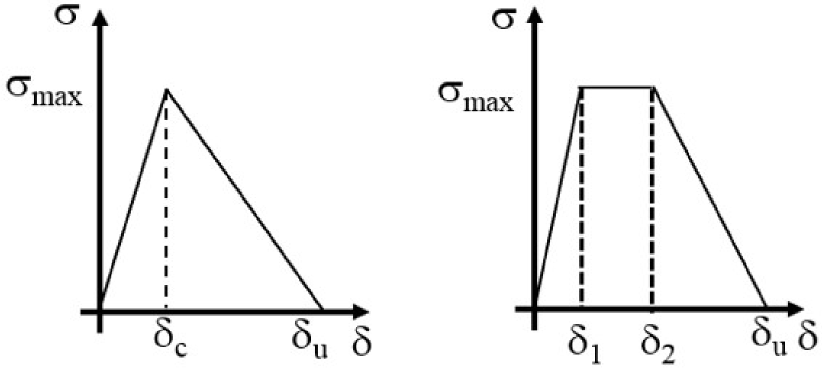

Fig.2.7 Bi-linear model, trapezoidal model in opening mode.

These are shown in Fig.2.7 for opening mode as the cohesive relation curves are in the first quadrant. Note that by tuning the parameters of the trapezoidal law, the bi-linear, linear softening or Dugdale models can be obtained. These force laws all have a finite cutoff length, i.e., the traction vanishes at a finite value of separation (δ_u). The expression for the trapezoidal law is given as,

$$\sigma = \begin{cases} \sigma_{\max}(\delta / \delta_1) & 0 \le \delta \le \delta_1 \\ \sigma_{\max} & \delta_1 \le \delta \le \delta_2 \\ \sigma_{\max}(\delta_u - \delta)/(\delta_u - \delta_2) & \delta_2 \le \delta \le \delta_u \end{cases} \tag{2.9}$$

and four parameters (σ_{max}, δ_1, δ_2, δ_u) characterize its shape. The quantity σ_{max} is the maximum traction the surface/interface can carry. Quantities δ_1 and δ_2 control the size of the plateau (yielding regime) and the slope of linear and softening branches. δ_u is the ultimate separation beyond which no traction can be carried signaling total failure. The fracture energy density (area below the curve) and initial stiffness are given as

$$\begin{aligned} \Gamma &= \frac{1}{2}\sigma_{\max}(\delta_u + \delta_2 - \delta_1) \\ E_i &= \sigma_{\max} / \delta_1 \end{aligned} \tag{2.10}$$

respectively. Note that if δ_1 is set equals to δ_2, the trapezoidal model reduces to the bi-linear relation with $\delta_2=\delta_1=\delta_c$. If $\delta_1= \delta_2=0$, it reduces to linear softening model. When $\delta_1=0$, $\delta_2= \delta_c$ the relation reduces to the Dugdale model with constant cohesive traction.

To differentiate normal (separation) and shear (slip) modes, the following notation is introduced. For displacement discontinuity in the plane, *u* represents the component normal to the surface (normal separation) while *v* represents the component tangent to the surface (shear slip). Normal (shear) traction is written as *f* (*g*). Other constitutive parameters are labeled with subscript *n* (*t*) for normal (shear). The normal mode cohesive relation (Fig.2.8) is a more general form than the opening mode relation (Fig.2.7) because it attempts to capture contact when the surface/interface is in compression. This is done by adding to the 3rd quadrant a very high stiffness branch. This approximation allows for material interpenetration, the magnitude of which can be decreased by increasing the slope of the branch in the compressive region.

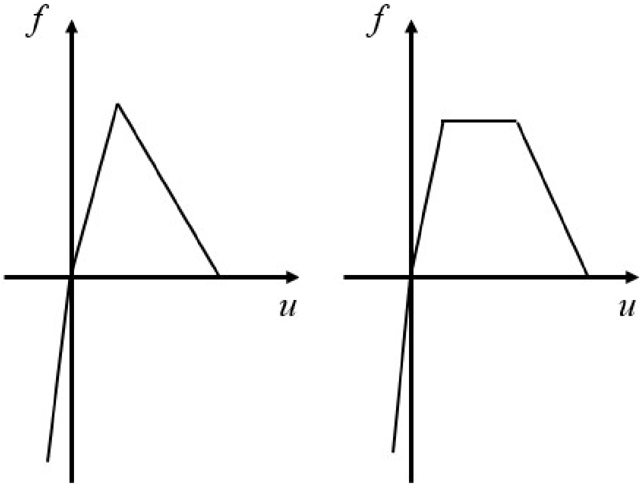

Fig.2.8 Cohesive relations in normal mode.

The main difference between shear and normal mode is in how to interpret a negative displacement jump. In normal mode, a small negative separation give rise to material interpenetration which approximates contact. This is a totally different process than material separation. However, shear mode is not directionally sensitive, i.e., the sign of slip indicates the direction of relative movement of material above and below cohesive surface. By flipping the 1st quadrant of the force law, skew symmetric cohesive relations covering negative shear slip are obtained as shown in Fig.2.9.

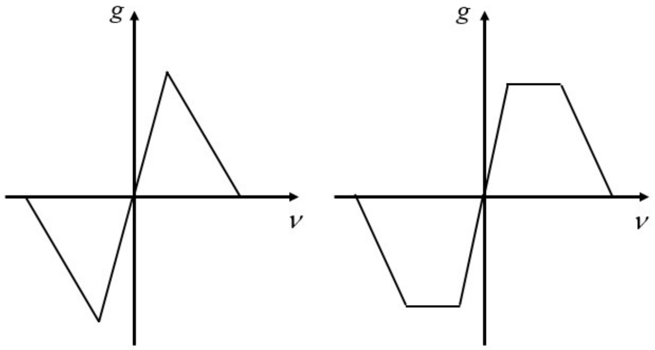

Fig.2.9 Cohesive relations in shear mode.

2.2.3 The Xu-Needleman law

Piecewise linear cohesive laws are simple to develop and relatively easy to implement. Several main disadvantages limit their application. Piecewise linear laws are phenomenological, i.e., they are without any physical basis and, they are not smooth, i.e., the discontinuities in slope may cause convergence problems during computation. Furthermore, the laws are not potential based and may have consistency problems in mixed-mode applications such as path dependent energy dissipation. This is also true for polynomial type force laws of the kind used in [51].

Physically based cohesive relations often have an exponential character and are derived from an atomic potential. A normal mode universal binding law (2.11), derived from the adhesive and cohesive binding energies of metallic materials has been proposed in [52], [53], [54]. These relations have the form,

$$f = e\sigma_{\max}\frac{u}{\delta_n}e^{-u/\delta_n} \tag{2.11}$$

where the two parameters (σ_{max} and δ_n) are all that are needed to characterize a unique exponential cohesive relation. $\sigma_{\max}$ controls the height of the curve whereas δ_n determines the range of action of the force law. By tuning these two parameters carefully, brittle and ductile cohesive surface responses can be obtained from one framework. Theoretically, the decohesion process terminates only when the separation is unbounded. Practically, a predetermined cutoff separation value can be set characterizing total failure. The fracture energy density and initial stiffness are given as,

$$
\begin{aligned}
&\phi = e\delta_n\sigma_{\max} \\
&E_i = e\sigma_{\max} / \delta_n
\end{aligned}
\tag{2.12}
$$

An analogous potential for shear slip has been introduced in [55]. The Xu-Needleman law combines the distinct physically based exponential shear and normal relations into a phenomenological force law. The model accounts for coupling between the modes and thus can be used to predict failure under mixed-mode conditions [56], [57]. This potential based model can be expressed as,

$$
\begin{aligned}
&\Psi(u,v) = \phi_n + \phi_n \exp\left(-\frac{u}{\delta_n}\right)\left\{\left[1-r+\frac{u}{\delta_n}\right]\left(\frac{1-q}{r-1}\right) - \left[q+\frac{(r-q)u}{(r-1)\delta_n}\right]\exp\left(-\frac{v^2}{\delta_t^2}\right)\right\} \\
&f = -\frac{\partial\Psi}{\partial u} = \frac{\phi_n}{\delta_n}\exp\left(-\frac{u}{\delta_n}\right)\left\{\frac{u}{\delta_n}\exp\left(-\frac{v^2}{\delta_t^2}\right) + \left(\frac{1-q}{r-1}\right)\left[1-\exp\left(-\frac{v^2}{\delta_t^2}\right)\right]\left[r-\frac{u}{\delta_n}\right]\right\} \\
&g = -\frac{\partial\Psi}{\partial v} = \frac{\phi_n}{\delta_n}\frac{2\delta_n}{\delta_t}\frac{v}{\delta_t}\left[q+\frac{(r-q)u}{(r-1)\delta_n}\right]\exp\left(-\frac{u}{\delta_n}\right)\exp\left(-\frac{v^2}{\delta_t^2}\right)
\end{aligned}
\tag{2.13}
$$

The model has 5 parameters ($\phi_n, \delta_n, q, \delta_t, r$). The first four are related to cohesive energy densities in normal and shear mode and must be determined from experiment. They can be divided into two groups which characterize normal and shear response respectively. ϕ_n and δ_n characterize the normal response and related to normal cohesive strength by 2.14_1. The nondimensionalized parameter q characterizes the ratio of cohesive energy density of shear and normal mode by 2.14_2. Based on the definition, the shear cohesive energy density is related to shear direction characteristic length and shear cohesive strength by 2.14_3,

$$\phi_n = \sigma_{\max} e \delta_n$$
$$q = \phi_t / \phi_n \tag{2.14}$$
$$\phi_t = \sqrt{e/2}\,\tau_{\max} \delta_t$$

Another nondimensionalized parameter *r* is defined by,

$$r = u^* / \delta_n \tag{2.15}$$

u^* is the value of normal separation after complete shear separation under the condition of zero normal traction, i.e., $f = 0$. In general, *r* is set to be vanishing since it ensures that a pure shear loading will not induce any normal separation.

The force law in uncoupled form for each mode is shown in Fig.2.10 for various values of force length parameter.

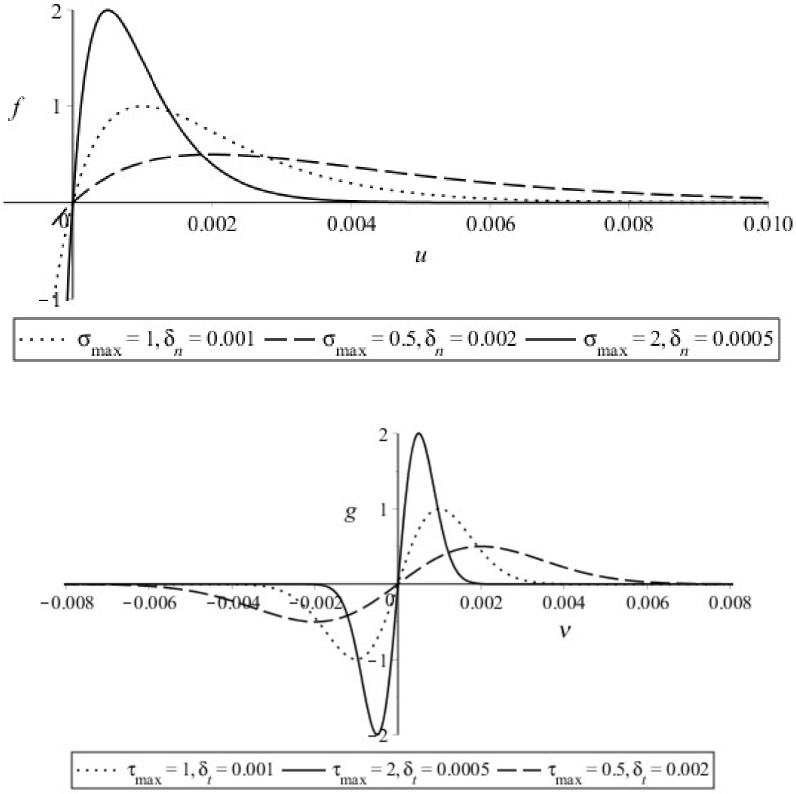

Fig.2.10 Uncoupled Xu-Needleman cohesive law in normal and shear modes.

Advantages of Xu-Needleman constitutive relation are that it is physically based and combines opening and shearing modes in one framework. The limitations of the Xu-Needleman constitutive law are i) that under total shear failure the normal traction does not vanish, ii) the parameter u^* is ill-defined and difficult to obtain experimentally, iii) there is no finite cut-off length, which does not resemble macroscopic fracture behavior [42], iv) loading and unloading response of potential force relations gives rise to surface “healing” which is unphysical, v) material interpenetration is not eliminated but minimized by the high cohesive surface stiffness in compression. Other more complex force laws exist in the literature however these force laws have their limitations as well.

Most of the results presented in this dissertation are for the Xu-Needleman potential force law. In pure shear mode, with zero normal traction, it assumes the form (Fig.2.10 b),

$$g(v) = \sqrt{2e}\tau_{\max} v / \delta_t e^{-(v/\delta_t)^2} \tag{2.16}$$

The characteristic length δ_t in (2.16) is scaled by a factor of $\sqrt{2}$ so that maximum stress occurs at $v = \delta_t$. Thus, rewrite (2.16) as,

$$g(v) = \sqrt{e}\tau_{\max} v / \delta_t e^{-0.5(v/\delta_t)^2} \tag{2.17}$$

2.2.4 Cohesive force laws with friction

The cohesive force laws discussed above mainly focus on the decohesion process in which the material interpenetration is minimized by setting a high stiffness in the 3rd quadrant of the normal cohesive law. This treatment suppresses the cohesive surface response when subject to compressive loading. However, when the problem to be studied consists of a significant amount of compressive load, which may induce nonnegligible friction effects, a specialized cohesive law which include frictional response should be used. Cohesive laws that account for friction as well as decohesion have been proposed in the literature [58], [59]. A simple model that separates the debonding process from the friction process is given in [60]. In this work the classic Coulomb friction law was assumed to become active only after complete decohesion (Fig.2.11). Another model introducing the friction mechanism from the very beginning, i.e., before complete decohesion is given in [61].

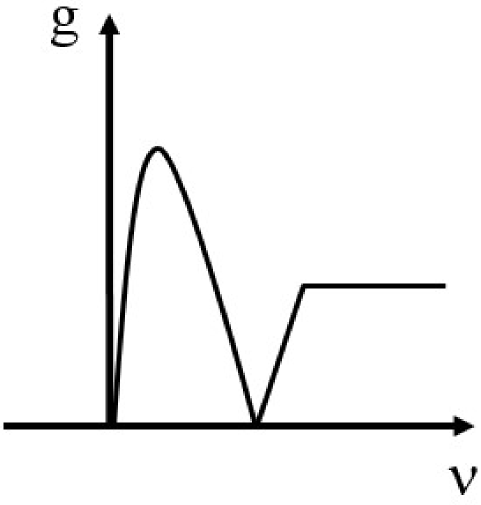

Fig.2.11 Cohesive-friction model [62].

Recently, a nonlinear cohesive/frictional contact model for mode-II shear debonding of an adhesive composite joint was proposed [63] based on a modified Xu-Needleman's exponential cohesive relation (Fig.2.12). Compared to previous constitutive relations, this model is built upon the potential based Xu-Needleman law. Since friction is affected by normal traction, a unified normal-shear model is more reasonable than models whose friction mechanism is based on uncoupled normal traction.

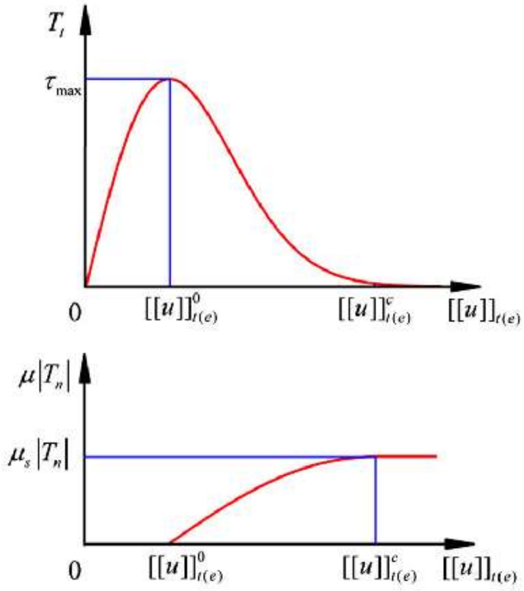

Fig.2.12 Cohesive-friction model [63].

2.3 Cohesive fracture mechanics

Cohesive zone models have undergone rapid development since their introduction by Barenblatt [4] and Dugdale [5] almost 60 years ago. At that time they were applied to a small region near the crack tip and served as a local mechanism to remove the stress singularity in LEFM [4], [5] and to capture localized plasticity in the fracture process zone [64]. Analytical work of this type extends LEFM in such a way that many of the features of the classical solution still apply. The idea of extending these kinds of models to an entire cohesive surface was presented by Needleman in [51], [65], [40].Today, they are employed mostly within a finite element framework to model behaviors such as quasi-static [66], [67] and dynamic crack propagation [68], [69], mixed-mode fracture of nonlinear [70], time dependent materials [71], etc.

2.3.1 Static defect solution

In this dissertation a (global) cohesive zone is applied to the entire (predetermined) surface along which the defect is assumed to propagate. Analytical work of this kind is mostly based on analyzing beams with cohesive defects ([72]). These studies apply classical beam or plate theories along with cohesive relations. The solutions are available for the mode-I double cantilever beam test [73], [74], mode-II end notch flexure test [75], and the mode-I/II mixed mode bending test [76]. However, most of this work is based on strength of materials theories of bending and relatively simple cohesive relations focusing on pre-failure response. An exact elasticity based theory of debonding and defect propagation has been proposed in [77], [78] which can be integrated with nonlinear cohesive laws. Related work of this type is cited in section 2.5.

2.3.2 Finite element simulations

Analytical solutions to problems employing cohesive zone models can answer fundamental questions about cohesive surface stability and defect propagation which help researchers have a better understanding of different cohesive laws and their predictions. However, analytical approaches are largely limited to simple geometries and relatively simple cohesive relations. For more complicated geometries and bulk material models, analytical solutions are exceedingly difficult to obtain due to mathematical complexity. Pioneering early work on FEM applied to cohesive surfaces involved the analysis of tensile decohesion along an cohesive surface with imperfections [65], modelling void nucleation processes [81] and studying dynamic crack growth and crack path branching [68]. Generally, two main methodologies can be found in modelling cohesive fracture depending on whether fracture is restricted to mesh boundaries. The first method restrains the crack propagation to occur between elements, branching or fragmentation is naturally obtained from the calculation process. Related work includes cohesive crack growth in concrete [82], [83], and nonuniform cohesive surface delamination analysis [40]. The other method enables crack growth within elements [84] which can be used to keep track of the unknown crack path. A direct extension of such work is called the extended finite element method (X-FEM) [85] that has been developed to model arbitrary discontinuities in meshes.

2.4 Linear and Nonlinear Integral Equations; Eigenfunction Expansions

An integral equation is an equation in which the unknown function to be solved for occurs within a definite integral (Fredholm integral equation) or indefinite integral (Volterra integral equation[5]). If the unknown function occurs in linear terms then the integral equation is linear, otherwise it is nonlinear. Because of their centrality to this work the following subsections contain a brief review of these equations.

2.4.1 Linear integral equations

The linear *Fredholm integral equation of the first kind* is,

$$\int_a^b K(x,y)u(y)dy = f(x) \tag{2.18}$$

where u is unknown (the solution). In (2.18) K (the *kernel*) and f (the *forcing*) are prescribed. The more common, linear *Fredholm integral equation of the second kind* has the unknown function occurring both inside and outside the integral, i.e.,

$$u(x) - \mu\int_a^b K(x,y)u(y)dy = f(x) \tag{2.19}$$

where μ is an arbitrary numerical quantity called the parameter of the equation. Fredholm integral equations arise in many applications in mechanics [12], [86] since elliptic partial differential equations with Dirichlet and Neumann boundary conditions can be transformed into them. Because the boundary value problems that are considered in this work are of Sturm-Liouville type [87], we

---

[5] These will not be considered further as they are not relevant to the work described in this document.

will elaborate on the theory of linear and nonlinear Fredholm integral equations of the second kind with separable kernels.

Solutions to Fredholm integral equations

The general solution to Fredholm integral equations of the second kind can be formulated by successive approximation as a Neumann series [12], i.e.,

$$\begin{aligned} u(x) &= \sum_{n=0}^{\infty} \mu^n u_n(x) \\ u_0(x) &= f(x) \\ u_n(x) &= \int K_n(x,y) f(y) dy \\ K_n(x,y) &= \int\int \ldots \int K(x,y_1)K(y_1,y_2)\ldots K(y_{n-1},y) dy_1 dy_2 .. dy_{n-1} \end{aligned} \tag{2.20}$$

Even though the successive approximation method has mathematical simplicity and stable precision improvement, the main reason that the method is not applied in this work is due to multiple integration processes which take most of the computation time.

A special kind of Fredholm integral equation has a separable or Pincherle-Goursat (PG) type kernel which can be written as,

$$K(x,y) = \sum_{k=1}^{n} X_k(x) Y_k(y) \tag{2.21}$$

If we write

$$\int_a^b Y_k(x) u(x) dx = \xi_k \ \ (k = 1,2,\ldots,n) \tag{2.22}$$

and substitute back into (2.19) the result is a series expansion for the unknown function,

$$u(x) = f(x) + \mu \sum_{k=1}^{n} \xi_k X_k(x) \tag{2.23}$$

Now multiply (2.23) by $Y_h(x)$ ($h=1,2,\ldots,n$) and integrate within the domain to get,

$$\begin{aligned} &\xi_h = b_h + \mu \sum_{k=1}^{n} a_{hk}\xi_k \ \ (h = 1,2,...,n) \\ &\int_a^b X_k(x)Y_h(y)dx = a_{hk}, \ \int_a^b Y_h(x)f(x)dx = b_h \end{aligned} \tag{2.24}$$

This can be reduced to an algebraic system of *n* linear equations in *n* unknowns,

$$\left.\begin{aligned} &(1-\mu a_{11})\xi_1 - \mu a_{12}\xi_2 - ... - \mu a_{1n}\xi_n = b_1 \\ &-\mu a_{21}\xi_1 + (1-\mu a_{22})\xi_2 - ... - \mu a_{2n}\xi_n = b_2 \\ &...... \\ &-\mu a_{n1}\xi_1 - \mu a_{n2}\xi_2 - ... + (1-\mu a_{nn})\xi_n = b_n \end{aligned}\right\} \tag{2.25}$$

Another special kind of kernel is the symmetric kernel, $K(x,y)=K(y,x)$, which can be written either as an infinite sum of eigenfunctions or, reduced to a PG kernel. For the Sturm-Liouville boundary value problem the corresponding kernels can be written as infinite eigenfunction expansions. The general solution scheme is approximation by truncation and reduction to a set of simultaneous algebraic equations by the orthogonality process. Assume ϕ_i and λ_i are the i^{th} orthonormal eigenfunction and corresponding eigenvalue (distinct, real valued). Then the kernel and solution can both be written as follows,

$$\begin{aligned} &K(x,y) = \sum_{j=1}^{n} \frac{\phi_j(x)\phi_j(y)}{\lambda_j} \\ &u(x) = \sum_{i=1}^{n} C_i\phi_i(x) \end{aligned} \tag{2.26}$$

where (2.26_1) is the bilinear formula [12]. Substitution into (2.19) yields,

$$\sum_{i=1}^{n} C_i\phi_i(x) = f(x) + \mu\int_a^b \left[\sum_{j=1}^{n} \frac{\phi_j(x)\phi_j(y)}{\lambda_j} \sum_{i=1}^{n} C_i\phi_i(y) \right] dy \tag{2.27}$$

and by orthogonality of eigenfunctions (i.e., multiply both sides by $\phi_m(x)$ and integrate),

$$\int_a^b \sum_{i=1}^{n} C_i\phi_i(x)\phi_m(x)dx = \int_a^b f(x)\phi_m(x)dx + \mu\int_a^b \int_a^b \left[\sum_{j=1}^{n} \frac{\phi_j(x)\phi_j(y)}{\lambda_j} \sum_{i=1}^{n} C_i\phi_i(y) \right] \phi_m(x)dydx \tag{2.28}$$

Note that m is a free index and the only nontrivial term occurs when $i=j=m$. The sums are annihilated so that,

$$C_m = \frac{\int_a^b f(x)\phi_m(x)dx}{(1-\mu/\lambda_m)} \tag{2.29}$$

The solution (2.26$_2$) is now completely determined in the form of an eigenfunction expansion.

2.4.2 Nonlinear Fredholm integral equations of the second kind

It has been shown that problems [78], [88] involving debonding and decohesion (see section 2.5) can be formulated as nonlinear Fredholm integral equations of the second kind (*Hammerstein integral equations* [12], [89]). The general form of these equations are,

$$u(x) = f(x) + \mu\int_a^b K(x,y)F(u(y))dy \tag{2.30}$$

where the kernel $K(x,y)$ and forcing $f(x)$ are given real-valued functions, $F(u(x))$ is a nonlinear function of $u(x)$ which appears both inside and outside the integral. Commonly used solution techniques include direct computation method, series solution method, the Adomian decomposition method and successive approximation method [89]. The series solution method is to basically write $u(x)$ in a Taylor series expansion which simplifies the integration of the nonlinear term. Adomian decomposition method applies Adomian polynomials to express nonlinear terms which result in decomposing the unknown function $u(x)$ into an infinite sum of components that will be determined recursively through iterations. The successive approximation method (also called the Picard iteration method) solves integral equations by finding successive approximation to the solution starting from an initially guessed function $u_0(x)$. Since the kernel of our particular problem is of a very special kind (separable), direct computation method is employed. The approach reduces the nonlinear Fredholm integral equation to an infinite set of nonlinear algebraic equations which can then be truncated and solved. To see this, first write an approximate truncated separable kernel in the form,

$$K(x,y)=\sum_{k=1}^{n}g_k(x)h_k(y) \tag{2.31}$$

and substitute back into (2.30) to get,

$$\begin{aligned} u(x) &= f(x)+\mu\sum_{k=1}^{n}\alpha_k g_k(x) \\ \alpha_k &= \int_a^b h_k(y)F(u(y))dy \end{aligned} \tag{2.32}$$

Substituting (2.32_1) into (2.32_2) gives a system of n nonlinear algebraic equations governing the constants α_k. Once these constants have been obtained, they can be substituted back into (2.32_1) to obtain the spectral decomposition of the solution. Note that the method of transforming nonlinear Fredholm integral equations to a finite set of nonlinear algebraic equations and solving by Newton-Raphson method has been used to analyze cohesive surface debonding and defect propagation in layers [78], [80], debonding at circular cohesive surface [90], [91] and defect propagation at circular cohesive surface [88].

2.5 Integral equation formulations of cohesive fracture problems

For cohesive fracture problems containing cohesive surfaces separating two or more subdomains, the cohesive surface constitutive relations which are different from bulk material constitutive relations lead to, i) complicated traction distribution along the cohesive surface, ii) deformation discontinuity across the cohesive surface (debonding), are the main focus of attention. The problem can be simplified by relegating nonlinearity to cohesive surface/interface[6] such that exact linear

---

[6] Cohesive interface explicitly refers to a physical interface separating two media. Cohesive surface is a more general term which can refer to cohesive interface, or an imagined surface whose purpose is solely characterizing defect propagation within one medium.

elasticity solutions to the bulk media can be employed to formulate nonlinear boundary conditions in the form of integral equations for the cohesive surface displacement discontinuities. Since the method is also applied in this work, the general procedure and successful example of its application will be briefly introduced in this subsection. Regardless of different geometries, loading and cohesive relations, the procedure can be generalized in the following steps,

1) Define component sub-problems. For composites and inclusion problems involving physical interface between different media, the domains of the component sub-problems are clearly defined by the interface where delamination or debonding would happen (shown in Fig.2.13 inclusion problem). However, for media with defect rather than physical interfaces, the cohesive surface is obtained by making an imaginary cut at the predetermined defect plane where defect would propagate (shown in Fig.2.13 beam problem). The traction on the cohesive interface or newly introduced cohesive surface by cut, is set to be arbitrarily distributed but satisfies the equilibrium of the component sub-problem.

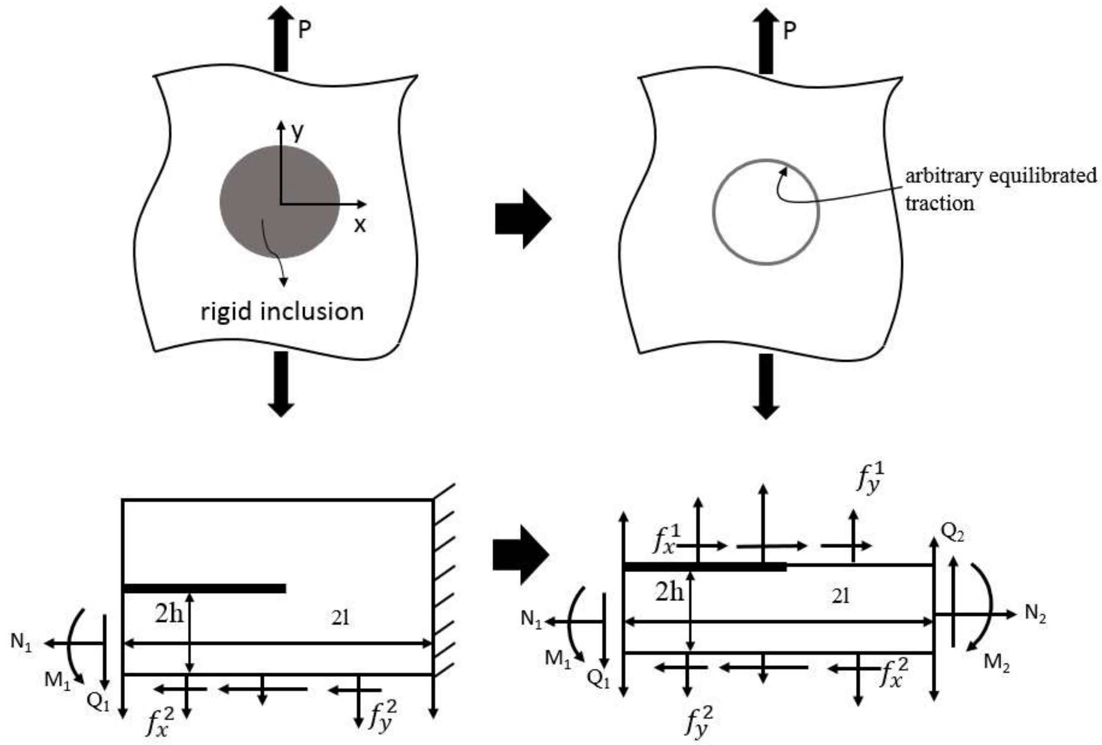

Fig.2.13 Cohesive fracture problem and its corresponding component sub-problem.

2) Obtain the analytical solution of the deformation field to the component sub-problem by solving the corresponding boundary value problem.
3) Integrate the two component sub-problems by applying a cohesive relation which relates the displacement discontinuity (deformation differences of the two constituents of the cohesive surface) with cohesive surface traction. Reconstruct the equations in form of solvable system of nonlinear integral equations.

The nature of the problem-solving process leads to nonlinear boundary conditions in the form of integral equations governing the cohesive surface fields. Note that for a more general geometry or loading, the component sub-problem may consist of displacement discontinuity and traction in multiple directions. If displacement discontinuities are coupled, the mixed-mode cohesive law should be applied, and the formulation is rather complicated. For the pure mode-III formulation described in the following chapters (uncoupled unidirectional deformation), the essential structure of a unidirectional cohesive fracture problem, in form of integral equations, can be written as,

$$\begin{aligned} [u](x) &= h(x,S) + \int_0^1 K(x,\xi)\cdot g([u](\xi),\xi)d\xi \\ L(S) &= \int_0^1 g([u](\xi),\xi)\cdot f(\xi)d\xi \end{aligned} \tag{2.33}$$

Equation 2.33 shows two groups of integral equations. Equation 2.33_1 shows that the displacement discontinuity $[u](x)$ can be written as the integral of a kernel $K(x,\xi)$ and a cohesive force law integrand $g([u](\xi),\xi)$. $K(x,\xi)$ only depends on the geometry and the eigenfunctions that governs the problem. The integrand $g([u](\xi),\xi)$ is the cohesive law with cohesive strength function characterizing initial defective and intact region. Equation 2.33_2 is a group of equilibrium equations each of which guarantees that a certain part of the system is equilibrated. S is the applied traction and $L(S)$ is the resultant by integrating the applied traction. Note that $f(\xi)$ is a geometry related function which arises from the integration of traction to get resultant. Equation 2.33 is a relatively compact representation of the problem, the actual algebraic equations to be solved requires subsequent treatment including eigenfunction expansion, mode truncation, and orthogonality, etc. It's worth pointing out that the two sets of nonlinear integral equations in 2.33 are coupled and generally need to be solved simultaneously, in which case, only numerical results can be used.

The use of exact elasticity solutions to analyze cohesive fracture problems was initiated and developed in several papers on the analysis of inclusion debonding and decohesion in different geometries subject to a number of different loadings (e.g., Levy, [77], [93], [94] and Levy and Hardikar [95]). Subsequently, the procedure was applied to layered composite systems subject to mode-I, mode-II loading (Chien and Levy [78], [79], [80]). Although originally developed to analyze debonding/decohesion and defect growth along interfaces separating distinct materials, the method can be used to analyze cohesive fracture in uniform material as long as the fracture surface can be specified a' priori ([78], [79], [80], [92], [96]). For the case of an interface defect in an inclusion-matrix system, Levy and Xie [88] analyzed the quasi-static defect growth process and interfacial stability (Fig.2.14).

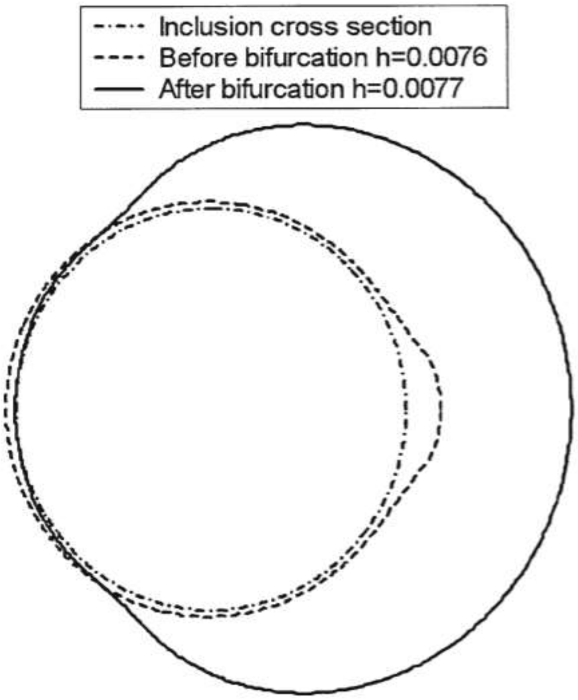

Fig.2.14 Cavity shape before and after bifurcation [88].(The term bifurcation, as in this work corresponds to snap cavitation.)

Note that the methodology is quite flexible and allows for a variety of cohesive force laws. One example of this is the structural interface which, in its original inception consists of linear trusses as shown in Fig.2.15 ([97], [98]). This model was modified by Chien and Levy to account for nonlinearity of the truss members in order to study the rupture of atherosclerotic plaques by interfacial debonding [99]. In that work a biomaterial interface, consisting of discrete integrin receptor proteins, connected a calcified cell with the extracellular matrix. The geometry is an elastic half-space (the extracellular matrix or plaque cap) containing a spherical inclusion (the calcification). The work revealed that when the inclusion is close to the cap-luminal boundary brittle interfacial decohesion precipitates an abrupt spike in circumferential stress in the thin layer of cap situated between the inclusion and luminal boundary. When this dynamic stress exceeds the cap strength, tearing occurs followed by thrombus formation and possibly infarction.

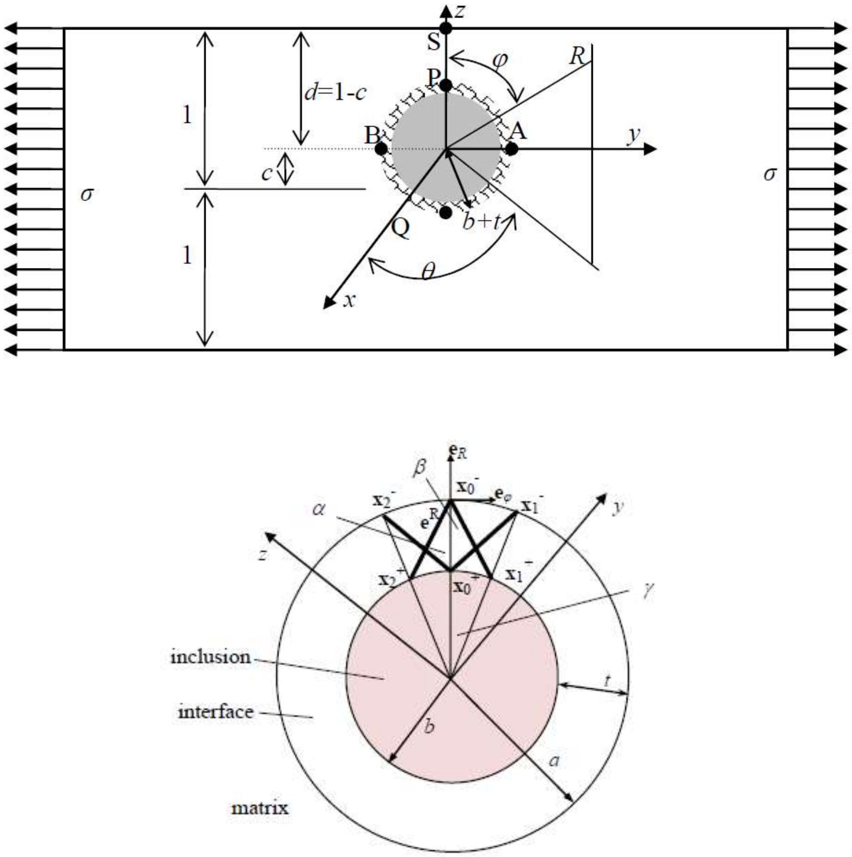

Fig.2.15 Local geometry of atherosclerotic plaques and structure interface with Warren truss.

In the following sections, a similar methodology is applied to cylinder and layered system to study the fundamental response of mode-III cohesive fracture. The detailed equation derivation process and numerical results will be presented.

3. Instability and Cohesive Fracture of a Torqued Cylindrical Bar[7]

This chapter mainly focuses on an idealized geometry that gives rise to pure mode-III fracture. The exact analysis is based on the solution of two elastic slender cylinders connected to each other end to end by a nonlinear cohesive surface. The loadings are equal and opposite torques on the top end of the top cylinder and the bottom end of the bottom cylinder (shown in Fig.3.1).

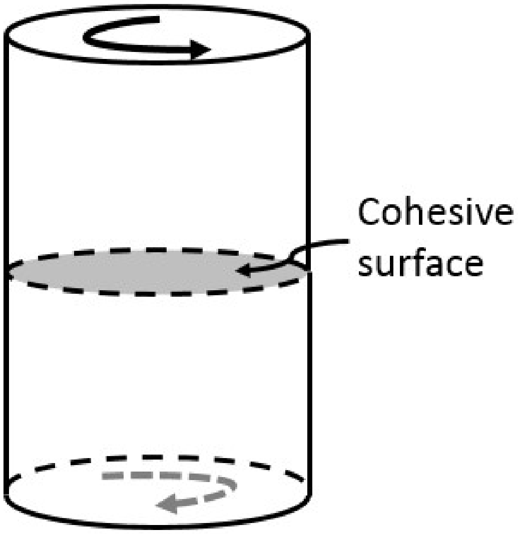

Fig.3.1 Cylinder model with cohesive surface.

The solution procedure outlined in previous Section 2.5 (while limited to infinitesimal strain, linear elastic bulk material and axisymmetric deformation) is applicable to a wide range of problems including cohesive surface stability and defect initiation and growth in a number of geometries. Generally, three issues will determine the kind of problem that is addressed.

i) *The cohesive relation.* Results based on the Xu-Needleman and bi-linear cohesive laws are presented and compared for certain problems. The Xu-Needleman relation in shear mode includes two constitutive parameters (the shear strength and a characteristic force length).

---

[7] The content of this chapter has been published in [92]

For problems requiring a constant shear strength τ_m, explicit results will be obtained using a value of *0.018* reflecting a relatively weak cohesive surface (recall that τ_m has been nondimensionalized by the shear modulus μ). This particular value is obtained from the following $\sigma_m/E=0.01$, $\tau_m/\sigma_m=0.7$, $\nu=0.285$ (here ν ("nu") represents Poisson's ratio as distinct from v which is the shear slip) that describes a cohesive surface which is slightly weaker in shear than in normal mode. The characteristic length has been chosen to be either *0.01* or *0.001* where the former (latter) characterizes ductile (brittle) cohesive surface behavior. When the bilinear cohesive relation is used, its constitutive parameter values are chosen so that they conform to the Xu-Needleman model, i.e., both laws have the same cohesive energy, cohesive strength and critical shear slip. Frictional response is modeled by adding a uniform compressive traction on the composite cylinder end caps. The frictional cohesive law can be obtained by coupling a static friction law to the cohesive relation. Depending on the relative magnitude of the cohesive strength and maximum friction traction, decohesion dominated and friction dominated response can be modeled within the same framework.

ii) Cohesive surface *uniformity.* Problems involving the stability of cohesive surfaces are analyzed with a constant ($\tau_{\max} = \tau_m$) reflecting a uniform cohesive surface. Cohesive surface nonuniformities are used to distinguish the bonded region and the initial defect region by setting the cohesive strength $\tau_{\max}(x)$ to be a function of cohesive surface coordinate. The idea of a nonuniform force law with a zero cohesive strength region to represent a crack was first implemented in [40], [65] for the problem of an initially cracked straight cohesive surface separating a block from a rigid substrate. Cohesive zone analyses of this type have been used in other types of problems as well including defect initiation and growth on a circular inclusion-matrix interface [88] and along straight cohesive surfaces in layered systems [78]. Apart from uniform cohesive surface, center, edge and annular (combination of the first two) defect geometries are studied in this chapter (Fig.3.2).

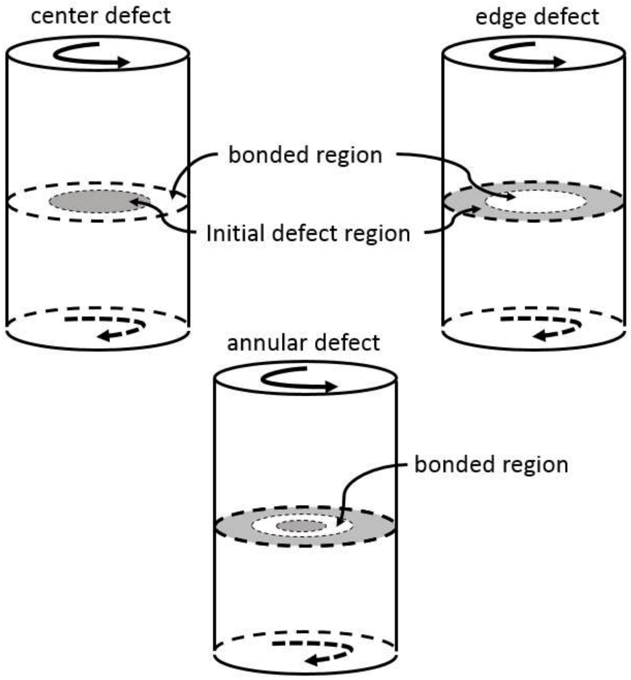

Fig.3.2 Three cohesive surface defect geometries.

iii) *Material homogeneity.* The only bulk material property related to the model is the shear modulus μ . Here, the focus is on a uniform material system or, a bilayer system so that in the later case, the top half has shear modulus μ_1 and the bottom half has shear modulus μ_2 . This requires that an additional parameter μ_1 / μ_2 be introduced. Material inhomogeneity within a layer will not be considered in this work.

The solution to the cohesive fracture of a finite or infinite slender cylindrical bar in torsion unfolds as follows. First, the infinitesimal strain solution to a relatively long[8] elastic cylinder subject to an

---

[8] The length of the cylinder is large compared to the radius.

arbitrary shear traction on one end and an equilibrating torque on the other is obtained by an eigenfunction expansion of the shear displacement field solution to the displacement equations of equilibrium. Next, for a nonlinear, nonuniform cohesive surface situated between two materially uniform cylinders, two single cylinder solutions are pieced together to obtain a nonlinear cohesive surface integral equation governing the cohesive surface slip field (tangential displacement jump). For a prescribed cohesive law, the integral equation, together with the integral equation of global moment balance, is solved by an eigenfunction expansion. This process yields modal equations governing mode multipliers of the cohesive surface shear slip field. In order to solve the equations, a program was written based on the Newton-Raphson method for a system of nonlinear equations and includes an integral solver for the numerical calculation of the mode multipliers. The shear slip field and corresponding interfacial traction field is obtained by post processing.

3.1 Elastic fields for arbitrary shear loading

The approach adopted in this work is to integrate Navier's displacement equation directly. (This solution was obtained independent of that of a similar problem solved by Lurie [100] using a different, and more complicated, approach that employs the Boussinesq potentials of three dimensional elasticity [101]). The approach adopted here is more suitable for our problem because it yields the displacement field directly whereas the Boussinesq potentials approach yields the stress field. For axisymmetric torsional deformation, assume that the displacement vector has only the circumferential component $u_\theta(r,z)$.

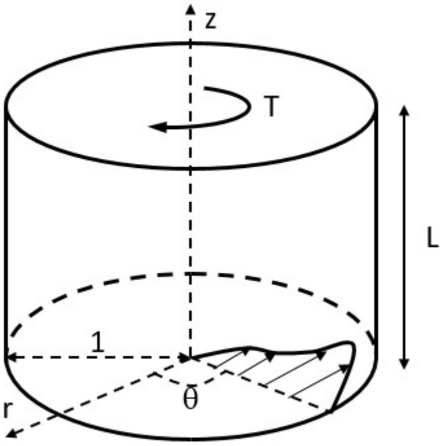

Fig.3.3 The cylinder under anti plane shear loading.

Navier's equation then becomes,

$$\frac{\partial^2 u_\theta}{\partial r^2} - \frac{1}{r^2} u_\theta + \frac{1}{r}\frac{\partial u_\theta}{\partial r} + \frac{\partial^2 u_\theta}{\partial z^2} = 0, \quad r \in (0,1),\ z \in (0, L) \tag{3.1}$$

where all quantities with dimensions of length have been nondimensionalized by the cylinder radius a. The nontrivial stress components associated with the circumferential displacement $u_\theta(r,z)$ are given by,

$$\sigma_{z\theta} = \frac{\partial u_\theta}{\partial z},\ \sigma_{r\theta} = \frac{\partial u_\theta}{\partial r} - \frac{u_\theta}{r} \tag{3.2}$$

Further note that all terms with dimensions of stress have been nondimensionalized by the shear modulus μ. The boundary conditions are:

i) strong (pointwise prescribed) boundary condition of vanishing traction on the lateral cylindrical surface $r=1$.

ii) strong (pointwise prescribed) boundary condition of prescribed shear traction on the surface $z=0$. Note this surface is to be defined as the cohesive surface when two cylinders are connected.

iii) weak (resultant prescribed) boundary condition of equilibrating torque on the upper surface $z = L$. Note this surface is to be defined as the surface where the external load is applied when two cylinders are connected.

These can be formulated as follows,

$$\begin{aligned}
&\sigma_{r\theta} = \frac{\partial u_\theta}{\partial r} - \frac{u_\theta}{r} = 0, \ r = 1 \\
&\sigma_{z\theta} = \frac{\partial u_\theta}{\partial z} = g(r), \ z = 0 \\
&\int_0^1 \sigma_{z\theta}(r,z) r^2 dr = T_0, \ z \uparrow \infty \text{ (semi-infinite bar) }, \ z = L \text{ (finite bar)}
\end{aligned} \tag{3.3}$$

where $g(r)$ (nondimensionalized by μ) is a prescribed function of radial coordinate r representing the arbitrary shear on one end. The torque T is nondimensionalized so that $T = 2\pi\mu a^3 T_0$. Note that L is nondimensionalized by the cylinder radius a and is such that $L \gg 1$. This last condition ensures that the details of the shear traction distribution $\sigma_{z\theta}$ on surface $z = 0$ will not be significantly affected by the stress distribution near $z = L$. Additionally, global moment equilibrium is ensured by requiring,

$$\int_0^1 g(r) r^2 dr = T_0 \tag{3.4}$$

The eigenvalue problem associated with equation (3.1) and (3.3) is of *singular Sturm-Liouville* type [87], and arises from the product solution $u_\theta(r,z) = R(r)e^{\pm\beta z}$ for the semi-infinite cylinder and $u_\theta(r,z) = R(r)[A\sinh(\beta z) + B\cosh(\beta z)]$ for the finite cylinder. It is given by,

$$\begin{aligned}
&\tilde{r}^2 R''(\tilde{r}) + \tilde{r}R'(\tilde{r}) + \left(\tilde{r}^2 - 1\right) R(\tilde{r}) = 0, \ \tilde{r} \in (0, \beta] \\
&\text{Lim } R, \ \textit{bounded} \ \tilde{r} \downarrow 0 \\
&\beta R'(\beta) - R(\beta) = 0
\end{aligned} \tag{3.5}$$

where $\tilde{r} = \beta r$, β is the separation constant and (3.5_1) is the *Bessel equation of order 1*. Note that (3.5_3) ensures the point wise satisfaction of vanishing shear tractions on the lateral cylinder surface (3.13_1). The eigenfunctions of (3.1) are,

$$\begin{aligned} &R_n(r) = C_n J_1(\beta_n r),\ n = 1,2,3,... \\ &R_0(r) = C_0 r,\ \beta_0 = 0 \end{aligned} \tag{3.6}$$

Where J_1 is the *Bessel function of the first kind of order 1* and use has been made of the identity $xJ'_\nu(x) = xJ_{\nu-1}(x) - \nu J_\nu(x)$ [102]. The eigenvalues are $\beta_0 = 0$ and $\beta_n,\ n = 1,2,3,...$ where β_n are the roots of the characteristic equation $J_2(\beta) = 0$. The first several roots are easily shown to be,

$$\beta_1 = 5.13562,\ \beta_2 = 8.41724,\ \beta_3 = 11.61984,\ \beta_4 = 14.79595,\ \beta_5 = 17.95982 \tag{3.7}$$

Since the eigenfunctions were generated from a Sturm-Liouville problem, they are orthogonal with respect to the weight function *r*. Thus,

$$\begin{aligned} &\int_0^1 rJ_1(\beta_n r)J_1(\beta_m r)dr = \frac{1}{2}\left[J_1(\beta_n)\right]^2 \delta_{mn},\ m,n = 1,2,... \\ &\int_0^1 r^2 J_1(\beta_n r)dr = 0,\ n = 1,2,... \end{aligned} \tag{3.8}$$

The solution for the displacement $u_\theta(r,z)$ can now be written as,

$$\begin{aligned} &u_\theta(r,z) = \omega_0 r + 4T_0 rz + \int_0^1 K(r,z,\rho)g(\rho)\rho d\rho \\ &K(r,z,\rho) = -\sum_{n=1}^{\infty} \frac{2J_1(\beta_n r)J_1(\beta_n \rho)}{\beta_n [J_1(\beta_n)]^2} e^{-\beta_n z} \quad \text{(semi infinite bar)} \\ &K(r,z,\rho) = -\sum_{n=1}^{\infty} \frac{2J_1(\beta_n r)J_1(\beta_n \rho)}{\beta_n [J_1(\beta_n)]^2 \tanh(\beta_n L)} \left[\cosh(\beta_n z) - \tanh(\beta_n L)\sinh(\beta_n z)\right] \quad \text{(finite bar)} \end{aligned} \tag{3.9}$$

where the additional boundary conditions (3.3$_2$), (3.3$_3$) have been imposed. Note that in (3.9), ω_0 represents an arbitrary rigid body rotation and T_0 is defined by $T_0 = \frac{T}{2\pi\mu a^3}$, the nondimensionalized torque.

The stress field follows directly from (3.3). It is interesting to note that for the semi-infinite cylinder the weak boundary condition of an applied torque at infinity gives rise to the stress distribution $\sigma_{\theta z} = 4T_0 r$. Furthermore, when $g(r)=g_0 r$ global moment equilibrium (3.4) implies that $g_0=4T_0$, the integral in (3.9$_1$) vanishes leaving an arbitrary rigid body rotation ω_0 , and the elementary solution of a torqued cylinder is recovered. A curious implication of the above results is that only the eigenfunction $R_0=C_0 r$ can be excited, i.e., apply $g=R_N(r)$ for some fixed N and obtain $u_\theta(r,z)$ proportional to $R_N(r)$. This is because global equilibrium cannot be satisfied as the integral is identically zero by (3.8$_2$).

3.2 Interfacial integral equations

Nonlinear interfacial integral equations. In this subsection, solution (3.9) is employed to develop integral equations governing the cohesive surface shear slip field, i.e., the discontinuity in tangential displacement across the surface. This is done by applying (3.9) to the upper and lower halves of the cylinder.

In order to obtain equations governing the shear slip field (displacement discontinuity field), first define the circumferential slip (circumferential displacement jump) as,

$$v(r) = [u_\theta](r) = \lim_{z\downarrow 0} u_\theta(r,z) - \lim_{z\uparrow 0} u_\theta(r,z) \tag{3.10}$$

where $v(r)$ is nondimensionalized by cylinder radius a. The first term on the right hand side of (3.10) is given by (3.9_1) evaluated at $z=0$. The second term on the right hand side of (3.10) can be shown to be identical to the first term provided we set,

$$K^{+}(r,\rho)=K(r,z=0,\rho),\ K^{-}(r,\rho)=-K(r,z=0,\rho) \tag{3.11}$$

and denote the rigid body rotation term as ω_0^{+} (ω_0^{-}) where a +(–) indicates a field associated with the upper (lower) half of the cylinder. Combining (3.9), (3.10), (3.11) and letting the interfacial shear traction g depend on the (unknown) interfacial slip v, as well as the radial coordinate, we get,

$$\begin{aligned} v(r) &= \omega r+\int_0^1 K(r,\rho)g(v(\rho),\rho)\rho d\rho \\ 0 &= -T_0+\int_0^1 g(v(\rho),\rho)\rho^2 d\rho \end{aligned} \tag{3.12}$$

where $K=K^{+}-K^{-}=2K^{+}$, $\omega=\omega^{+}-\omega^{-}$ and the global equilibrium balance (3.4) has been included as (3.12_2). Provided the cohesive surface shear g and the torque T_0 are prescribed, (3.12) forms a set of two nonlinear integral equations for two unknowns. One is the function $v(r)$ and the other is the constant, relative rigid body rotation ω, which is no longer arbitrary but governed by global equilibrium.

Modal equations. The solution to the system (3.12) for $v(r)$ is sought as an eigenfunction expansion of the form,

$$v=v_0 r+\sum_{n=1}^{\infty} v_n J_1(\beta_n r) \tag{3.13}$$

Direct substitution of (3.13) in (3.12) along with orthogonality relations (3.8) yields equations for the mode multipliers $v_n,\ n=1,2,\ldots$ and constant ω,

$$
\begin{aligned}
&0 = v_0 - \omega \\
&0 = v_m + \frac{4}{\beta_m \left[J_1(\beta_m)\right]^2} \int_0^1 J_1(\beta_m r) g(v_0, v_1, v_2, \ldots, r) r dr, \quad m = 1, 2, 3, \ldots \\
&0 = -T_0 + \int_0^1 g(v_0, v_1, v_2, \ldots, r) r^2 dr
\end{aligned}
\tag{3.14}
$$

If a finite number of terms, say N, are taken in the sum (3.13), then (3.14), together with the cohesive law, represents a set of $N+2$ equations for the $N+2$ unknowns ω, v_0, v_1, $v_2, \ldots, v_N$. The system of nonlinear equations is solved numerically by the Newton-Raphson method [103] which gives an approximate solution, the accuracy of which generally increases with an increasing number of modes. Higher order modes with small magnitudes that are close to system precision (set for the process of integration) do little but introduce noise and waste computation time. The balance between solution precision and computational burden introduced by increasing numbers of modes is sought by trial and error comparison. In this section, bifurcation plots and field plots are obtained with 20 modes of approximation. 50 modes approximations are used to determine the brittle cohesive surface traction field for comparison with static crack solutions taken from the literature.

Uniform linear spring cohesive surface*; an exact solution.* An exact, closed form solution to this problem can be obtained for the linear "spring" cohesive surface, i.e., $g=\alpha v$, α is a constant stiffness. Assume the solution $v=v_0 r$, where v_0 is constant. Then (3.12_1) implies that $v_0=\omega$ where use has been made of (3.8_2), (3.9), (3.11) and the fact that $K = 2K^+$. Global equilibrium (3.12_2) yields the slip $v = 4T_0 r / \alpha = 2Tr / \alpha\pi\mu a^3$ and the shear traction $g = 4T_0 r = 2Tr / \pi\mu a^3$.

3.3 The uniform cohesive surface; cohesive surface stability

A uniform cohesive surface means the cohesive law does not explicitly depend on the cohesive surface coordinate(s), i.e., the cohesive surface shear strength is a constant. The uniform cohesive surface assumption is used to study the response of weak cohesive surfaces where the effects of defects are negligible. Furthermore, in the uniform linear spring cohesive surface analysis, the system of nonlinear integral equations degenerates to one linear integral equation governing the classical torqued cylinder problem of linear elasticity. This can be used to check the validity of the numerical calculations.

For the uniform Needleman type cohesive surface, a bifurcation plot of maximum slip $v(r=1)$ versus normalized applied torque (T_0) for different values of force length δ is shown in Fig.3.4. A tangent bifurcation is seen to occur at a critical T_0 which coincides with the transition to unstable states of increasing separation at decreasing values of torque (and therefore failure of the cohesive surface). Bifurcations of this sort are not unusual for the Xu-Needleman force law [88]. However, the behavior indicated in the figure differs from other cases in that it does not appear to have the common "S" shape indicating a jump discontinuity in slip. This means that static behavior, i.e., the ability of the cohesive surface to support load, does not exist after the first transition. Note that with decreasing force length the transition becomes more brittle, i.e., cohesive surface failure occurs at smaller values of slip, without a significant decrease in the critical torque required to affect it.

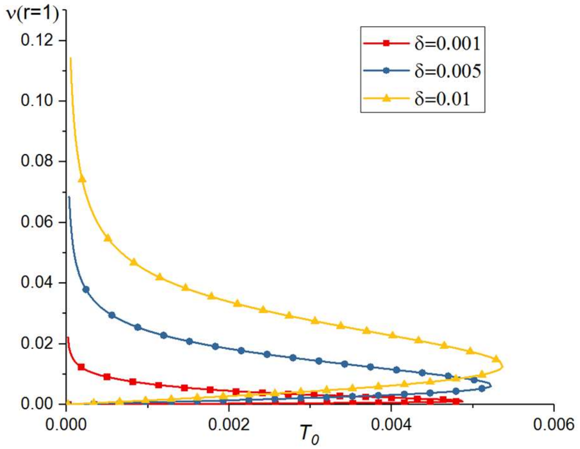

Fig.3.4 Bifurcation plot. Shear slip $\nu(r=1)$ and torque T_0. Uniform cohesive surface. $\tau_{\max}=0.018$.

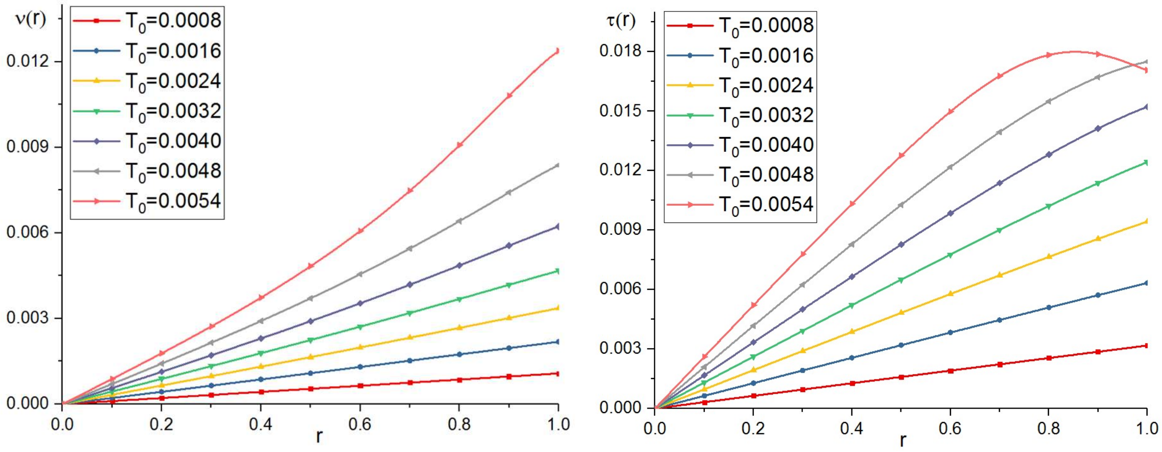

Fig.3.5 Shear slip $\nu(r)$ and shear traction $\tau(r)$. Uniform cohesive surface. $\tau_{\max}=0.018$, $\delta=0.01$.

It is not surprising that under relatively small torques, the cohesive surface shear traction and shear slip plots follow a linear pattern since most points of the surface are within the quasi-linear branch of the force law (Fig.3.5). As the applied torque increases, the outer radius (with the largest shear slip) first enters the nonlinear zone of the force law. Once the shear slip exceeds the characteristic length (δ), and enters the softening branch of the force law, shear traction starts to drop as shown by the top curve in the shear traction field plot of Fig.3.5. This contrasts with the classical torsion solution and the solution for the linear spring cohesive surface. In those cases, the maximum shear traction and shear slip fields are always linearly distributed so that the maximum values always occur at the outer radius.

By looking at the slip plot, it turns out that a one mode approximation to the slip field, i.e.,

$$v = v_0 r \tag{3.15}$$

captures many features of the essential physical behavior with minimum effort. The governing equation can be obtained by combining (3.16) with (3.14_3) and the force law and integrating to get,

$$0 = F(\alpha) = T_0 - e^{1/2}\tau_{\max}\alpha^{-3}\left[2-\left(\alpha^2+2\right)e^{-\alpha^2/2}\right] \tag{3.16}$$

where $\alpha = v_0/\delta$ and, as defined above, T_0 is a nondimensional measure of the applied torque (T) given by $T = 2\pi\mu a^3 T_0$. The nonlinear algebraic equation (3.16) has bifurcation points only if $dF/d\alpha = 0$. Applying this condition leads to the critical shear slip and critical torque at bifurcation,

$$\alpha_{cr} = 1.2704,\ T_{0cr} = 0.3115\tau_{\max} \tag{3.17}$$

Note that this point corresponds to complete failure of the cohesive surface as it indicates the transition to states of increasing slip under decreasing torque (Fig.3.4). Equation (3.17) yields a critical normalized torque of $T_0 = 0.0056$ (provided $\tau_{\mathrm{m}} = 0.018$) which is a good approximation of the transition point in Fig.3.4. This is underscored by the fact that the single mode solution predicts a critical torque independent of the characteristic length which is clearly erroneous.

3.4 Center, edge and annular defect growth in uniform and bi-cylinders

In this subsection, cohesive surface nonuniformities in the form of initial axially symmetric center (penny shaped), edge (ring shaped) and annular (combination of first two) defects (Fig.3.2) are considered by assuming that the cohesive strength is a function of radial coordinate in the general form,

$$\tau_{\max}(r) = \begin{cases} \tau_m, & r \in \text{ initial perfect region} \\ 0, & r \in \text{ initial imperfect region} \end{cases} \tag{3.18}$$

The nonuniform cohesive surface; the penny shape (*edge*) *defect.* In the case of the edge defect, (3.18) assumes the form,

$$\tau_{\max}(r) = \begin{cases} \tau_m, & 0 < r < \xi_0 \\ 0, & \xi_0 < r < 1 \end{cases} \tag{3.19}$$

where ξ_0 is the initial core radius (normalized by cylinder radius *a*). In following calculations unless specified, we will take ξ_0 to be *0.8*.

Figure.3.6 contains bifurcation curves for the nonuniform cohesive surface with edge defect using the Xu-Needleman force law and the bi-linear force law. For comparison purposes the force law parameters were chosen to have identical cohesive surface energy, cohesive strength and critical slip. The plot reveals the effect of the force law shape on the stability behavior. It is no surprise that the behavior predicted by the bi-linear force law is similar to that of the Xu-Needleman law since they share the same physical parameters (same fracture energy density, cohesive strength and critical slip). Furthermore, note that the smaller the characteristic force length (i.e., the more brittle the cohesive surface) the better the consistency between the bi-linear and Xu-Needleman force laws. This can be explained by the fact that the differences of bi-linear and Xu-Needleman exponential force law mainly are around the top of the force law maximum which represents material yielding. A larger yielding region in the cohesive force law will increase the discrepancy between the fields predicted by the two different force laws. This argument also addresses the necessity for a more precise characterization of force laws when analyzing ductile cohesive surfaces.

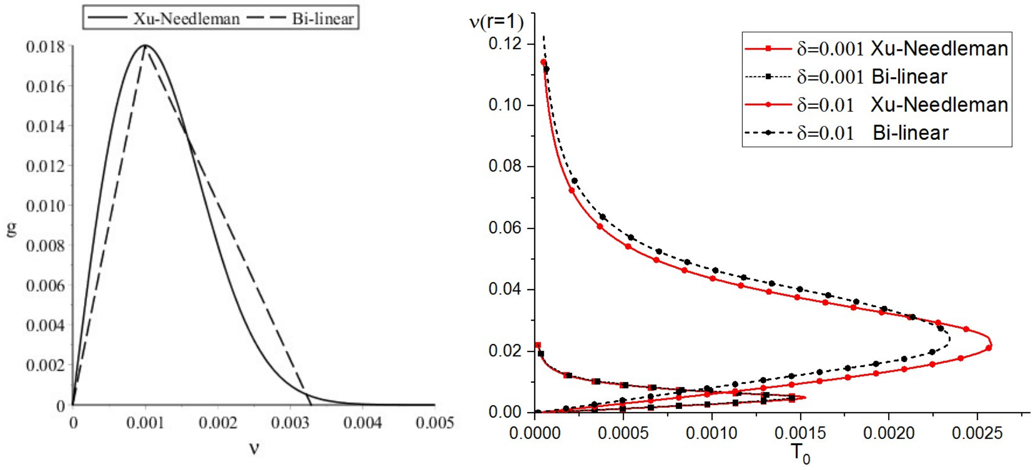

Fig.3.6 a) Xu-Needleman law and corresponding Bi-linear law. b) Bifurcation plots for the Xu-Needleman and bi-linear force laws (edge defect).

By comparison with Fig.3.4 (bifurcation plot of uniform cohesive surface), Fig.3.6 shows that nonuniform cohesive surfaces have a similar stability behavior (a critical torque separating stable and unstable branches that lead to total failure). However, unlike uniform cohesive surfaces, where the characteristic length has little effect on the bifurcation torque, a significant drop is observed for the nonuniform brittle cohesive surface. This is consistent with the common-sense idea that an initial defect on a brittle cohesive surface is more dangerous than on a ductile cohesive surface due to its higher stress concentration.

Figure.3.7 depicts the shear slip distribution and shear traction distribution at different values of torque for a relatively brittle cohesive surface (small δ). Taken together the figures indicate behavior that is readily identifiable with sharp crack growth, i.e., a diminishing core region with negligible slip, and a concomitant shear traction that monotonically increases from zero at the core center followed by an abrupt drop off outside the core.

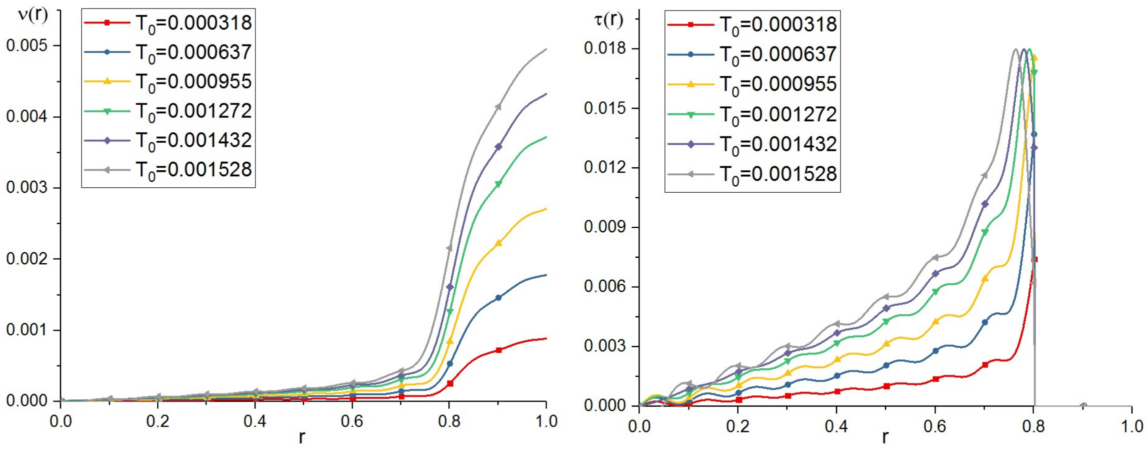

Fig.3.7 a) Shear slip field. b) Shear traction field. δ=0.001.

By way of contrast, consider Fig.3.8 which depicts the shear slip/traction distributions of a more ductile cohesive surface (large δ).

In order to quantify quasi-static defect growth within the framework of cohesive fracture we will need to define the location of the defect tip. This is not always straightforward owing to i) the somewhat amorphous definition of defect tip within the cohesive surface formulation (note that the X-N exponential type force law does not have finite decohesion cutoff length and it is not suitable for defect tip defined by vanishing traction), ii) the fact that cohesive laws characterize a range of separation/slip phenomena (e.g., Fig.3.7 and Fig.3.8) not all of which can be identified with the growth of a defect.

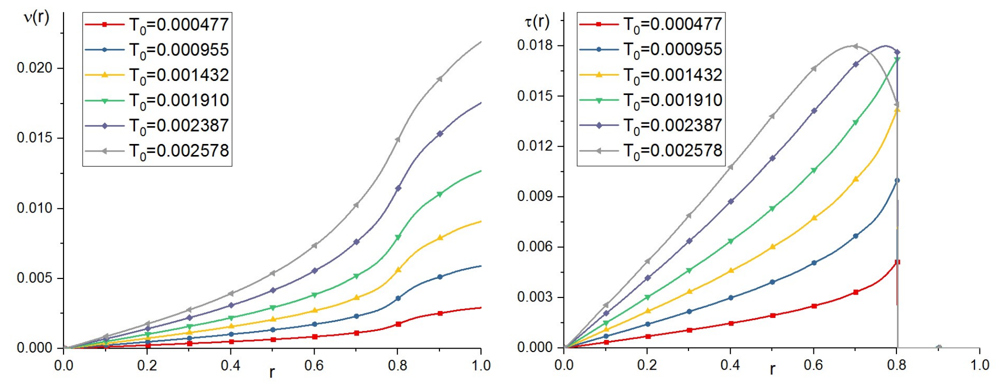

Fig.3.8 a) Shear slip field. b) Shear traction field. δ=0.01.

For the later, we simply note that a clear picture of defect extension will occur only for certain parameter values, namely high cohesive surface stiffness (small force length parameter). Regarding item i) much of the difficulty concerns growth under mixed mode loading which is not relevant to the present work (see [78], [88] for further discussion of this issue). One approach to resolve this issue is to define the location of the defect tip by an onset criterion for defect propagation whereby a critical shear slip needs to be attained for growth. In the present work only one slip mode is active and the location of the defect tip ξ is be defined by the condition that the slip at that point attains a critical value, i.e., $v(\xi) = \delta$. Because we are dealing with a single mode this criterion coincides with the maximum shear stress condition that $g(v(\xi)) = \tau_{\max}$. Finally, it is noted that there will generally be two critical loads to consider. One is the *initiation torque* T_{0i} which is defined to be the smallest torque required to cause the defect to extend and the other is the *bifurcation torque* T_{0c} which is that torque which signals the transition to states of increasing slip at decreasing values of torque, i.e., cohesive surface instability or failure. The related notion of *defect length* is defined by $\zeta(T_0) = \xi_0 - \xi(T_0)$ and is such that i) $\xi(T_0 = 0) = \xi_0$, ii) $\zeta(T_0 = 0) = 0$ and iii) $d\zeta / dT_0 \uparrow \infty$ at a finite value of torque (bifurcation torque). Fig.3.9 is a plot of defect length (ζ) versus torque for two different values of force length parameter δ. The figure indicates that the initiation torque and the bifurcation torque both decrease for more brittle cohesive surfaces (smaller δ 's). Furthermore, the figure indicates that the amount of growth prior to failure is less for brittle cohesive surfaces.

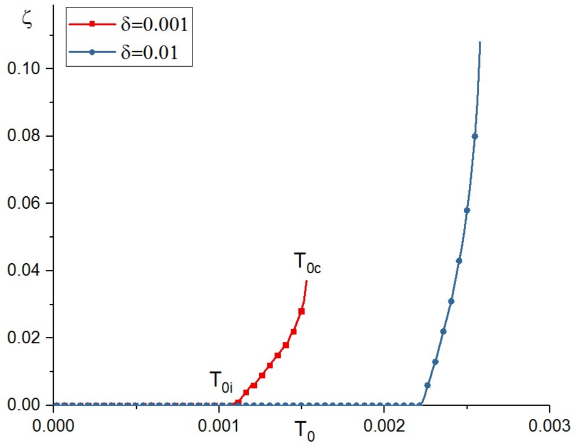

Fig.3.9 Defect length (ζ) versus torque.

The static fracture mechanics solution of Benthem and Koiter [104], for the torsionally loaded cylindrical bar containing an annular defect, can be used to check the quality of the solution presented herein. Note however that the classical crack solution can only provide the near tip static field and gives no insight into the defect growth process. For this reason, the parameter values of the present solution, which gives the full field along with defect growth, will need to be tuned to values appropriate for static crack like behavior. Thus, consider a stiff[9] (small δ), strong (large $\tau_{\max}$) cohesive surface under a small applied torque, i.e., ($\delta = 0.001,\ \tau_{\max} = 0.018$). The Benthem and Koiter (BK) solution for the axisymmetric shear stress on the crack plane is given by,

$$\begin{aligned} \sigma_{\theta z} &= \frac{4}{\sqrt{2}} K T_0 \frac{(1-\xi_0)^{1/2}\, \xi_0^{-5/2}}{(\xi_0 - r)^{1/2}}, \\ K &= \frac{3}{8}\left(1 + \frac{1}{2}\xi_0 + \frac{3}{8}\xi_0^2 + \frac{5}{16}\xi_0^3 + \frac{35}{128}\xi_0^4 + 0.208\xi_0^5\right) \end{aligned} \tag{3.20}$$

Where $\sigma_{\theta z}$ has been nondimensionalized by the shear modulus μ, ξ_0 is the nondimensional core radius (which locates the defect tip from the cylinder axis) and T_0 is the nondimensional torque.

---

[9] Recall that for cohesive force laws (3.4) the initial stiffness $dg/dv|_{v=0}$ is proportional to τ_m/δ.

Fig.3.10 depicts the static BK solution along with the cohesive solution obtained for three different values of torque. As expected the curves indicate excellent agreement between the two solutions at the smallest value of torque considered. The solutions begin to diverge for larger values of torque owing to the extension of the defect in the cohesive fracture solution. Furthermore, the cohesive solution gives an accurate description at and near the core center (*r=0*) where the shear stress distribution must vanish.

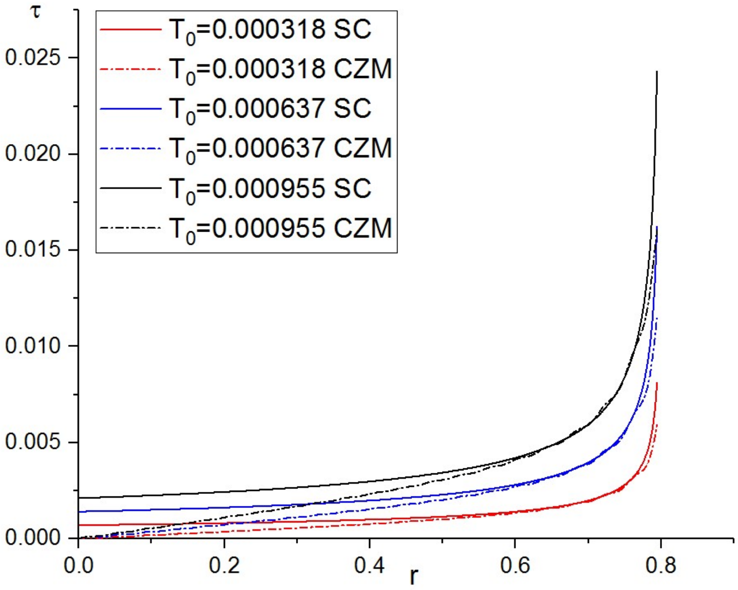

Fig.3.10 Static crack solution (SC) vs cohesive fracture solution (CZM).

The nonuniform cohesive surface; the penny shape (*center*) *defect.* In the case of a penny shape defect, the cohesive surface nonuniformity has an expression similar to (3.20) but with the perfect and imperfect regions switched, i.e.,

$$\tau_{\max}(r)=\begin{cases}0, & 0<r<\xi_0\\ \tau_{\mathrm{m}}, & \xi_0<r<1\end{cases} \tag{3.21}$$

From Fig.3.7 and Fig.3.8, we can conclude that for the edge defect, growth is inward from the tip of the initial defect. This occurs because the defect driven concentration of stress occurs at the outer most radius of the bonded material. For the center defect we might expect outward growth from the defect tip however this might not be true because, while defect driven stress concentration occurs at the defect tip, the cylindrical geometry and torsional loading indicate larger shear slip and shear traction at the outer radius. Thus, there is a competition between the elevated shear traction occurring at the inner radius caused by the defect and, the elevated shear traction occurring at the outer radius due to torsional deformation. Similar to the edge defect, the maximum shear slip occurs within the initial defect zone. Figures 3.11 and Fig.3.12, for the penny shaped defect, show a qualitative difference in behavior due to the difference in characteristic lengths. For $\delta=0.001$ (Fig.3.11), the behavior is defect dominated. The shear traction and shear slip field concentration are at the defect tip (r=0.8) and the defect will grow outward towards the outer radius. However, for $\delta=0.01$ (Fig.3.12), before the bifurcation torque, the shear traction and the shear slip at the outer radius have already become comparable (or greater than) that at the defect tip. This fact indicates that the formation of a new defect may occur at the outer radius. The cohesive surface would therefore be degraded by both the initial defect growing outward and the newly formed defect (at the outer radius) growing inward. This finding motivates the contents of the next section which mainly focuses on a discussion of the sequence of defect initiation.

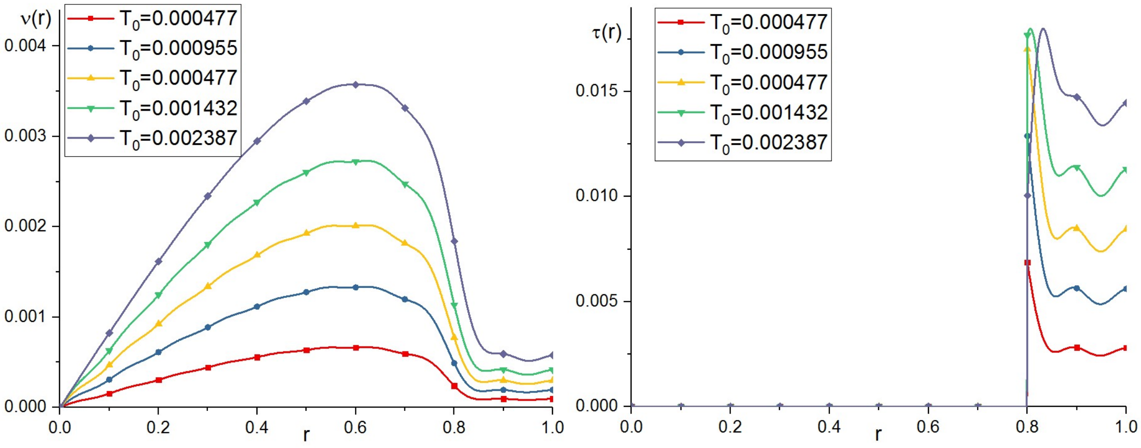

Fig. 3.11 a) Shear slip field. b) Shear traction field. δ=0.001.

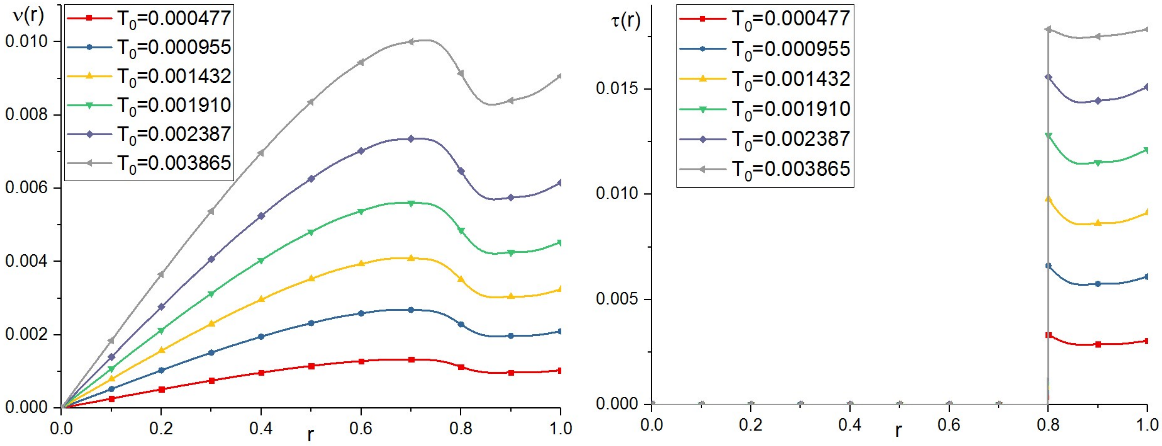

Fig.3.12 a) Shear slip field. b) Shear traction field. δ=0.01

The nonuniform cohesive surface; two initial defect fronts (*annular defect*). For the cohesive surface with an annular defect characterized by (3.22),

$$\tau_{\max}(r)=\begin{cases}0,\ 0<r\le\xi_0\\ \tau_m,\ \xi_0<r\le\xi_1\\ 0,\ \xi_1<r\le 1\end{cases}\tag{3.22}$$

the cohesive strength step function appearing in the definition is approximated by a combination of smooth hyperbolic functions. The function $\tau_{\max}(r)=\frac{-\tau_m}{2}\left[\tanh(\gamma(\xi_0-r))+\tanh(\gamma(r-\xi_1))\right]$, where γ measures the ascent slope, is used to approximates (3.22) (all calculations were carried out with a γ value of 200). This is done in order to boost computational efficiency since calculating the values of smooth functions is faster than evaluating nested conditional statements. Two issues not present in the edge and penny-shaped defect analyses occur in this case. The first involves the cohesive surface loading capacity and how it changes as the bonded region shrinks, the second concerns the sequence of propagation of the two initial defect fronts.

Figure.3.13 depicts how altering the location of an initial defect front affects the load capacity of the cohesive surface. The blue curve shows that increasing the radius of the inner defect front ξ_0

(fixing the outer defect front at $\xi_1 = 0.95$) has little effect on the critical torque since material at the inner radius carries a reduced amount of interfacial shear. However, decreasing the radius of the outer defect front ξ_1 (fixing the inner defect front at $\xi_0 = 0.20$) leads to a significant drop in the critical torque (orange curve).

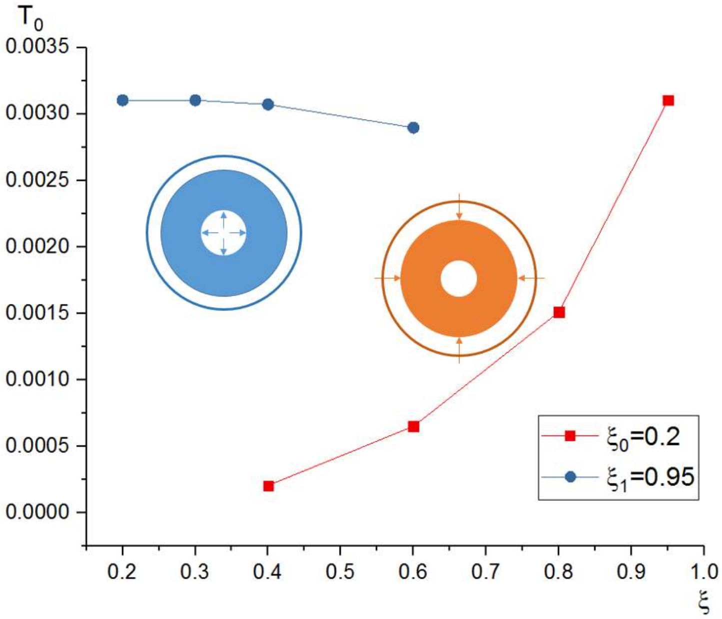

Fig.3.13 Annular defect geometry and its influence on the critical torque maximum.

Comparison of the cohesive fracture solution (CFS) to the static crack solution (SCS) is indirect because the annular defect solution for the sharp crack does not, to the best of our knowledge, appear in the literature. An approximate solution for the sharp crack can be obtained by superimposing the Benthem and Koiter solution [1] for two different crack geometries. However, the approximation ignores crack tip interaction which will lead to erroneous results when two crack fronts are close to each other. The cohesive surface shear distribution for the cohesive fracture solution and the corresponding superimposed sharp crack solution are given in Fig.3.14 for different initial inner defect front locations. Figure.3.14 shows that for a relatively large bonded region, the SCS and the CFS give similar predictions for the stress distribution, i.e., the outer defect front is subject to a higher stress concentration which in turn would be the first to propagate. However, for a relatively small bonded region (bottom right of Fig.3.14), the CFS and the SCS, as expected, diverge because the SCS cannot predict crack tip interaction. It is worth noting that, in such cases, the stress concentration at the inner defect front has already become comparable to the outer one which leads to the issue of the sequence of defect propagation. Figure.3.15 addresses this question by

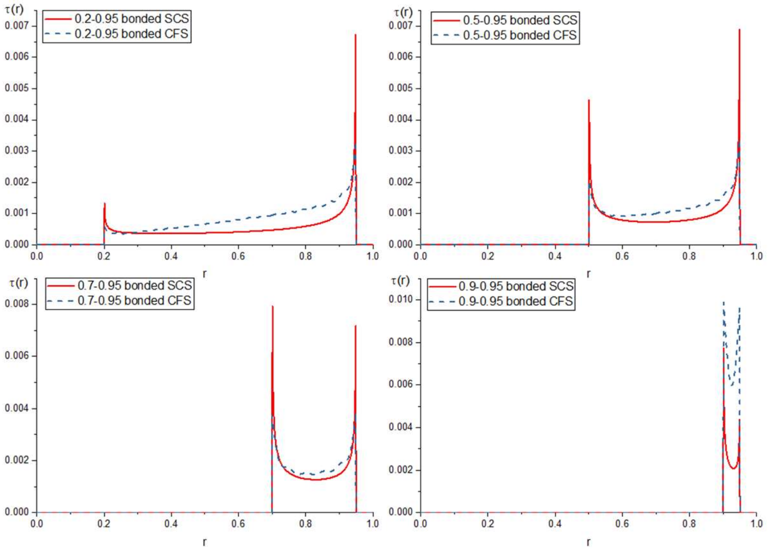

Fig.3.14 CFS vs SCS for different initial inner defect front locations.

depicting the defect growth process for annular bonded regions of radial thickness 0.1 situated at different locations within the cross section. Note that each curve terminates at the critical torque maximum. For an annular bonded region close to the core, only the outer defect front will propagate. However, when the bonded region is located towards the outer radius, the inner defect front will eventually propagate as well (Fig.3.15 left line of 0.8-0.9 bonded region).

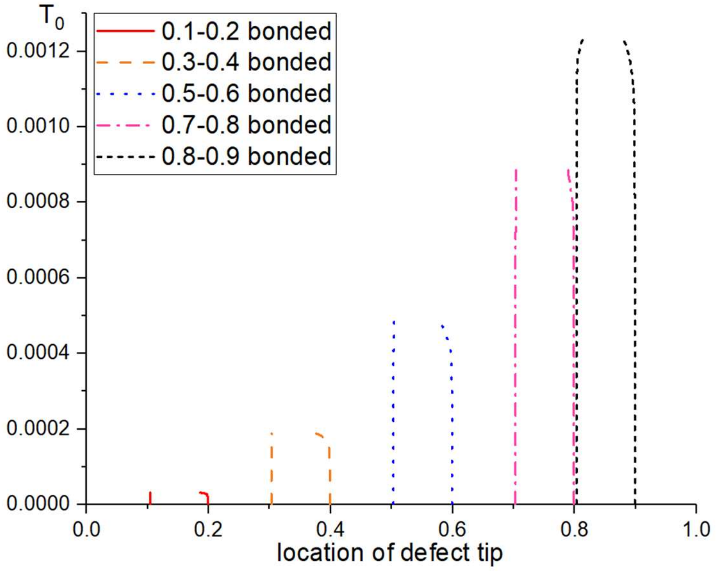

Fig.3.15 Defect tip locations.

The formulation presented in this paper is readily applicable to the bi-cylinder problem, i.e., the problem of two cylinders made of different material bonded together by an infinitesimal thin layer of adhesive along a common interface. The adhesive can spread along the whole cross sectional area (uniform interface) or cover just part of it(nonuniform interface). In the process leading to the governing integral equations (3.12), one merely keeps track of the different shear moduli of the upper and lower halves of the cylinder. Thus, for the uniform cylinder, quantities with the dimensions of stress are nondimensionalized by shear modulus μ . For the bi-cylinder a second shear modulus μ_2 is introduced and this is also nondimensionalized by shear modulus $\mu_1 = \mu$. Figure.3.16 shows that the bi-cylinder shares the same defect propagation processes as the uniform cylinder (increasing slip with increasing load, torque maximum leading to interface/cohesive surface failure). For the uniform interface, the shear slip-torque plots are very similar regardless of shear modulus ratio μ_2 (Fig.3.16a). However, for the nonuniform interface (Fig.3.16b), significant differences in the torque maximum are observed. For increasing values of μ_2, the curves seem to converge. This can be explained by considering the problem of a compliant cylinder resting on a rigid foundation whose behavior should be dominated by the compliant material (curves for $\mu_2 = 1.0$ and $\mu_2 = 2.0$ curves are close). Because the cohesive strength is normalized by $\mu_1 = \mu$, small μ_2 ($\mu_2 < 1$) makes the interface weaker and more compliant leading to a drop of interface load capacity (curves for $\mu_2 = 0.5, 0.1$ versus $\mu_2 = 0.1$).

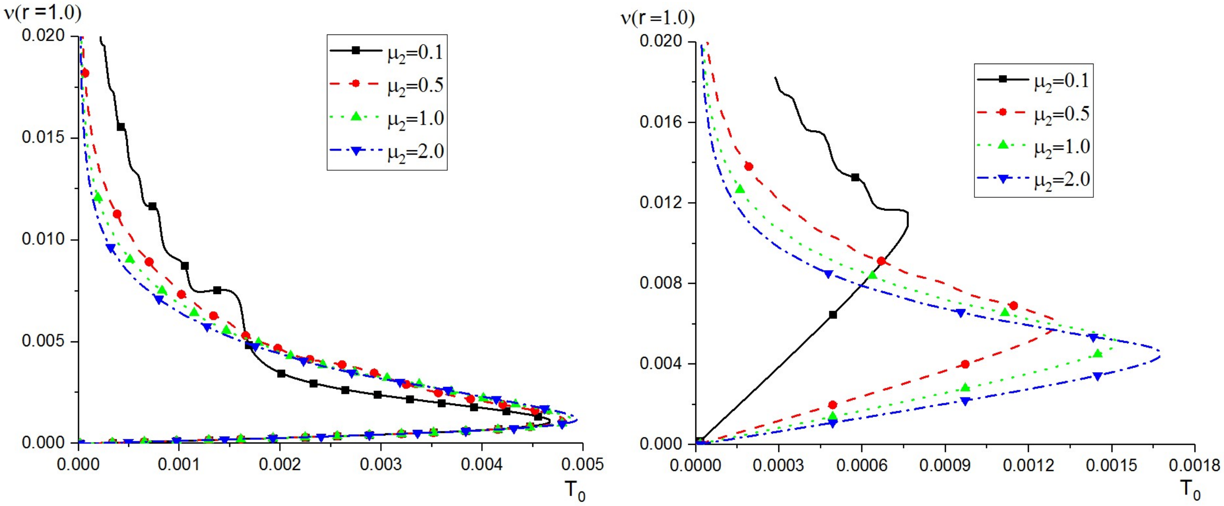

Fig.3.16 Interface shear slip $v(r=1)$ vs torque T_0 for the bi-cylinder.

a) Uniform interface, b) Nonuniform interface.

3.5 Principal stress and mode-I micro cracks

Micro-cracks oriented at certain angles to the primary fracture plane have been observed in numerous cylinder torsional experiments [33], [35], [105]. The coalescence and extension of these micro-cracks leads to an array of new repetitive oblique secondary crack planes which resembles a factory roof. The *factory roof pattern* is a common phenomenon in mode III+I testing of brittle materials such as PMMA. A careful study of such crack configurations not only helps to understand the formation of rupture zones but i) reveals a more general fracture initiation process, ii) shows the effects of mode-III/I mixity on fracture behavior, iii) explains how mode-I micro-cracks deviate from the primary fracture plane and finally, iv) shows its effects on bulk material behavior after the primary crack tip moves. Knauss [105] did experiments on brittle materials (solithane) under mode-III dominated loading (torsion of cylinder with edge razor cut), and showed that the crack front fragments into multiple cracks oriented at 45° with respect to the primary crack plane. He concluded that these cracks are mode-I cracks generated by the maximum principal tensile stress. Based on a series of testing with microscopic observation and finite element analysis, Cox and Scholz [33] pointed out that the rupture zone of mode-III cracks is formed by an array of oblique tensile micro-cracks at the tip of the primary initial crack. This argument is in accordance with the maximum tensile stress criterion for mixed fracture proposed by Erdogan and Sih [106] when the crack direction is not predetermined. Cox and Scholz also predicted a 45° angle (ϕ) between the micro-crack plane and primary fracture plane.

The cohesive zone analysis of the previous sections can be used to shed light on mode-I micro-crack formation by examining the maximum principal tensile stresses and their locations. Recall that for the cylinder problem, subject to a remote torque, the only two non-vanishing stress components are $\sigma_{r\theta}$ and $\sigma_{z\theta}$. Stress tensor manipulation yields the magnitude of the principal tensile stress and its associated principal direction,

$$\sigma_p = \sqrt{\sigma_{r\theta}^2 + \sigma_{z\theta}^2} \qquad \left[\frac{\sigma_{r\theta}}{\sqrt{2\left(\sigma_{r\theta}{}^2 + \sigma_{z\theta}{}^2\right)}},\ \frac{1}{\sqrt{2}},\ \frac{\sigma_{z\theta}}{\sqrt{2\left(\sigma_{r\theta}{}^2 + \sigma_{z\theta}{}^2\right)}} \right] \tag{3.23}$$

The oblique mode-I micro defect plane is perpendicular to the principal tensile stress direction given in (3.23) and its intersection line with the local θ-z plane at the primary fracture tip is shown in top figure in Fig.3.17. The bottom figure of Fig.3.17 shows the idealized stress state of an element subjected to only $\sigma_{z\theta}$, the corresponding direction of principal stress and mode-I micro defect plane with ϕ=45°.

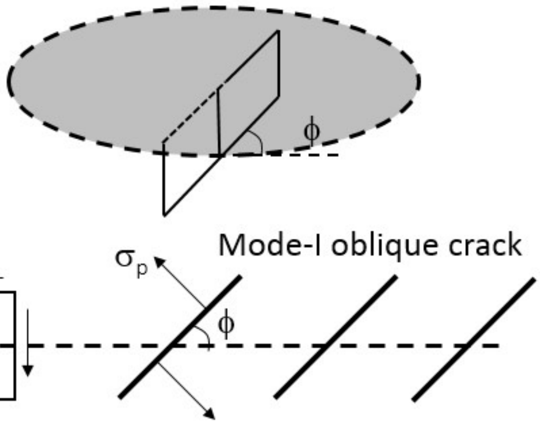

Fig.3.17 Oblique mode I micro cracks.

The existence of the stress component $\sigma_{r\theta}$ can be demonstrated by the following argument. For an edge cracked cohesive surface, the moment resultant of the shear traction on the defect plane must equilibrate the applied torque on the top end cap. Now take a free body diagram of a fictitious internal cylinder with radius slightly ahead of the crack tip (Fig.3.18). This shows that the decrease in torque carried by the reduced top surface area (on the free body) must be picked up by shear traction $\sigma_{r\theta}$ component on the lateral surface (of the free body). Note that the resultant of the shear traction on the defect plane is unchanged. The difference of the load carried by the cohesive surface and the equivalent torque on the reduced top surface reaches its maximum at the initial defect tip. In the vicinity of this location, the cohesive surface stress state predicts that $\sigma_{r\theta}$ is comparable to $\sigma_{z\theta}$ which makes the angle deviate from 45° as shown in Fig.3.19. At a smaller radius (except close to core when $\sigma_{z\theta}$ is also very small) $\sigma_{z\theta}$ dominates and the angle is very close to 45°. For points beyond the defect tip ($r > \xi_0$), the angle quickly increases to 90° because $\sigma_{z\theta}$ decreases abruptly to zero and $\sigma_{r\theta}$ becomes the dominant term. The cohesive zone analysis just described gives a more precise explanation for the orientation of oblique mode-I micro-cracks. The prediction of approximately 45° oblique mode-I micro cracks agrees with experiment and FEM analysis from the literature [35], [107], [108].

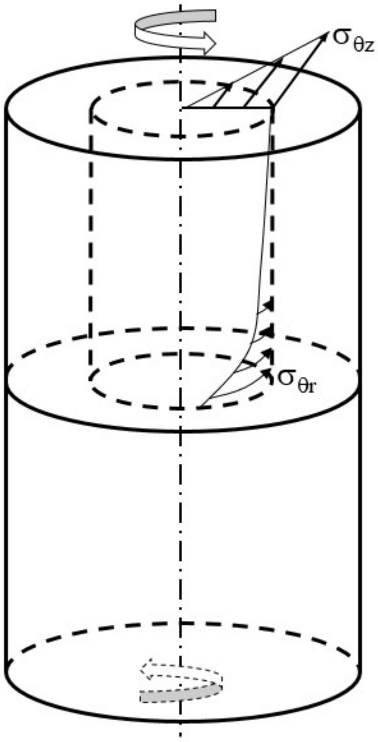

Fig.3.18 Fictitious internal cylinder (dotted) with radius just behind the defect tip.

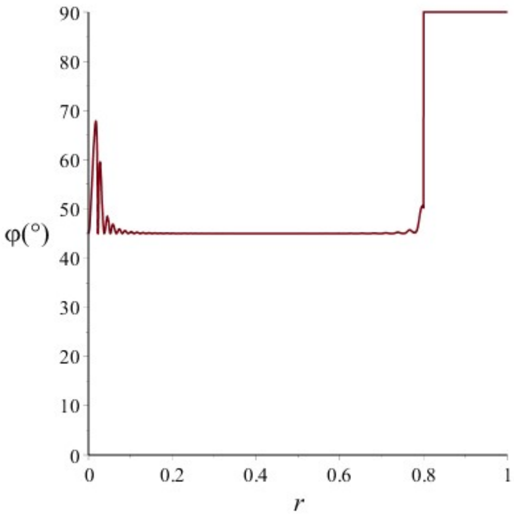

Fig.3.19 Orientation of mode I micro defects obtained from the cohesive zone analysis.

3.6 Characterization of frictional cohesive surface and corresponding response

The transition from cohesion to sliding friction during contact is a key dissipative mechanism in cohesive zone approaches dealing with frictional cohesive surfaces [109], e.g., fiber pull out in composite materials [111]. An early attempt to combine cohesion and frictional contact [60] treated decohesion and friction as decoupled sequential processes (the cohesive surface is assumed to be frictionless until complete decohesion after which friction is activated). Other theories, such as initiating frictional response when the load is first applied [61] or, from the onset of fracture, have also been proposed [63].

For the torqued cylindrical bar, friction on a parallel cut section will not occur. In order to introduce a friction mechanism into the present formulation (without introducing additional sources of shear slip) i) the loading is modified to include a compressive traction that is uniformly distributed on the cross section and ii) the cylinder is assumed to be materially uniform (so there is no slip at the cohesive surface arising from differential contraction). The modified cohesive law (g_m) is then assumed to be the sum of a cohesive part (g) and a superimposed frictional part (f), i.e., $g_m = g + f$.

Furthermore, the frictional part of the force law is taken to be zero for a range of values of slip less than a critical value. Beyond this point the frictional part rapidly increases to its maximum uniform value determined by the friction coefficient and the normal compressive traction. This step-like behavior (shown in Fig.3.20) is modelled by a hyperbolic trigonometric function [63],

$$f = \begin{cases} 0, & 0 < \nu < \alpha\delta \\ f_{\max} \tanh\left(\lambda(\nu - \alpha\delta)\right), & \alpha\delta < \nu \end{cases} \tag{3.24}$$

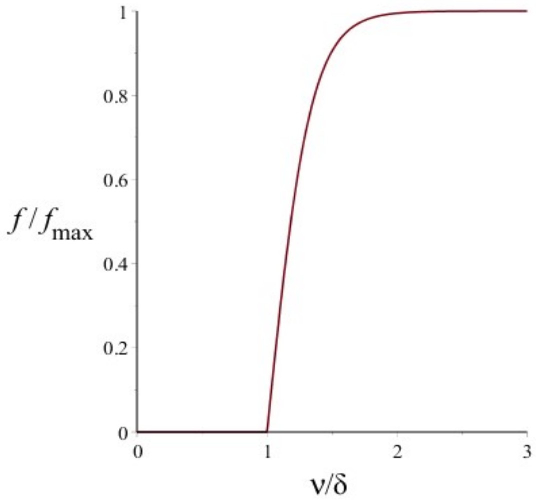

Fig.3.20 Frictional branch of cohesive law approximated by a hyperbolic trigonometric function. $\alpha = 1$.

where $f_{\max}$ is the maximum friction force which is dependent on the friction coefficient and the compressive traction. Parameters α and λ are two dimensionless constitutive parameters that characterize the shape of frictional part. Parameter α controls when the frictional response begins while parameter λ determines how fast the curve rises to its maximum friction value (slope of ascending branch in Fig.3.20). There are generally two kinds of qualitatively different behaviors, i.e., i) decohesion dominated response and ii) friction dominated response. The first occurs when there is a small amount of friction (maximum friction force less than maximum cohesive force, e.g., $f_{\max} = 0.3\tau_m$), the second when there is a larger amount of friction (maximum fiction force greater than the maximum cohesive force, e.g., $f_{\max} = 1.5\tau_m$). The frictional cohesive force law for both cases is presented in Fig.3.21. Corresponding shear slip-torque plots are shown in Fig.3.22. For the decohesion dominated case (Fig.3.22a), the general shape is similar to previous frictionless cases except that i) the stable branch has a pronounced decrease in slope (at around T_0=0.0003) and ii) the unstable branch will not decrease to zero applied torque. The reason for the turning point is that some points on the cohesive surface have already entered the region where friction is active, and the introduction of friction tends to stiffen the cohesive surface leading to a decrease in slope of slip vs normalized applied torque curve . In case ii), the unstable branch will not decrease to zero applied torque since even for large shear slip, the shear traction would attain the persistent maximum friction force. For the friction dominated

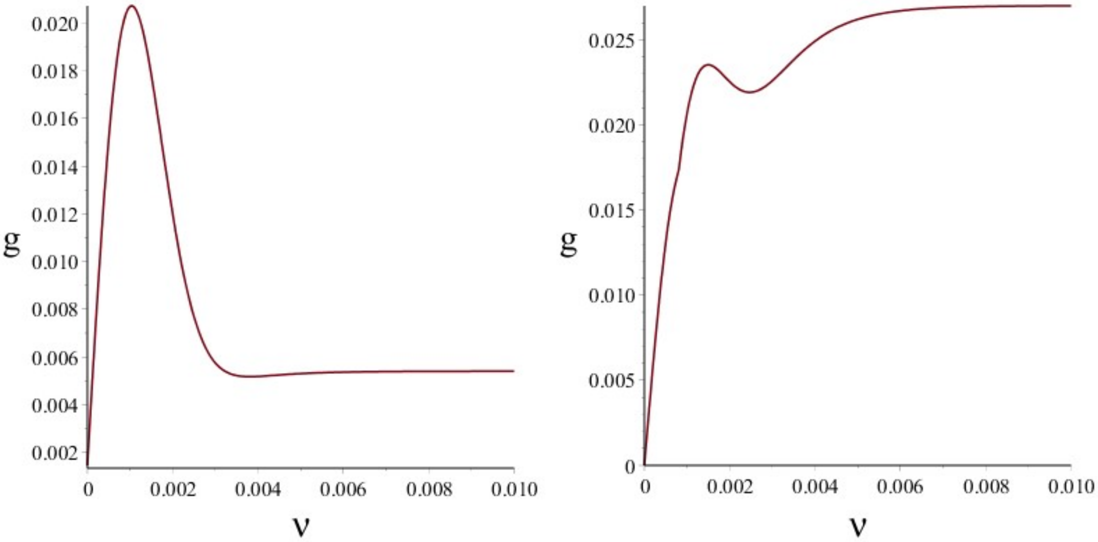

Fig.3.21 Frictional cohesive force law($\tau_m = 0.018, \delta = 0.001$, α=0.8, $\lambda = 500$.). a) Decohesion dominated ($f_{\max} = 0.3\tau_m$), b) Friction dominated ($f_{\max} = 1.5\tau_m$).

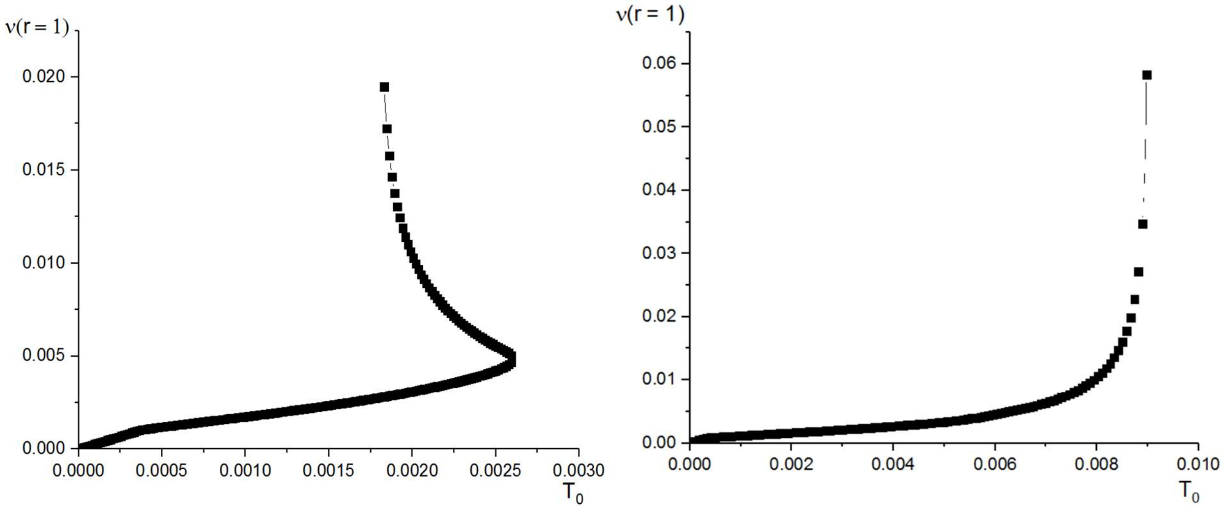

Fig.3.22 Shear slip $\nu(r=1)$ vs torque T_0. Edge defect ($\xi_0 = 0.8$).

a. Decohesion dominated. b. Friction dominated.

cohesive surface (Fig.3.22b) the behavior appears to be qualitatively different then decohesion dominated response. This is because there does not appear to be a critical torque maximum. The cohesive surface will still fail as it appears that the slope of the curve becomes unbounded at a finite value of torque. However, the exact behavior beyond the last computed point of Fig.3.22b is unknown because i) the curve is almost vertical leading to a breakdown of the Newton Raphson process and ii) the slip magnitude may be beyond the infinitesimal strain assumption.

4 Instability and Cohesive Fracture of the Two-Sublayer System

The basic procedure used to derive the governing integral equations for layered systems is similar to that of the cylinder case treated previously. Note the term “sublayer” in this work represents the medium on one side of the cohesive surface. The two-sublayer system can be used to model, i) a materially uniform layer containing a line defect (the layer is separated into two sublayers by the plane of defect) and, ii) the interfacial defect between two different media. The single sublayer solution is obtained subject to arbitrary, strong (pointwise prescribed) boundary conditions. Cohesive surface integral equations are obtained by piecing together the solutions for two or more sublayers.

4.1 Elastic fields for arbitrary shear loading

Anti-plane shear of a sublayer subjected to arbitrary, but equilibrated, strong tractions on opposing surfaces. Consider a plane rectangular sublayer (Fig.4.1), infinite in extent in the direction normal to the plane, with coordinates of points referred to a Cartesian coordinate system. The only anti-plane displacement component is $u_z(x,y)$. The Navier-Cauchy equilibrium equation in the absence of body force is $(1-2\nu)\nabla^2\mathbf{u}+\nabla div\mathbf{u}=\mathbf{0}$ which, for anti-plane shear, becomes,

$$\frac{\partial^2 u_z(x,y)}{\partial x^2}+\frac{\partial^2 u_z(x,y)}{\partial y^2}=0,\ x\in(\text{-}1,1),\ y\in(\text{-}h,h) \tag{4.1}$$

which is the two-dimensional Laplace equation in a rectangular domain. Recall that all quantities with dimensions of length have been nondimensionalized by the layer half-width. Nontrivial stress components (normalized by shear modulus μ) are given by,

$$\sigma_{zx}=\frac{\partial u_z}{\partial x},\ \sigma_{zy}=\frac{\partial u_z}{\partial y} \tag{4.2}$$

Strong boundary conditions on top and bottom surfaces can be formulated as,

$$\begin{aligned}
&\sigma_{zy} = \frac{\partial u_z}{\partial y} = g(x),\ y = h \\
&\sigma_{zy} = \frac{\partial u_z}{\partial y} = f(x),\ y = -h \\
&\sigma_{zx} = \frac{\partial u_z}{\partial x} = 0,\ x = \pm 1
\end{aligned} \tag{4.3}$$

where $g(x)$ and $f(x)$ are prescribed shear tractions on the top and bottom surfaces written as functions of coordinate x.

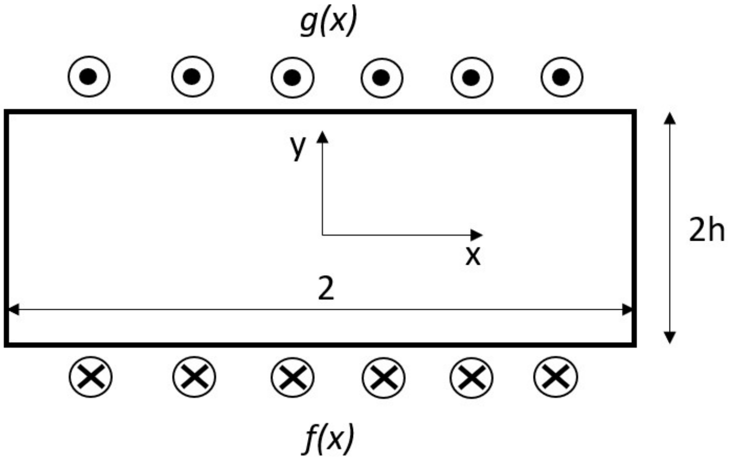

Fig.4.1The single sublayer.

Note that global force equilibrium requires that

$$\int_{-1}^{1} f(x)dx = \int_{-1}^{1} g(x)dx \tag{4.4}$$

The eigenvalue problem obtained from (4.1), (4.2) and (4.3) is of *regular Sturm-Liouville* type [87] given by,

$$\begin{aligned}
&X''(x) + \beta^2 X(x) = 0 \\
&\frac{\partial X(x)}{\partial x} = 0,\ x = \pm 1
\end{aligned} \tag{4.5}$$

The fundamental set of solutions to (4.5$_1$) is $\sin(\beta x)$ and $\cos(\beta x)$. For the remainder of this work a symmetric geometry, with loading symmetric about the y,z plane, is assumed. The eigenvalues and eigenfunctions are therefore,

$$\begin{aligned} &X_n(x) = C_n \cos(\beta_n x),\ n = 1,2,3... \\ &X_0(x) = D_0,\ n = 0 \\ &\beta_n = n\pi,\ n = 1,2,3... \end{aligned} \tag{4.6}$$

Because the layer is assumed to have a finite thickness the product solutions are written in the form,

$$\begin{aligned} &u_{z,n}(x,y) = X_n(x)[A_n \sinh(\beta_n y) + B_n \cosh(\beta_n y)] \quad n = 1,2,...,N \\ &u_{z,0}(x,y) = X_0(x)[A_0 + B_0 y] \end{aligned} \tag{4.7}$$

where hyperbolic functions have replaced exponential functions.

Combine (4.6) and (4.7), the displacement and stress fields can be rewritten as,

$$\begin{aligned} &u_z(x,y) = D_0 + C_0 y + \sum_{n=1}^{\infty}\left[C_n \cos(\beta_n x)\sinh(\beta_n y) + D_n \cos(\beta_n x)\cosh(\beta_n y)\right] \\ &\sigma_{yz} = \frac{\partial u_z(x,y)}{\partial y} = C_0 + \sum_{n=1}^{\infty}\left[C_n\beta_n \cos(\beta_n x)\cosh(\beta_n y) + D_n\beta_n \cos(\beta_n x)\sinh(\beta_n y)\right] \\ &\sigma_{xz} = \frac{\partial u_z(x,y)}{\partial x} = \sum_{n=1}^{\infty}\left[-C_n\beta_n \sin(\beta_n x)\sinh(\beta_n y) - D_n\beta_n \sin(\beta_n x)\cosh(\beta_n y)\right] \end{aligned} \tag{4.8}$$

Apply strong boundary conditions (4.3$_{1,2}$) and isolate C_n and D_n coefficients to get,

$$\begin{aligned} &C_0 + \sum_{n=1}^{\infty} C_n\beta_n \cos(\beta_n x)\cosh(\beta_n h) = \frac{f(x)+g(x)}{2} \\ &\sum_{n=1}^{\infty} D_n\beta_n \cos(\beta_n x)\sinh(\beta_n h) = \frac{g(x)-f(x)}{2} \end{aligned} \tag{4.9}$$

The direct integration of (4.9$_1$) yields

$$C_0 = \int_{-1}^{1} \frac{f(x)+g(x)}{4} dx \tag{4.10}$$

Explicit expressions for individual C_n and D_n coefficients, in terms of integrals of *f(x)* and *g(x)*, follow directly from the orthogonality of the eigenfunctions. A rearrangement of terms enables the displacement field (4.8_1), in a single sublayer subject to arbitrary but equilibrated shear tractions on the top and bottom surfaces, to be written in the integral form,

$$\begin{aligned}
u_z(x,y) &= D_0 + \int_{-1}^{1} K_1(\zeta,x,y)g(\zeta)d\zeta + \int_{-1}^{1} K_2(\zeta,x,y)f(\zeta)d\zeta \\
K_1 &= \frac{y}{4} + \sum_{n=1}^{\infty}\left[\frac{\cos(\beta_n\zeta)}{2\beta_n\cosh(\beta_n h)}\sinh(\beta_n y) + \frac{\cos(\beta_n\zeta)}{2\beta_n\sinh(\beta_n h)}\cosh(\beta_n y)\right]\cos(\beta_n x) \\
K_2 &= \frac{y}{4} + \sum_{n=1}^{\infty}\left[\frac{\cos(\beta_n\zeta)}{2\beta_n\cosh(\beta_n h)}\sinh(\beta_n y) - \frac{\cos(\beta_n\zeta)}{2\beta_n\sinh(\beta_n h)}\cosh(\beta_n y)\right]\cos(\beta_n x)
\end{aligned} \tag{4.11}$$

where D_0 is an arbitrary rigid body displacement. Note ζ is a dummy variable of integration in the x direction.

4.2 Interfacial integral equations

In this subsection, interfacial integral equations are derived for the two-sublayer system. Representation of these equations as a finite set of nonlinear algebraic *modal* equations suitable for numerical solution will be obtained as well.

The two-sublayer system. The two-sublayer system consists of two sublayers of identical width and depth, but generally different thicknesses, separated by a cohesive surface. This system can be analyzed by considering the two sublayers separately (Fig.4.1) and employing the solution developed in the previous section (Fig.4.2). Thus, apply (4.11) to the top and bottom layers[10] and define the cohesive surface displacement discontinuity (shear slip) as,

---

[10] A +(-) indicates quantities associated with the top(bottom) layer.

$$v(x) = [u_z](x) = Lim\ u_z^+(x, y^+ \downarrow -h^+) - Lim\ u_z^-(x, y^- \uparrow h^-)\ . \tag{4.12}$$

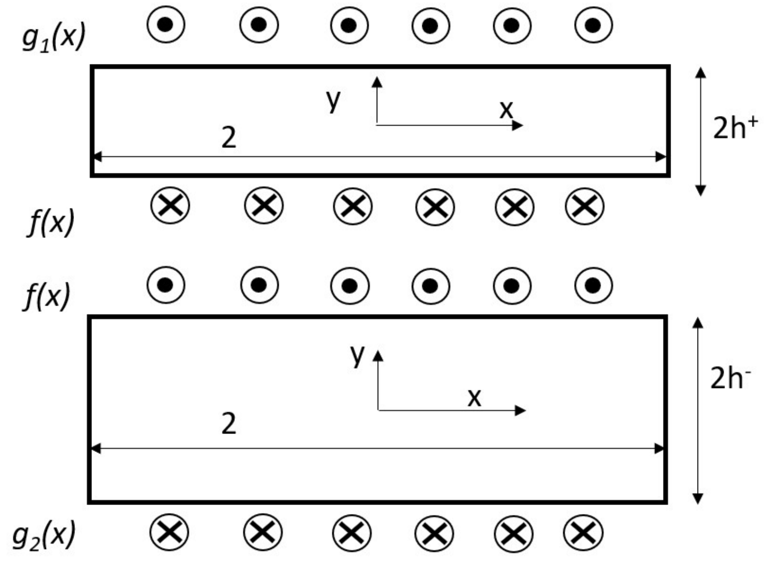

Fig.4.2 The two-sublayer system.

The displacement fields of the top and bottom layers can be written as,

$$\begin{aligned} u_z^+ &= D_0^+ + \int_{-1}^{1} K_1(\zeta, x, y) g_1(\zeta) d\zeta + \int_{-1}^{1} K_2(\zeta, x, y) f(\zeta) d\zeta \\ u_z^- &= D_0^- + \int_{-1}^{1} K_1(\zeta, x, y) f(\zeta) d\zeta + \int_{-1}^{1} K_2(\zeta, x, y) g_2(\zeta) d\zeta \end{aligned} \tag{4.13}$$

Substitute equation (4.13) into (4.12) and evaluate on the cohesive surface to yield the expression for the shear slip

$$\begin{aligned} &v(x) = v_R + \int_{-1}^{1} K_1(\zeta, x) g_1(\zeta) d\zeta + \int_{-1}^{1} K_{12}(\zeta, x) f(\zeta) d\zeta - \int_{-1}^{1} K_2(\zeta,) g_2(\zeta) d\zeta \\ &K_{12}(\zeta, x) = K_2(\zeta, x, -h^+) - K_1(\zeta, x, h^-) \\ &K_1(\zeta, x) = K_1(\zeta, x, -h^+) \\ &K_2(\zeta, x) = K_2(\zeta, x, h^-) \\ &v_R = D_0^+ - D_0^- \end{aligned} \tag{4.14}$$

In (4.14), geometry dependent kernels K_1 and K_2 are given by (4.11) and functions $g_1(\zeta), g_2(\zeta)$ are prescribed shear tractions on top and bottom surfaces. Constant v_R is a rigid body translation term governing the relative rigid displacement of the top layer with respect to the bottom layer. Global equilibrium for the two-sublayer system is satisfied provided an equilibrated system of shear tractions is applied to the top and bottom surfaces of the layer. Rigid body equilibrium for a single sublayer constrains the relative rigid body movement of one sublayer with respect to the other. This has to be actively enforced. Thus, (4.14_1) must be supplemented with the rigid body equilibrium equation,

$$0=\int_{-1}^{1} f(\zeta)d\zeta-\int_{-1}^{1} g(\zeta)d\zeta \tag{4.15}$$

(It can be shown that the satisfaction of (4.15) for one sublayer, together with an equilibrated set of applied shear tractions, implies satisfaction of rigid body equilibrium for the other sublayer.) Note that for a cohesive surface problem, $f(v)$ is defined by a particular cohesive law. In order to solve (4.14) and (4.15), they must first be reformulated as a set of nonlinear algebraic equations. In order to do this, write the solution as an expansion in eigenfunctions of the kernels K_1, K_2, i.e.,

$$v(x)=\sum_{n=0}^{\infty} v_n \cos(\beta_n x) \tag{4.16}$$

where the $\{v_n, n=0,1,2,\ldots\}$ are unknown mode multipliers. Introduce $D_0 = D_0^{+} - D_0^{-}$, $\bar{h} = \frac{1}{2}\left(h^{+} + h^{-}\right)$ for simplicity. Apply orthogonality,

$$
\begin{aligned}
&0 = v_0 - v_R + \bar{h}\int_{-1}^{1} g_1(x)dx \\
&0 = v_n + \frac{\int_{-1}^{1} g_1(x)\cos(\beta_n x)dx}{2\beta_n}\left[\tanh(\beta_n h^+) - \coth(\beta_n h^+)\right] + \frac{\int_{-1}^{1} g_2(x)\cos(\beta_n x)dx}{2\beta_n}\left[\tanh(\beta_n h^-) - \coth(\beta_n h^-)\right] \\
&\qquad \frac{\int_{-1}^{1} f(v(x),x)\cos(\beta_n x)dx}{2\beta_n}\left[\tanh(\beta_n h^+) + \tanh(\beta_n h^-) + \coth(\beta_n h^+) + \cot(\beta_n h^-)\right] \\
&0 = \int_{-1}^{1} f(v_0, v_1, ..., v_n, x)dx - \int_{-1}^{1} g_1(x)dx \\
&n = 1, 2, ..., N
\end{aligned}
\tag{4.17}
$$

If N terms are taken in the sum (4.16), and the cohesive law is given as a function of x and $v(x)$, then (4.17) represents a set of $N+2$ equations for $N+2$ unknowns $v_R, v_0, v_1, ..., v_n$.

4.3 The uniform cohesive surface; surface stability

In this subsection numerical results are presented for several two-sublayer or materially nonuniform bilayer systems with different defect configurations, material properties and layer thicknesses. In all cases it is assumed that the shear tractions applied to the top and bottom surfaces are uniform and the defects are symmetric in the width direction.

Uniform cohesive surface; the bifurcation problem. For the cylinder in torsion, the traction distribution depends on the radial coordinate even when the cohesive surface is uniform, i.e., without defects. This causes difficulties in obtaining the exact solution to the bifurcation problem. However, in the case of the layered system, there is a uniform traction distribution in the absence of defects. This can be demonstrated as follows (Fig.4.3).

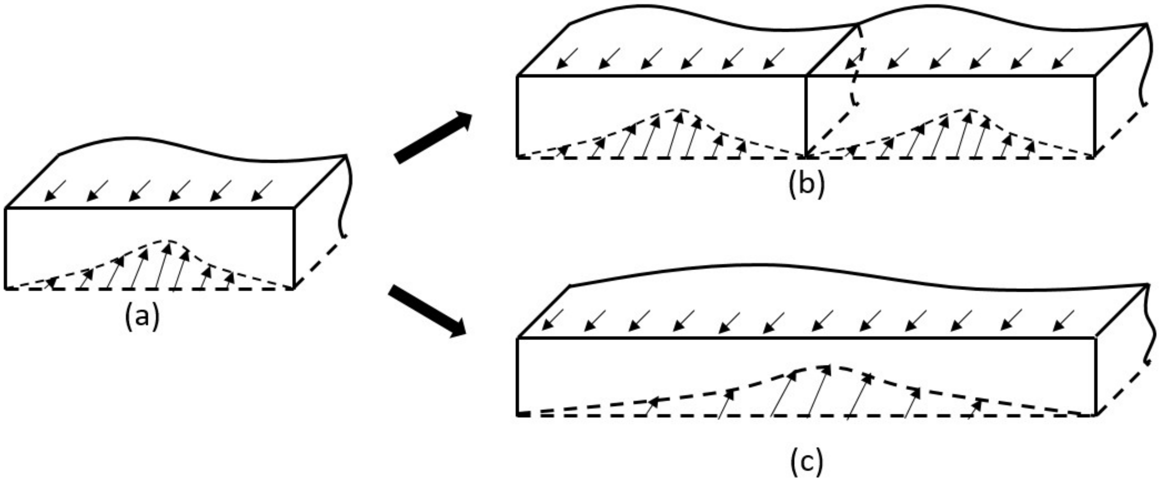

Fig.4.3 Explanation of uniform solution for a uniform cohesive surface.

Suppose a two-sublayer system, subject to a uniform applied shear traction S on its upper surface, has a nonuniform but equilibrated shear traction on the cohesive surface as shown in Fig.4.3(a). The solution to a similar problem of twice the width as (a) can be obtained by simply connecting two original geometries side by side shown in Fig.4.3(b). This can be done because the tractions of the side surfaces vanish. Scaling the solution of (a) would generate a similar traction pattern as Fig.4.3(c). Because the traction distribution in Fig.4.3(a) is arbitrary, the uniqueness theorem of linear elasticity [110] implies that the original traction distribution is uniform. Based on this argument the interfacial shear slip is uniform and governed by (4.17$_1$) and (4.17$_3$), i.e.,

$$\begin{aligned} 0 &= v_0 - v_R + 2\bar{h}S \\ 0 &= f(v_0) - S \end{aligned} \tag{4.18}$$

If the two-sublayer system is load controlled and the cohesive surface is of uniform X-N exponential type , then the slip v_0 and the relative rigid body displacement v_R can be obtained from (4.18) and (2.17), i.e.,

$$
\begin{aligned}
v_0 &= \delta\sqrt{-W\left(-e^{-1}\left(\frac{S}{\tau_{\max}}\right)^2\right)} \\
v_R &= \delta\sqrt{-W\left(-e^{-1}\left(\frac{S}{\tau_{\max}}\right)^2\right)} + 2\bar{h}S
\end{aligned}
\tag{4.19}
$$

where W is the multivalued Lambert W function [112]. Figure.4.4 is a plot of solution (4.19_1). The graph depicts a *load maximum* or *tangent bifurcation* and is characterized by two distinct branches, a stable branch (increasing slip under increasing load) and an unstable branch (increasing slip under decreasing load). This behavior is similar to that which occurs in the mode-III deformation of a cylindrical bar in torsion (Fig.3.4). Note that due to the multi-valued nature of the Lambert W function, the solution to the load control problem is generally multi-valued. This will not cause any ambiguity for the two-sublayer system subjected to monotonically increasing load from the reference state.

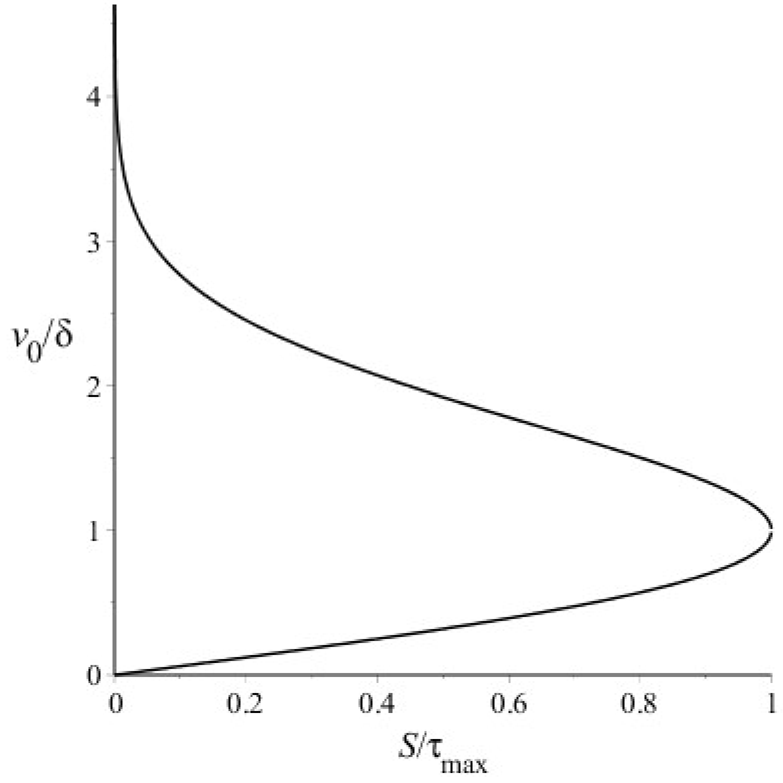

Fig.4.4 Uniform cohesive surface response.

However, in layered systems with more than one cohesive surface, multi-valued solutions can lead to asymmetric deformation and more complex bifurcation behavior.

4.4 Center and edge defect fields in uniform two-sublayer

The formulation presented is applicable to many different defect configurations and loadings. In this section the focus is on, i) two-sublayer systems that reveal fundamental aspects of defect growth behavior and, ii) solutions that can be tested against classical SIF solutions that exist in the literature. Thus, the problems considered below are i) a materially uniform layer containing a small defect (both center and edge) symmetrically placed with respect to the top and bottom surfaces, ii) a materially nonuniform bilayer system containing an interface defect and, iii) a uniform layer or nonuniform bilayer system containing a defect that is not symmetrically distributed with respect the top and bottom surfaces (i.e., the sub surface defect problem), iv) a symmetric linear array defect, v) a frictional interface.

Center defect. Fig.4.5 is a two-sublayer system with identical thicknesses and material properties containing a single center defect situated on the cohesive surface separating the two sublayers. The parameter ξ_0 characterizes the ratio of defect length to sublayer half-width so that the coordinate dependent cohesive strength function is given by,

$$\tau_{\max}(x)=\begin{cases}\tau_{\mathrm{m}} & \text{otherwise}\\ 0 & -\xi_0\le x\le\xi_0\end{cases}\tag{4.20}$$

(Recall that all lengths are nondimensionalized by layer half width). Unless otherwise noted the following parameter values will be used in calculations, $h=0.5$, $\xi_0=0.1$ which represents a relatively small defect length and a relatively thick layer. These values are chosen so that boundary effects are mitigated, and solutions can be compared with the infinite plate or semi-infinite plate static crack tip fields of linear elastic fracture mechanics.

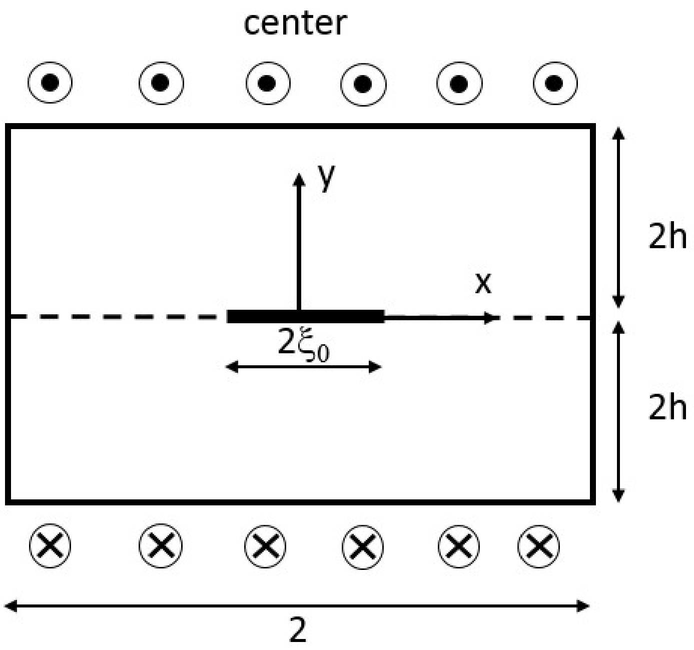

Fig.4.5 Bilayer system with center defect.

Fig.4.6 shows bifurcation curves for different characteristic lengths. The general behavior is similar to the torqued cylinder case, i.e., a critical applied shear traction characterizes the transition from stable to unstable states. For load control, once the critical shear traction is reached, the cohesive surface cannot carry any more load and the defect plane fails.

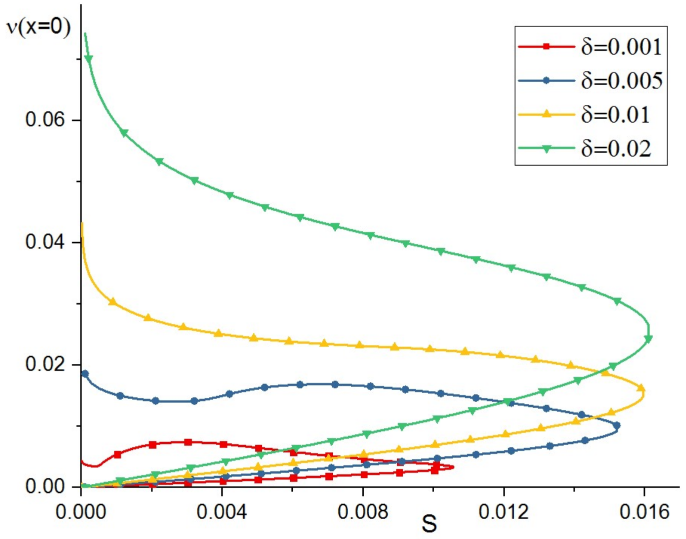

Fig.4.6 Bifurcation plot.

Figure 4.7 depicts the shear traction field ($\tau(x) = f(v(x),x)$) and the shear slip field ($v(x)$) for the brittle cohesive surface. Symmetry about the y-z plane allows the fields to be plotted only for $x \geq 0$. Note the strong stress concentration near the defect tip representing "sharp crack-like" defect growth. By contrast, Fig.4.8 shows a ductile cohesive surface (large δ) with a more distributed traction and slip field. The failure of the cohesive surface is no longer "sharp crack-like" defect growth but generally tends to a more uniform slip process.

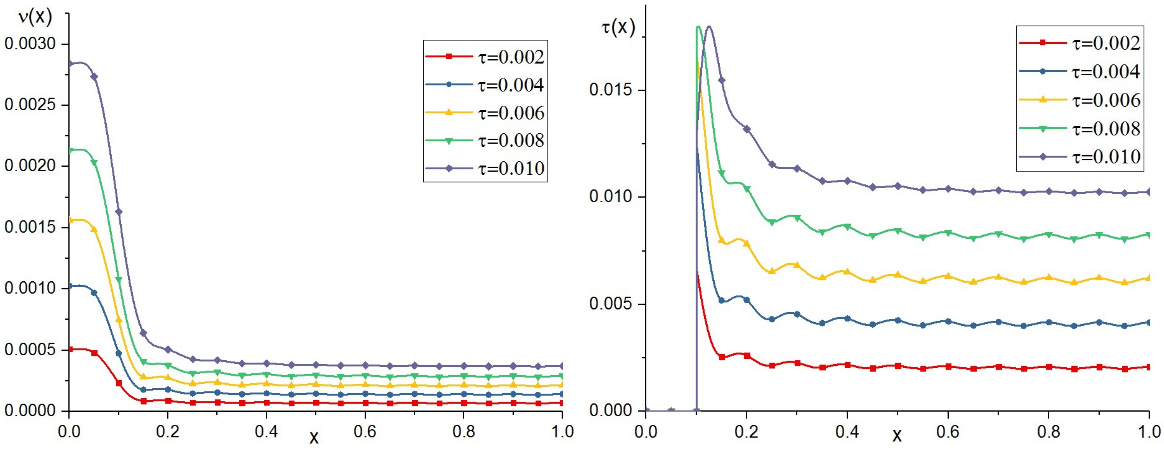

Fig.4.7 Center defect *δ=0.001* a) shear slip field, b) shear traction field.

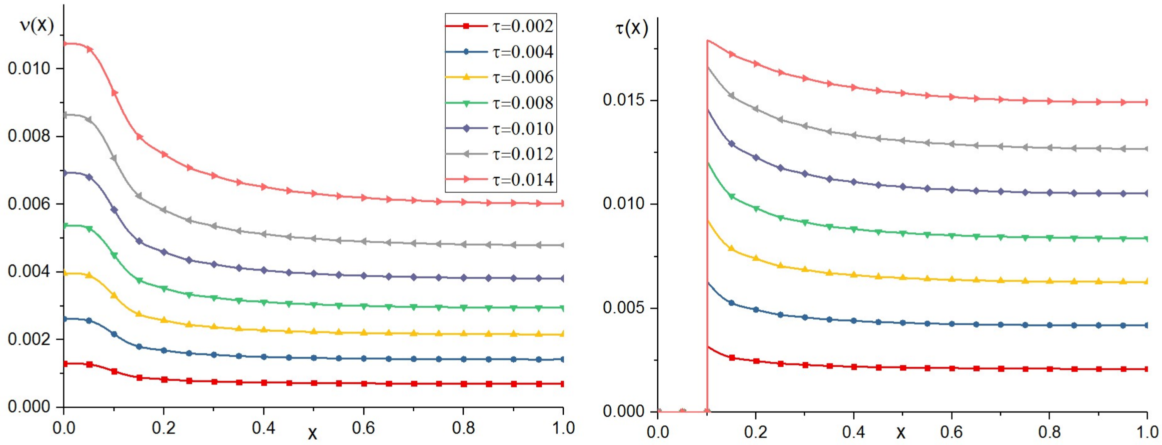

Fig.4.8 Center defect $\delta=0.01$ a) shear slip field, b) shear traction field.

The comparison between the cohesive fracture solution and that of classical fracture mechanics is carried out with parameters consistent with a static crack (i.e., high cohesive surface stiffness and small applied load). The Stress Intensity Factor Handbook [14] gives the SIF for two geometries that are similar to our two-sublayer configuration (i.e., the infinite and semi-infinite plates as shown in Fig.4.9). Note that these two geometries are infinite in extent in the *y*-direction (in our problem the *y* dimension is finite). Due to Saint-Venant’s principle, we anticipate that this will not cause any inconsistency as long as the thickness ($h^+=h^-=h$) of the two-sublayer system is large compared to the crack length.

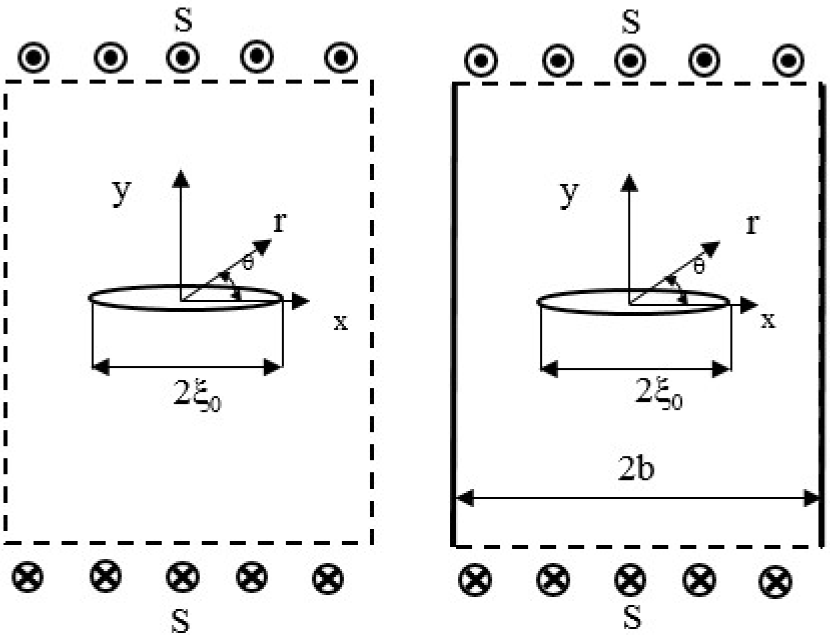

Fig.4.9 a) SIF infinite plate. b) SIF semi-infinite plate.

The SIF's for the two geometries given in SIFs handbook [14] are,

$$\begin{aligned}&\text{Infinite Plate: } \tau(r)=\frac{S\sqrt{\xi_0}}{\sqrt{2r}}\\&\text{Finite Width Plate: } \tau(r)=\frac{\tan^{1/2}\left(\dfrac{\pi\xi_0}{2b}\right)S\sqrt{\dfrac{2b}{\pi}}}{\sqrt{2r}}\end{aligned}\qquad(4.21)$$

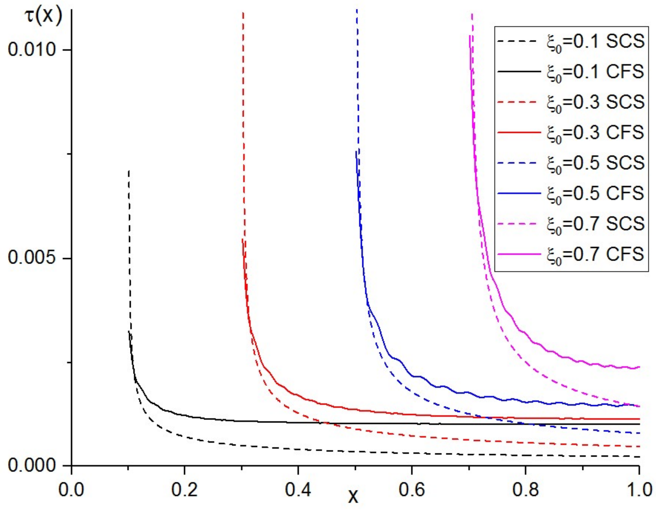

Fig.4.10 Cohesive fracture solution (CFS) vs finite width static crack solution (SCS). $\delta = 0.001$.

Figure.4.10 shows that cohesive fracture solution agrees well with the finite width SCS solutions based on the SIF (4.21_2) around the defect tip. However, SIF gives a poor estimation of fields away from the tip (where the shear traction should converge to the applied shear load rather than approach zero if crack is small).

Edge defect. An edge defect can be modeled by switching the initial intact and defective zones in the center defect geometry as shown in Fig.4.11. The corresponding cohesive strength function can be written as,

$$\tau_{\max}(x) = \begin{cases} 0 & \text{otherwise} \\ \tau_{\mathrm{m}} & -1+\xi_0 \le x \le 1-\xi_0 \end{cases} \tag{4.22}$$

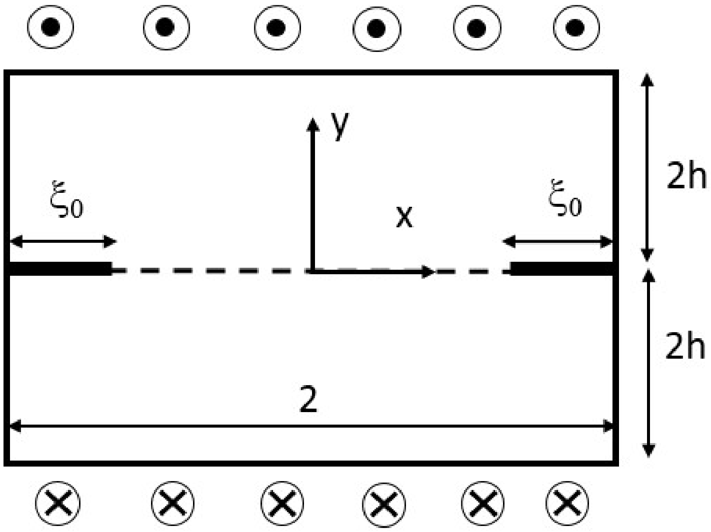

Fig.4.11 two-sublayer system with edge defect.

Here all length quantities are normalized by layer half width (*b=1, h=0.5,* ξ_0*=0.1*), which creates an initial defect region of *0.1* at each edge. The similarities between the center and the edge defects can be explained by an imaginary cut of the center defect geometry (Fig.4.5) along the *y-z* plane which separates the solid into two halves “A” and “B” (as shown left of Fig.4.12). Since both the left and right sides of the halves “A” and “B” are traction free, the two halves can be positioned side by side in a different order which generates the edge defect configuration.

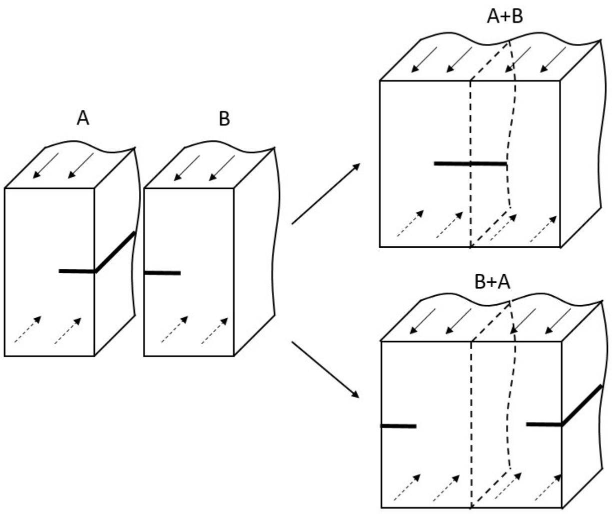

Fig.4.12 Similarities of center and edge defects.

Based on this argument, the edge defect geometry should have exactly the same solution as the center defect region provided the *x*-axis is translated. A computation carried out without taking this idea into account verifies this argument, i.e., Fig.4.13 is the same as Fig.4.7 if the direction of the *x*-axis is flipped. Note that in the SIF handbook, the edge defect geometry was not listed independently since mathematically it is the same as the center defect geometry.

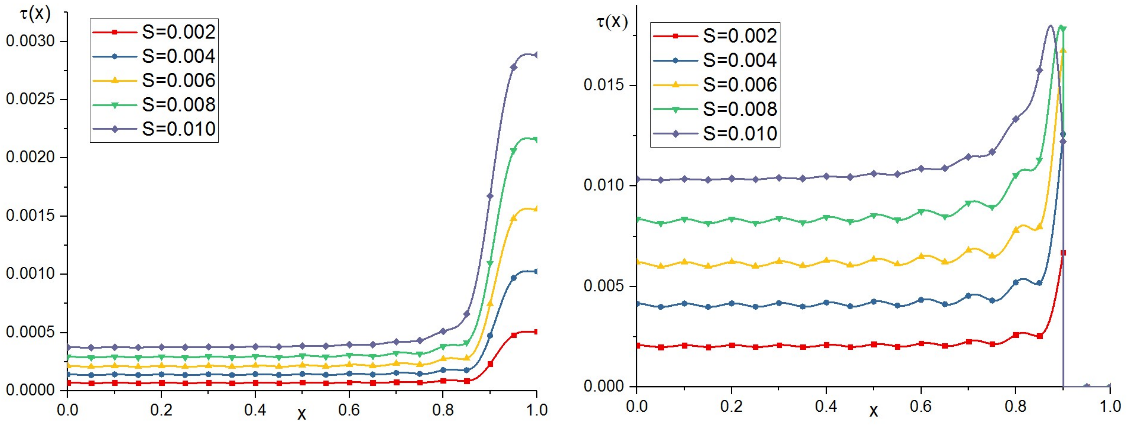

Fig.4.13 The edge defect $\delta=0.001$. a) shear separation field, b) shear traction field.

4.5 Center defect fields in materially nonuniform bilayer

The formulation developed above is not restricted to layered systems that are materially and geometrically uniform. In this subsection the solution is applied to the bilayer problem consisting of an interfacial defect situated between two materially and geometrically nonuniform layers. The specific problem considered is a coating/substrate system in which the coating layer is considerably thinner and stiffer than the substrate layer. Exact SCS for such systems, as well as those consisting of double layers of coating or functionally graded coatings, are treated in [113]. These solutions predict that the SIF increases with decreasing thickness of the coating or, decreasing shear stiffness ratio (μ_c / μ_s) where μ_c is the shear modulus of the coating and μ_s is the shear modulus of the substrate. Because the general mathematical structure of this problem is the same as that of previous problems, many of the features observed are qualitatively the same as well. In order to understand the effect of shear stiffness ratio and thickness ratio (h^+/h^-), where h^+ is the coating thickness and h^- the substrate thickness, the maximum shear traction along the cohesive surface is plotted against the applied shear S. Figure 4.14 reveals how shear stiffness properties and coating thicknesses affect the cohesive surface traction field. Because all the points are computed under the same loading, the maximum traction on the surface can be treated as a parameter characterizing the local stress concentration (similar to SIF). Each locus of points shows that the maximum traction increases with a reduction of coating thickness h^+. A comparison between the three different loci of points shows that as the coating becomes stiffer, the maximum traction is reduced. The computational results presented here indicate behavior that is qualitatively the same as the SCS provided in [113].

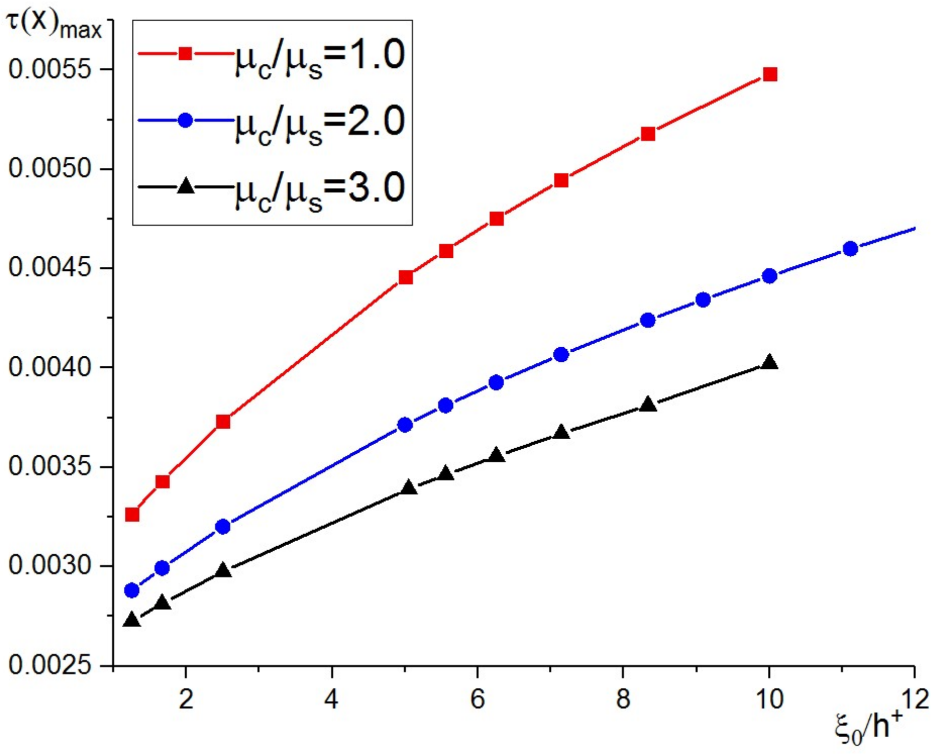

Fig.4.14 cohesive surface maximum shear traction vs defect geometry. Center defect. $\xi_0 = 0.1,\ \delta = 0.001,\ S = 0.001$.

4.6 Linear array of defects and sequence of defect propagation

Modelling initial defects by a coordinate dependent cohesive strength function enables the analysis of more complicated defect configurations. In the previous section on the derivation of the governing integral equations, a perfect symmetry in both geometry and loading is assumed with respect to the *y-z* plane, hence, all the eigenfunctions are even functions of *x* direction which can only be used to approximate fields which are even in *x* as well. Such an assumption restricts the geometry of linear arrays of defects to be even in *x*. Based on the above discussion, the solution to associated static crack analyses of this type of problem include, a) periodic distributions of collinear cracks with equal spacing and size in an infinite domain (Fig.4.15a), and b) three collinear, symmetrically placed cracks (Fig.4.15b). In this subsection, the theory developed above will be applied to predict the response and, to address questions related to multiple defect distributions such as, i) whether or not all defects will propagate prior to complete failure of the cohesive surface, ii) the sequence and rates of defect propagation given that multiple defects propagate, iii) the consistency of the predictions of SCS and CFS.

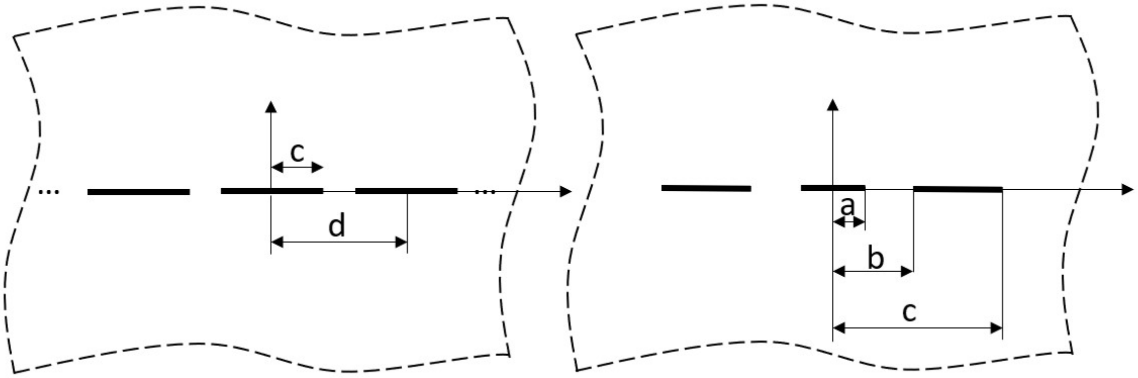

Fig.4.15 Symmetric linear array defect. a) Periodic distribution of defects of equal size and spacing. b) Three symmetrically placed defects with arbitrary size and location.

The SCS for the two different configurations of Fig.4.15 are given below. It is reasonable to assume that Fig.4.15a has a periodic traction distribution which means that all crack tips share the same value of stress intensity factor [14], [104],

$$K_{III} = \lim_{r \to 0} \sqrt{2r}\, S \left\{ 1 - \left[\frac{\sin(\pi c / d)}{\sin(\pi (c+r)/d)} \right]^2 \right\}^{-1/2} \tag{4.23}$$

where *c*, *d* are defined in the figure, and *r* is defined on the horizontal axis from crack tip. For three symmetrically located cracks shown in Fig.4.15b, the corresponding stress intensity factors are given by [14],

$$
\begin{aligned}
K_{IIIa} &= \sqrt{\frac{c^2-a^2}{b^2-a^2}}\,\frac{E(k)}{K(k)}\,S\sqrt{a} \\
K_{IIIb} &= \sqrt{\frac{b^2-a^2}{c^2-b^2}}\left[1-\left(\frac{c^2-a^2}{b^2-a^2}\right)\frac{E(k)}{K(k)}\right]S\sqrt{b} \\
K_{IIIc} &= \sqrt{\frac{c^2-a^2}{c^2-b^2}}\left[1-\frac{E(k)}{K(k)}\right]S\sqrt{c} \\
k^2 &= \frac{c^2-b^2}{c^2-a^2}
\end{aligned}
\tag{4.24}
$$

Note that in (4.24) K_{III} is the mode-III stress intensity factor with the subscript (a, b or c) representing the corresponding crack tip while *k* is a nondimensional parameter characterizing the relative crack lengths. Quantities $K(k)$ and $E(k)$ are complete elliptic integrals of the first and second kind associated with *k*. Because the crack configurations given in Fig.4.15 are for the infinite plane, geometrical parameters must be chosen so that the results obtained can be compared with the finite layered system of the CFS. For periodic defects as shown in Fig.4.15a, it can be proved that when *d=2.0/3.0,* the problem degenerates to the problem of a finite domain with three equally sized and spaced cracks due to symmetry.

Fig.4.16 shows the shear traction for the special case where *d=2.0/3.0*, *c=1.0/6.0*, i.e., where the length of the cracked region equals that of the bonded region.

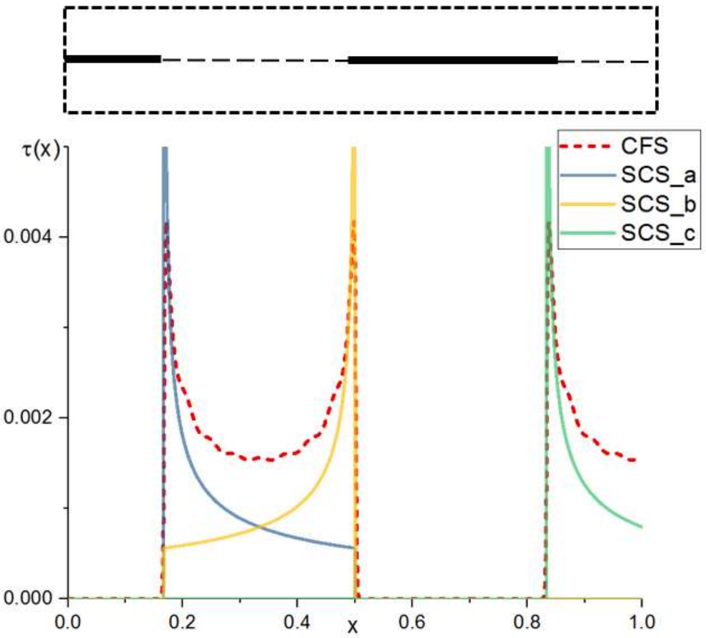

Fig.4.16 Shear traction, periodic distribution of defects.

$d=2.0/3.0$, $c=1.0/6.0$, $\delta=0.001$.

Note that, i) CFS and SCS are consistent near the crack/defect tip, ii) CFS and SCS both predict the same amount of stress concentration regardless of crack location due to the periodic condition, iii) away from the defect tips (into the initially bonded region), the CFS predicts higher stress concentration since it takes defect interaction into consideration automatically whereas SCS not. For more general cases where the location and size of outer cracks varies, the accuracy of SIF is undermined by finite width effect or crack interaction. In the following section, SIF solution is plotted simply for comparison. Fig.4.17 shows the defect spacing's effect on the shear traction field. For closely located defect tips, the interaction between two defect fronts tend to increase the maximum shear traction that leads to defect propagation at an earlier stage (in Fig.4.17a defect tips are at $x=0.05$, 0.1). However, for sparsely located defects, the interaction is negligible (Fig.4.17b).

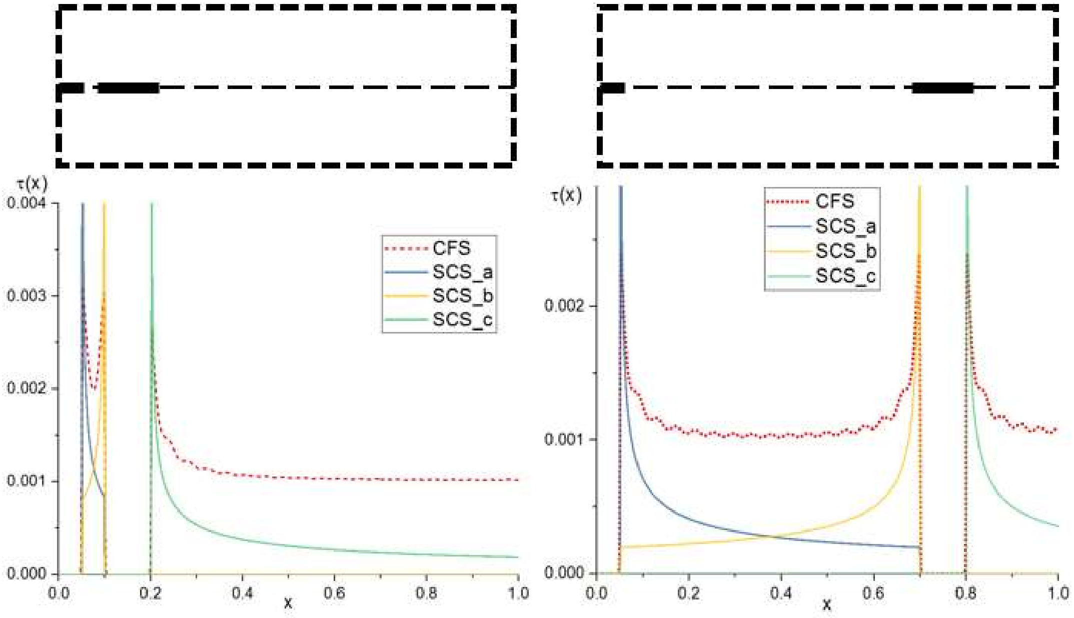

Fig.4.17 Shear traction with same defect size but different spacing.

Three symmetrically placed defects

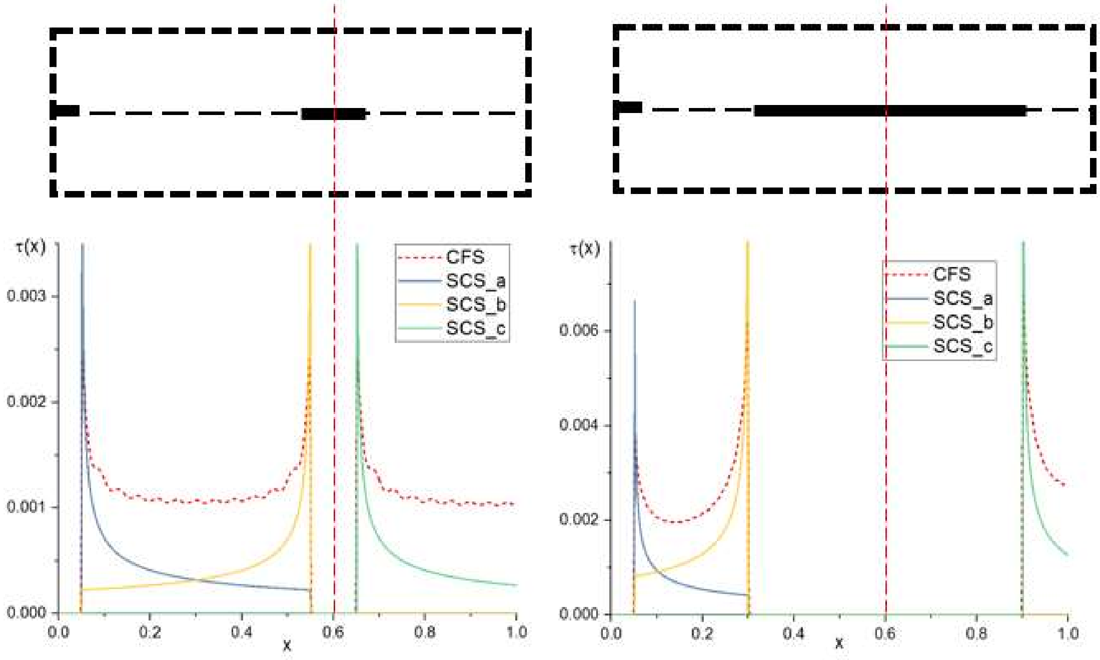

Fig.4.18 Shear traction with same defect center location but different defect size.

Three symmetrically placed defects

Figure.4.18 shows that the crack/defect size has a significant effect on the shear traction distribution. The second and third tips in Fig.4.18b has a significantly higher traction magnitude than its counterpart in Fig.4.18a. Note that in Fig.4.18b the CFS predicts a higher traction magnitude at the third tip (*x=0.9*) than at the second tip (*x=0.3*) whereas the SCS predicts that the second tip has a 3% higher K_{III} than the third tip. Unlike SCS, whose accuracy is largely dependent on a negligible boundary effect, CFS can provide superior results for large crack geometries with a strong boundary condition. This is because CFS exactly accounts for the boundary effect.

4.7 Defect propagation process

The previous subsections are mainly focused on static stress analysis including solution verification based on existing SCS solutions. One of the strengths of CFS is its ability to characterize quasi-static defect propagation. In this subsection, defect propagation processes are analyzed for an exponential force law considering the effects of the different cohesive surface constitutive parameters on the response.

The method of characterizing defect propagation process is the same as previously given in Section 3.4. The fundamental sequence of steps in the quasi-static growth process is as follows. Under small applied loads there is minimal interfacial shear slip $v(x) < \delta$ (or $\tau(x) < \tau_m$ with $\tau(x) = f(v(x), x)$) and the defect is considered static by the onset criterion. As the load is increased a critical slip (or equivalently a critical cohesive surface shear traction) is attained, i.e., $v(x = \xi_0) = \delta$ or equivalently $\tau(x = \xi_0) = \tau_m$[40], [88]. The value of load at which this occurs is the *initiation load*, i.e., that load at which growth initiates. As the load increases beyond this value the defect extends to locations that satisfy the criterion, i.e., $\xi > \xi_0$. This process continues until the cohesive surface becomes unstable, i.e., $d\xi/d\tau \to \infty$ at a finite value of ξ. The critical load at which this occurs is the *bifurcation load* (failure load). Beyond this point the cohesive surface slip increases under decreasing load and there are no stable equilibrium states.

For the fundamental center defect geometry (Fig.4.5), it is reasonable to expect that the cohesive law constitutive parameters e.g., the characteristic force length (δ), will have a strong effect on the defect growth process since it characterizes the brittle or ductile nature of the cohesive surface. Figure 4.19 shows that for a brittle cohesive surface (small δ), cohesive surface deterioration is restricted to a small region near the tip and, the behavior has the appearance of sharp crack growth, i.e., strong stress concentration. As for the ductile cohesive surface that traction pattern is more distributed, the load can be carried by a relatively large area which leads to higher initiation loads and crack initiation at a later stage.

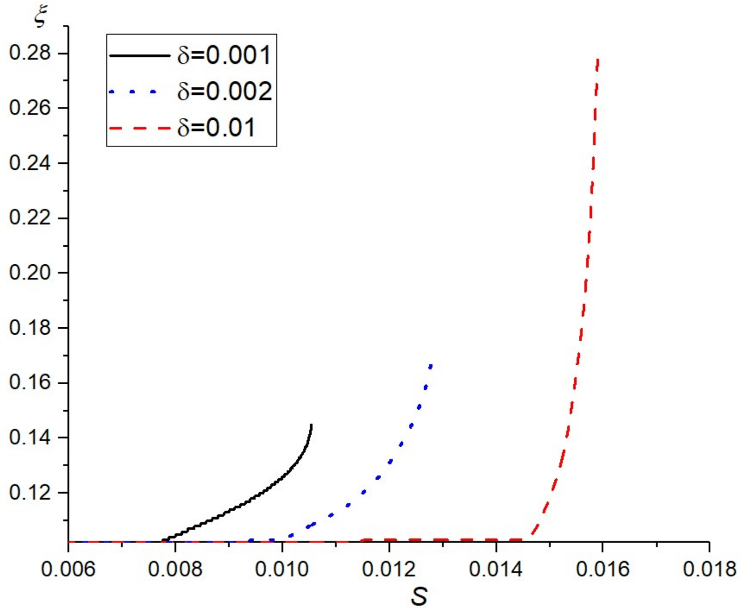

Fig.4.19 Defect propagation of a center defect. Initial defect tip at $\xi_0 = 0.1$.

Figure.4.20a shows that when the sizes of the defects are similar and sparsely distributed, all defect tips have a similar degree of stress concentration which leads to approximately the same maximum traction at different tips and simultaneous defect propagation response. However, when the second defect ($x \in (0.4, 0.8)$) is much longer (Fig.4.20b) than the center defect ($x \in (0, 0.05)$), the first defect tip will not propagate before the cohesive surface becomes unstable. In Fig.4.20c the length of the second defect ($x \in (0.3, 0.9)$) is further increased so that tip c is close to the traction free surface. This configuration is such that boundary effects will occur for defect tip c. The figure indicates that, i) the defect size has a significant effect on defect behavior in that larger defects tend to have a stronger stress concentration which may lead to defect initiation at an earlier stage, ii) comparing the two defect fronts of the outer crack, the defect tip which is closer to the free surface will initiate at an earlier stage and undergoes more substantial defect growth.

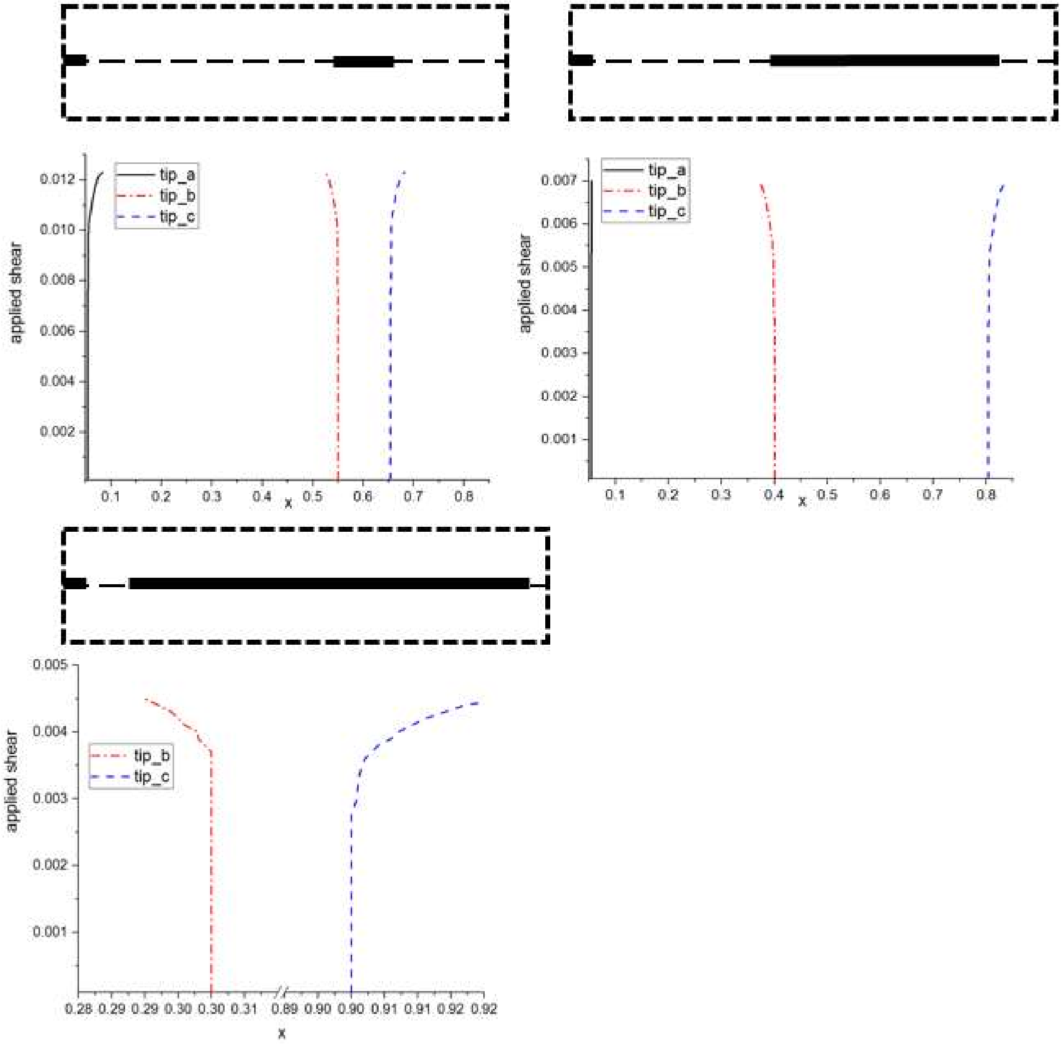

Fig.4.20 Defect propagation. Three symmetrically placed defects.

a) a=0.05, b=0.55, c=0.65. b) a=0.05, b=0.4, c=0.8. c) a=0.05, b=0.3, c=0.9.

4.8 Maximum principal stress and mode-I micro cracks

Micro cracks oriented at certain angles to the primary fracture plane have been observed in anti-plane delamination processes of laminated composites [114], [115]. A careful examination of the stress field at the cohesive surface would help to, i) understand the general fracture initiation process, ii) explain how mode-I micro cracks deviate from the primary fracture plane. Similar to torsion tests, layered composites show an array of 45° oblique tensile micro cracks initiating from the tip of the primary crack [33], [116]. The formulation developed in the previous sections can be used to shed light on mode-I micro crack formation by predicting the maximum principal tensile stresses and their locations in the region of the primary mode-III defect. Because of the assumed form of displacement and slip fields ($u_z(x,y), v(x,y)$), the only two non-vanishing stress components in anti-plane shear loading of layered systems are σ_{xz} and σ_{yz}. For the two non-vanishing stress components, σ_{yz} is nothing but the interfacial shear traction which is a primary output field from the computation program. However, the other stress component σ_{xz} has to be obtained from post processing. Note that from section 4.1, the elastic field for each sub-layer is governed by two sets of multipliers (C_n, D_n in (4.8)). However, the program calculated multipliers governing interfacial slip are basically the combinations of C_n and D_n from two sub-layers. Generally it's impossible to derive C_n and D_n directly from v_n. However, since the problem in this section has perfect symmetry in the thickness direction, one can expect that the two sublayers are subject to exactly the same deformation along the cohesive surface. Hence, it is reasonable to distribute the mode multipliers governing interfacial slip evenly to two sublayers. Stress tensor manipulation yields the maximum tensile stress and its corresponding direction as,

$$\sigma_p = \sqrt{\sigma_{xz}^2 + \sigma_{yz}^2} \qquad \vec{\lambda}_p = \begin{bmatrix} \dfrac{\sigma_{xz}}{\sqrt{2}\sigma_p} & \dfrac{\sigma_{yz}}{\sqrt{2}\sigma_p} & \dfrac{1}{\sqrt{2}} \end{bmatrix} \tag{4.25}$$

The oblique mode-I micro crack plane (oriented at an angle φ in Fig.4.21) is perpendicular

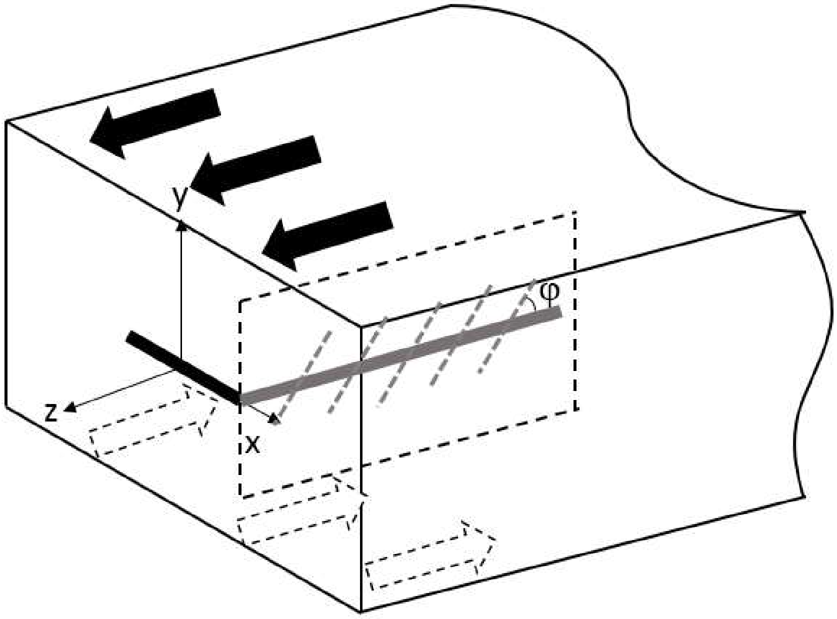

Fig.4.21 Orientation of oblique mode-I micro cracks.

to the principal tensile stress direction given in (4.25). The mode-I micro crack planes' intersection lines with the local *y-z* plane at the primary defect front is shown in Fig.4.21.

Figure.4.22 shows the values of orientation angle φ for a center defect ($h = 0.5,\ \xi_0 = 0.1$) geometry under an moderate applied loading prior to defect initiation. It begins with $\varphi = 90^o$ since the dominant stress component in the defect region is σ_{xz}. Far ahead of the crack tip the unperturbed shear converges to the uniform shear loading and the σ_{xz} component vanishes so that $\varphi = 45^o$. Within the region close to the crack tip, a smooth transition from 90° to 45° occurs with the variation depending on the relative magnitude of σ_{xz} and σ_{yz}. The prediction of mode-I micro crack initiation can proceed once a crack initiation criterion has been specified. Difficulties with this approach are that the exact values of the stress components close to the defect tip is sensitive to both the form of cohesive law and the manner in which the cracked region is characterized.

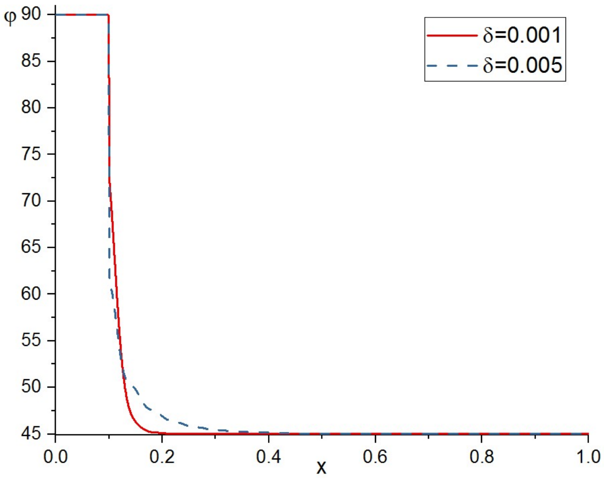

Fig.4.22 Distribution of orientation angle φ.

4.9 Characterization of frictional cohesive surface and corresponding response

Based on the same frictional cohesive constitutive relation shown in section 3.6, this section presents the analogous bifurcation plots for two qualitatively different kinds of layered system

For the decohesion dominated case (Fig.4.23a), the general shape is similar to previous frictionless cases (Fig.4.6) except that the unstable branch will not decrease to zero applied shear since the shear traction would attain the persistent maximum friction force regardless of the large value of shear slip.

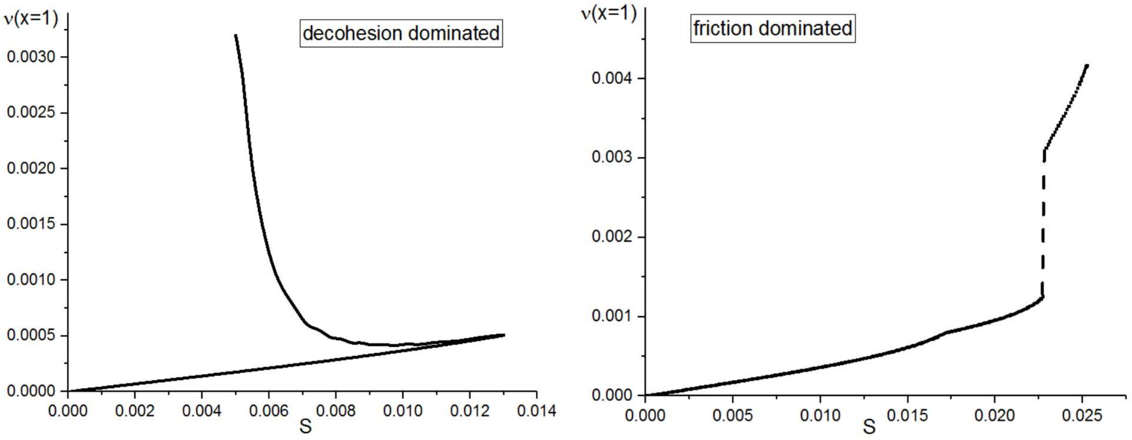

Fig.4.23 Bifurcation plots (center defect) a. Decohesion dominated. b. Friction dominated.

For the friction dominated case (Fig.4.23b) the behavior appears to be qualitatively different from decohesion dominated response in the following sense, i) there does not appear to be a tangent bifurcation at a critical failure load. The cohesive surface will still fail as it appears that the slope of the curve becomes unbounded at a finite value of shear load. ii) a shear slip jump is observed before the bifurcation shear load (in other words, a discontinuity of shear slip under a continuously increasing applied shear). Note that this phenomenon is not observed in related research on torqued cylinders (Song and Levy 2019) due to the differences in the applied traction field (uniform versus linearly varying with radial coordinate). The exact behavior beyond the last computed points of Fig.4.23b is unknown since i) the curve is almost vertical leading to a breakdown of the Newton Raphson process and ii) the slip magnitude may be large, thereby violating the infinitesimal strain assumption.

5 Instability and Cohesive Fracture of the General N-Sublayer System

5.1 Interfacial integral equations

The formulation for the *N*-sublayer system (Fig.5.1) is obtained by following a similar process as the two-sublayer system. The major difference is that the N-sublayer system has two outer layers with prescribed tractions and at least one layer that is subject only to reactive cohesive surface tractions on its upper and lower surfaces. To avoid ambiguity, a new labeling scheme for the multilayer system is introduced: i) superscripts represent the numbering of layers from top to bottom (e.g., h^1 means the half thickness of the 1^{st} layer), ii) subscripts define the location within one layer, *1* for top surface and *2* for bottom (e.g., f_2^1 represents the shear traction on the bottom surface of the 1^{st} layer), iii) because the cohesive surface shear slip is defined for two adjacent layers, two superscripts are assigned ($v^{2,3}$ means the cohesive surface shear slip between the 2nd and 3rd sublayers).

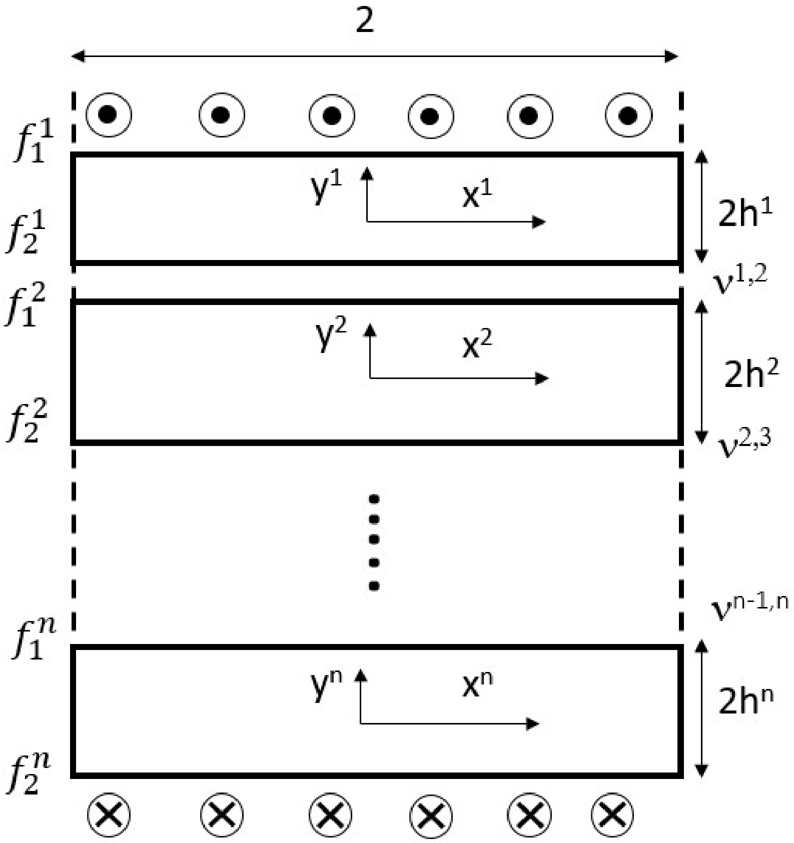

Fig.5.1 N-sublayer system.

Now suppose the system has *M+1* sublayers with *M* cohesive surfaces where each cohesive surface slip field is characterized by an expansion in *N+1* modes (*n*=0, 1, 2, …, *N*), i.e.,

$$v^{m,m+1}(x) = \sum_{n=0}^{N} v_n^{m,m+1} \cos(\beta_n x) \tag{5.1}$$

Thus, there are $M \bullet (N+1)$ unknown mode multipliers which, together with the *M* unknown relative rigid body displacements[11], result in a total of $M \bullet (N+2)$ unknowns to be solved for. The nonlinear system of integral equations governing these unknowns is given by,

---

[11] One sublayer is fixed against rigid body displacement.

$$
\begin{aligned}
&0 = \nu_0^{m,m+1} - \nu_R^{m,m+1} + (h^m + h^{m+1})\int_{-1}^{1} \frac{f_1^m(\nu^{m,m+1}(x),x)}{2}dx \\
&0 = \nu_n^{m,m+1} + \frac{\int_{-1}^{1} f_1^m(x)\cos(\beta_n x)dx}{2\beta_n}\left[\tanh(\beta_n h^m) - \coth(\beta_n h^m)\right] + \frac{\int_{-1}^{1} f_2^{m+1}(x)\cos(\beta_n x)dx}{2\beta_n}\left[\tanh(\beta_n h^{m+1}) - \coth(\beta_n h^{m+1})\right] \\
&\qquad + \frac{\int_{-1}^{1} f_2^m(x)\cos(\beta_n x)dx}{2\beta_n}\left[\tanh(\beta_n h^m) + \coth(\beta_n h^m)\right] + \frac{\int_{-1}^{1} f_1^{m+1}(x)\cos(\beta_n x)dx}{2\beta_n}\left[\tanh(\beta_n h^{m+1}) + \coth(\beta_n h^{m+1})\right] \\
&0 = \int_{-1}^{1} f_2^m(\nu_0^{m,m+1}, \nu_1^{m,m+1}, \nu_2^{m,m+1}, \ldots, \nu_N^{m,m+1}, x)dx - \int_{-1}^{1} f_1^1(x)dx \\
&m = 1,2,\ldots M \\
&n = 1,2,\ldots N
\end{aligned}
\tag{5.2}
$$

Equation (5.2_2) provides $M \bullet N$ equations and ($5.2_{1,3}$) each provides M equations for a total of $M \bullet (N+2)$ equations.

5.2 Instability and asymmetric deformation in the multi-sublayer system

5.2.1 Instability and asymmetric deformation of uniform tri-sublayer system

Recall that the bifurcation analysis of the uniform cohesive surface problem in Section 4.3 concludes that the uniform cohesive surface should have a uniform shear traction (and slip) distribution, equal to the applied shear traction (interfacial slip can then be obtained by inverting the cohesive force law). Inverting the exponential force law yields a Lambert W function which is not single-valued. Generally, there are two slip values to one applied shear which can be verified by checking a plot of the force law. In the figure of a force law (e.g. Fig.2.10), a certain loading can be represented by a horizontal line. For an applied shear smaller than the cohesive strength, there are two intersection between the line representing applied load and force law (representing two solutions). This fact should not cause any ambiguity in the two-sublayer system since there is only one cohesive surface. However, for a system with more than one cohesive surface, the multi-valued behavior leads to complicated bifurcation patterns such as asymmetric deformed configurations arising from symmetric geometry and loading. In this subsection, the analysis of the tri-sublayer system and the four-sublayer system are discussed in detail.

A result of the uniqueness theorem is that a uniform cohesive surface will have a uniform shear slip and traction field. The slip fields for a tri-sublayer system (with two cohesive surfaces) can be written as,

$$\begin{aligned} v^{1,2}(x) &= v^{1,2} \\ v^{2,3}(x) &= v^{2,3} \end{aligned} \tag{5.3}$$

where $v^{1,2}, v^{2,3}$ are constant. Global equilibrium requires that,

$$\begin{aligned} S - \tau_{\max 1}\sqrt{e}(v^{1,2}/\delta)e^{-0.5(v^{1,2}/\delta)^2} &= 0 \\ S - \tau_{\max 2}\sqrt{e}(v^{2,3}/\delta)e^{-0.5(v^{2,3}/\delta)^2} &= 0 \end{aligned} \tag{5.4}$$

For a given shear traction load (*S*), the exact solution for the interfacial slip can be directly obtained by isolating expressions for $v^{1,2}$ and $v^{2,3}$. From (5.4),

$$\begin{aligned} v^{1,2} &= \delta \Bigg/ \sqrt{-\frac{1}{LambertW\left(-\dfrac{e^{-1}S^2}{\tau_{\max 1}^2}\right)}} \\ v^{2,3} &= \delta \Bigg/ \sqrt{-\frac{1}{LambertW\left(-\dfrac{e^{-1}S^2}{\tau_{\max 2}^2}\right)}} \end{aligned} \tag{5.5}$$

Consider a displacement-controlled system, assume the top sublayer and bottom sublayer are subjected to equal but opposite rigid body displacements (top moving in positive *z* direction). Based on (5.2$_1$), the shear slip field can be written as,

$$\begin{aligned} v^{1,2} &= R_{t,b} - R_{mid} - S\left(h_1 + h_2\right) \\ v^{2,3} &= R_{t,b} + R_{mid} - S\left(h_2 + h_3\right) \end{aligned} \tag{5.6}$$

where $R_{t,b}$ is the absolute value of the controlled rigid body translation (R.B.T) of top and bottom sublayers, R_{mid} is the value of R.B.T of the middle sublayer. Rearranging terms $R_{t,b}$ and R_{mid} can be written as,

$$\begin{aligned} R_{t,b} &= \frac{1}{2}\left[\nu^{1,2} + \nu^{2,3} + S\left(h_1 + 2h_2 + h_3\right)\right] \\ R_{mid} &= \frac{1}{2}\left[-\nu^{1,2} + \nu^{2,3} + S\left(h_3 - h_1\right)\right] \end{aligned} \tag{5.7}$$

Now take S as the forcing term of the problem. The values of $R_{t,b}$ and R_{mid} for a given loading (S) can be obtained by substituting (5.5) into (5.7). Due to the multi-valued nature of the Lambert W function (a stable and an unstable branch), different combinations of such branches will generally create four configurations based on permutations and combinations.

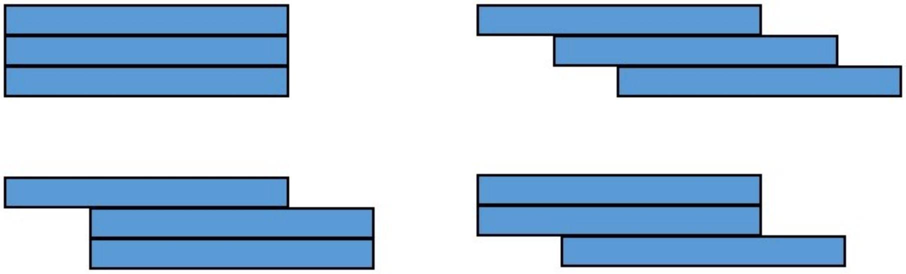

Fig.5.2 Four terminal configurations of traction control loading.

Suppose a tri-sublayer system subject to traction loading that follows exactly as the force law (load to critical shear and then unload), Fig.5.2 shows four "possible" terminal configurations. The top left case indicates that two cohesive surfaces heal resulting in their initial state since the force law (XN) used here is reversible. The top right figure is the opposite of the first case in that both cohesive surfaces snap (the slip value jumps to the unstable branch of the force law) to large slip values which leads to a skew symmetric configuration. Note that the two cases at the top of Fig.5.2 both have symmetry since the two cohesive surfaces are behaving exactly the same (in the unloading process, two cohesive surfaces fall into the same branch of the cohesive force law). The bottom of Fig.5.2 shows two asymmetric terminal configurations caused by different cohesive surface behavior governed by different branches of the cohesive force law (one cohesive surface goes back to the stable branch of the force law and heals itself, the other cohesive surface snaps as the unstable branch governs). Note that for the displacement-controlled system, the first case in Fig.5.2 cannot be obtained since the controlled displacement will create offsetting between the top and bottom sublayer. The other three cases are distinguished by the relative magnitudes of two cohesive surface slip values. For a displacement-controlled system (top and bottom sublayers subject to equal and opposite controlled displacement), the two cohesive surface slip values are closely related to the location of the middle sublayer. The skew symmetric configuration can be obtained only when the middle sublayer does not displace, while the other two asymmetric cases can be differentiated by checking the direction of R.B.T of the middle sublayer. For the convenience of discussion about system configuration based on sublayer R.B.T. R_{mid} vs $R_{t,b}$ is plotted for the tri-sublayer system under displacement-controlled loading. To distinguish from the bifurcation plots of previous sections, "configuration bifurcation plot" is used in this chapter for R_{mid} vs $R_{t,b}$ plots.

Uniform material, geometry and cohesive strength. For cases where the two uniform cohesive surfaces have identical cohesive strengths, the direction of movement of the middle sublayer is random which manifested by two branches in configuration bifurcation plot of Fig.5.3. In this figure curves show a perfect symmetry with respect to the abscissa. The general process as depicted in Fig.5.3 proceeds as follows. For ductile cohesive surface (large δ), under a monotonically increasing displacement control of top and bottom sublayers, the middle sublayer initially undergoes no rigid body translation and the system remains symmetric (①). At a certain value of the controlled displacement, the symmetric configuration is broken, and the middle sublayer will displace together with the either top or bottom sublayer (②or ③, corresponding to the two bottom cases in Fig.5.2). For brittle cohesive surface (small δ), the asymmetric configuration is formed by an abrupt jump or snap bifurcation from the symmetric configuration as opposed to the gradual process of the ductile cohesive surface. There is another branch ④ (top right case in Fig.5.2) which indicates a symmetric configuration after the bifurcation point. However, this branch is unstable and ultimately unobservable since any material imperfection or nonuniformity would break the configuration of perfect symmetry leading to asymmetric configurations.

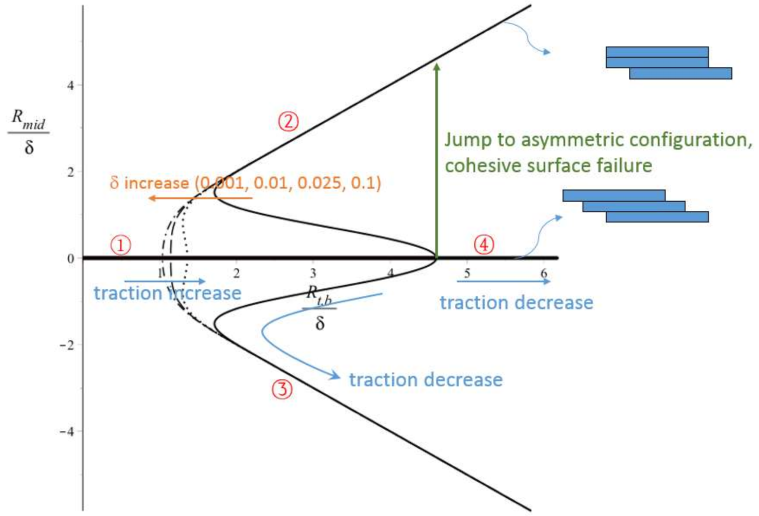

Fig.5.3 Configuration bifurcation plot for uniform cohesive surface.

Uniform material, geometry and cohesive surface with different cohesive strength. In the preceding subsection, the symmetric bifurcation behavior (Fig.5.3) was considered for the tri-sublayer system with perfect symmetry (identical sublayer geometries and cohesive strengths). However, once the perfect symmetry in geometry or material properties is removed, some of the bifurcation branches become unreachable and the stable (i.e., observable) configuration of the system can be determined. In this subsection, parameters and sublayer geometries are kept the same with the exception of one of the cohesive surface strengths (τ_m) which is taken to be slightly weaker than the others are. Figure.5.4a shows that the 4 branches of configuration bifurcation plots no longer intersect at a single point as the previous uniform cohesive surface case. The symmetry is broken, and the curves appears as two separated groups. The first one is composed of ①, ② which shows that the middle layer displaces on initial application of the load and tends to move in the same direction as the top layer before bifurcation occurs. Note that ① is the branch that begins at the origin (initial configuration). The other group (③, ④) are unstable branches lying entirely in the 4th quadrant and have no physical significance since they never intersect with any curve starting from the initial configuration (origin). This means that these equilibrium states can't be obtained by a continuous increase in loading of the system from the symmetric unstressed initial configuration. For purpose of distinction, the applicable configurations are drawn in blue close to the corresponding curves, whereas the inapplicable ones are drawn in red as shown in Fig.5.4. It is worth noting that the bigger the perturbation in cohesive strength, the more the two groups will diverge. As the perturbation in cohesive strength vanishes, the plots converge to the symmetric unperturbed solution (Fig.5.3). Comparing Fig.5.4 with the corresponding unperturbed case of Fig.5.3 shows that the perturbation of cohesive strength will not fundamentally affect the response, which is determined by the ductility of the cohesive surface, i.e., either an abrupt jump (brittle) or a smooth continuous transition (ductile) to an asymmetric configuration. However, the perturbation of cohesive strength does control the direction of R.B.T of the middle sublayer (only one configuration from the bottom of Fig.5.2 is applicable), whereas in the case of unperturbed case, either one is equally likely.

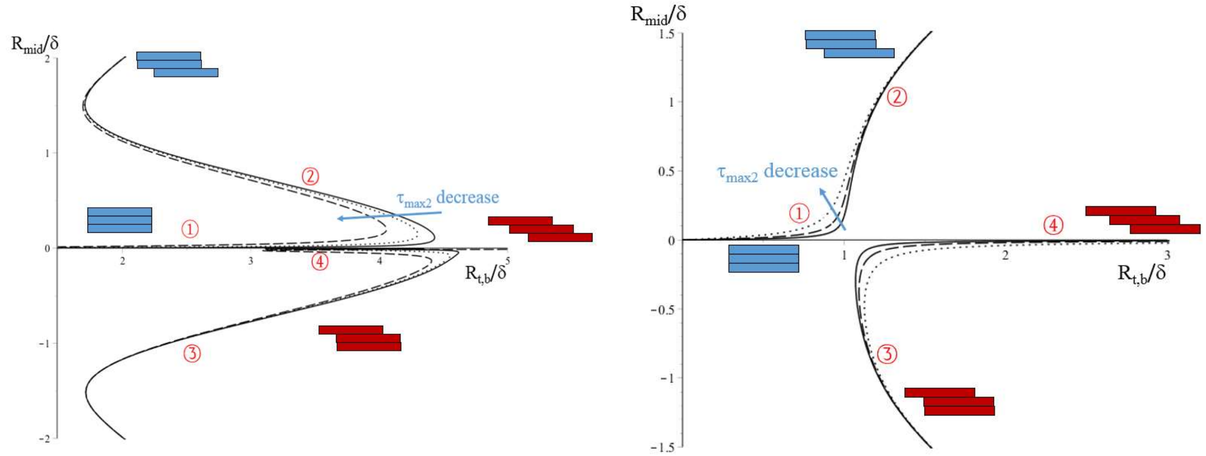

Fig.5.4 Configuration bifurcation plot for uniform cohesive surfaces with perturbed strength. a) brittle cohesive surface. b) ductile cohesive surface

For the case of a perturbed brittle cohesive surface under increasing displacement-controlled loading, the system initially moves through a sequence of quasi-skew symmetric configurations (negligible R.B.T of the middle layer). As the controlled displacement becomes larger, the interfacial shear increases and the R.B.T of the middle layer becomes noticeable with its direction of movement following the other constituent with the stronger cohesive surface. Once the interfacial shear reaches the critical load, the weaker cohesive surface snaps and the shear traction jumps back to a small value. To compensate the abrupt decrease of shear traction, the stronger cohesive surface goes back along the stable branch of force law and self-heals, its slip decreases, and the asymmetric configuration is obtained. The response of perturbed ductile cohesive surface model is similar except the displacement jump is replaced by a gradual process.

5.2.2 Instability and asymmetric deformation of uniform four-sublayer system

The analysis of a four-sublayer system follows the same procedure as mentioned above. For convenience of discussion, a new labeling system is introduced. From top to bottom, the sublayers are labelled from 1 to 4. Assume that the first and fourth sublayer undergo equal but opposite controlled R.B.T. For a uniform four-sublayer system with three cohesive surfaces, the expressions for cohesive surface slip are,

$$\begin{aligned} v^{1,2} &= R_1 - R_2 - S\left(h_1 + h_2\right) \\ v^{2,3} &= R_2 - R_3 - S\left(h_2 + h_3\right) \\ v^{3,4} &= R_3 + R_1 - S\left(h_3 + h_4\right) \end{aligned} \tag{5.8}$$

For each applied load *S,* the cohesive surface slip values for three uniform cohesive surfaces can be obtained by inverting the force law. Equation (5.8) is a system of three linear equations governing three R.B.T (R_1, R_2 and R_3). The bifurcation behavior and configuration of a displacement control system can be obtained by plotting R_2 and R_3 versus the controlled displacement R_1.

Figure	τ_{max1}	τ_{max2}	τ_{max3}
5.5a	0.018	0.018	0.018
5.5b	0.016	0.016	0.018
5.5c	0.016	0.018	0.018

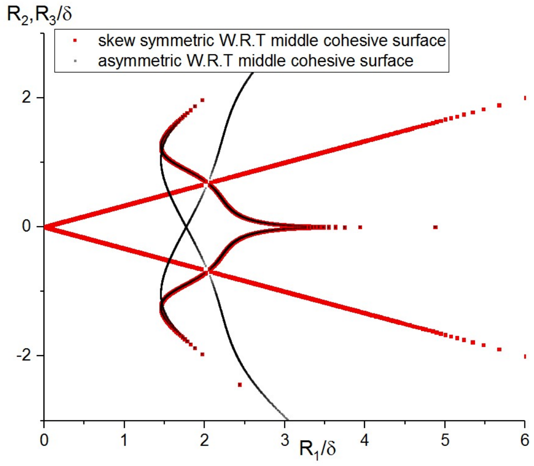

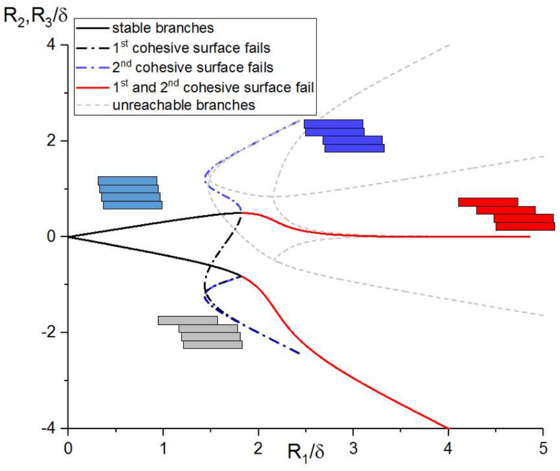

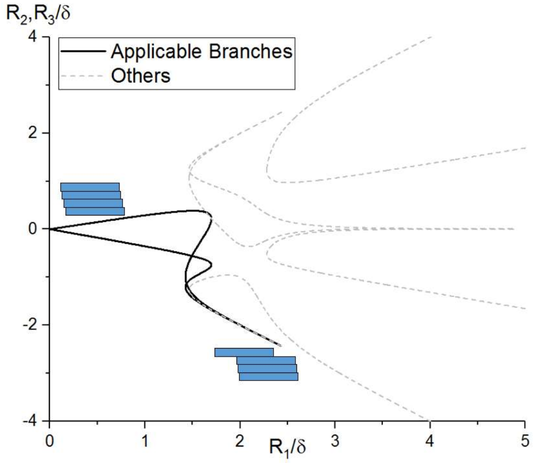

Fig.5.5 Configuration bifurcation plot of four-sublayer brittle uniform cohesive surface ($\delta = 0.001$). a) same cohesive surface strength, b) two weak cohesive surfaces, c) one weak cohesive surface

Figure.5.5 shows the transition in behavior from an idealized system with three cohesive surfaces of identical strength (Fig.5.5a) to the more realistic case in which one of the cohesive surface is weaker or stronger than the other two (Fig.5.5b,c). Figure.5.5a shows that for the system without any perturbation, all the branches (8 of them) intersects at two bifurcation points. Whether the system remains skew symmetric or develops into an asymmetric configuration after hitting the bifurcation point is mathematically arbitrary and would ultimately depend on imperfections in the system. Figure.5.5b relaxes the condition of identical cohesive surfaces by choosing two to be weaker than the third. The imperfection introduces two candidates of cohesive surface failure that reduce the number of applicable branches from 8 to 4 (1 stable branch and 3 unstable ones) since the stronger cohesive surface should never fail before the weaker ones do. Figure.5.5c shows that if there is only one weak cohesive surface, i.e., the only candidate for cohesive surface failure, 8 branches degenerate to only two applicable branches (one stable and one unstable which means the configuration can be determined) such that the weakest cohesive surface snaps and the two others self-heal (the cohesive surface slip closes). Initially, the four-sublayer system would deform symmetrically like a deck of card under relatively small controlled displacement. As the controlled displacement increases, interfacial slips increase such that the traction on the weaker cohesive surface reaches the cohesive strength which signals bifurcation. After that the second sublayer would jump back and move together with the third and fourth layers such that the cohesive surface slips of the second and third cohesive surfaces close.

It might be argued that the asymmetric bifurcation configuration results from the reversable cohesive force law, however the argument is only partially correct. The self-healing process occurs because the force law has more than one equilibiurm state for a given load. As long as the basic structure of force law (stable branch following by unstable branch) remains unchanged, under monotonically increasing controlled displacement, there will always be an asymmetric configuration which can only be obtained by undergoing a cohesive surface self-healing process.

5.2.3 Instability and asymmetric deformation of the nonuniform tri-sublayer system

Rigid body translation in systems with nonuniform cohesive surfaces are not as important as systems with uniform cohesive surfaces since the main focus of nonuniform cohesive surface analysis is traction related to defects. This subsection presents a brief discussion of the instability in the tri-sublayer system with defect geometry consisting of one center defect on each cohesive surface. The analysis of the nonuniform cohesive surface problem and its resulting behavior follows along the lines of the uniform case above. However, the solution for the rigid body translation for a nonuniform cohesive surface problem cannot be as easily found as in the uniform one. Recall that for the uniform cohesive surface problem simply inverting the force law is all that is required. For the nonuniform cohesive surface problem, the cohesive surface slip field of the whole traction controlled process has to be calculated. This consists of both a stable branch (from a monotonically increasing load to the critical point, initiation and stable defect grwoth) and an unstable branch (unload to vanishing traction, unstable defect growth resulting in cohesive surface failure). Recall the slip field at the nonuniform cohesive surface,

$$
\begin{aligned}
v^{1,2}(x) &= D_0^{1,2} + C_0^{1,2}h + \sum_{n=1}^{\infty}\left[C_n^{1,2}\cos(\beta_n x)\sinh(\beta_n h) + D_n^{1,2}\cos(\beta_n x)\cosh(\beta_n h)\right] \\
v^{2,3}(x) &= D_0^{2,3} + C_0^{2,3}h + \sum_{n=1}^{\infty}\left[C_n^{2,3}\cos(\beta_n x)\sinh(\beta_n h) + D_n^{2,3}\cos(\beta_n x)\cosh(\beta_n h)\right]
\end{aligned} \tag{5.9}
$$

in which D_0 is the term in the displacement expansion that characterizes the relative rigid body translation of two adjacent sublayers. The $C_0 y$ term represents a simple shear deformation in the *y* direction while the higher order trigonometric terms characterize a nonuniform shear distribution in the *x* direction due to the presence of defects. However, there are two clarifications that need to be examined, i) the elasticity solution will not eliminate the arbitrary R.B.T of the system as a whole which means one of the layers must be fixed against rigid body translation, ii) the constants D_0's are relative R.B.T of two adjacent sublayers, and an algorithm needs to be introduced in order to compute the R.B.T of each sublayer. Recall

$$
\begin{aligned}
D_0^{1,2} &= R_1 - R_2 \\
D_0^{2,3} &= R_2 - R_3
\end{aligned} \tag{5.10}
$$

where R_1 is the R.B.T of the top sublayer, R_2 is the R.B.T of the middle sublayer and R_3 is the R.B.T of the bottom sublayer. Suppose the top and bottom sublayers translate same amount in opposite direction ($R_1 = -R_3 = R_{t,b}$, $R_2 = R_{mid}$), which is also the controlled displacements. The initial position of middle sublayer is chosen to be the reference, equation (5.10) can be rewritten as

$$
\begin{aligned}
R_{t,b} &= (D_0^{1,2} + D_0^{2,3})/2 \\
R_{mid} &= (-D_0^{1,2} + D_0^{2,3})/2
\end{aligned} \tag{5.11}
$$

The original load-controlled system now has been transformed into an equivalent displacement-controlled system. The sublayer configurations can be obtained once R_{mid} vs $R_{t,b}$ is plotted. It can be expected that similar to the uniform cohesive surface problem (Fig.5.3), there is an unstable (unreachable branch for the classical pitchfork bifurcation) skew symmetric configuration when no perturbation of cohesive strength exists. In that case, the second sublayer does not move while the top and bottom sublayers rigidly translate by equal amounts in opposite directions (resulting in a horizontal line as shown in Fig.5.3). When a slight perturbation (a perturbation of cohesive strength or a microstructural defect or a geometrical defect) appears, the perfect symmetry in the thickness direction is broken, the system will end up with an asymmetric configuration. To trigger an asymmetric configuration, the 2nd cohesive surface is set to be slightly weaker than the 1st one. Based on the results from the uniform cohesive surface problem, one would expect that, after reaching the critical load, the middle layer tends to move along with the top layer (with whom it forms a stronger attachment). Figure.5.6 shows the configuration bifurcation plots of thin sublayer system with different magnitudes of cohesive strength perturbation (the 1st cohesive surface with a cohesive strength $\tau_m^{1,2} = 0.018$ is the unperturbed value, the 2nd cohesive surface strength is perturbed to be slightly smaller). Under displacement-controlled loading, the configuration bifurcation plot reveals a stable quasi symmetric branch (close *to the abscissa*), followed by two displacement jumps. Ultimately, at a later stage of unstable branch, the middle sublayer will move with the top sublayer such that the second interfacial slip snaps and the first interfacial slip is closed. Those two different slips under the same relatively small loading correspond to the two shear slip values under the same small applied shear traction in the force law.

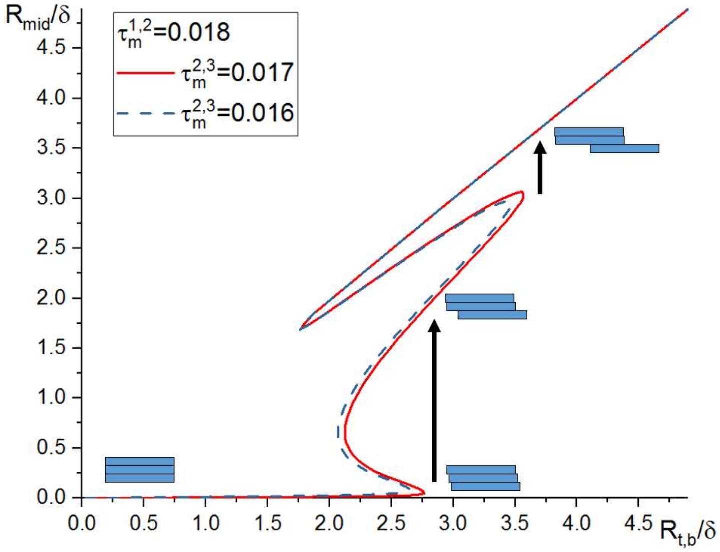

Fig.5.6 Brittle thin layer ($\delta = 0.001$, $h = 0.1$) with different cohesive strength perturbation.

Figure.5.7 shows how bifurcation plots vary with sublayer thickness (note all sublayers are equally thick). Based on the stages of configuration bifurcation, three branches are defined. Start from the origin, the branch that essentially overlaps the abscissa is the skew *symmetric configuration* branch since the R.B.T of the middle sublayer is almost zero regardless of increasing controlled displacement. The straight line with a slope of approximately *1* is the *asymmetric configuration* branch since the middle layer is moving together with the top sublayer, creating a large difference in shear slip between the two cohesive surfaces. The curve connecting the symmetric and asymmetric branches is called the *transition* branch which is the most complicated one. However, the transition branch only affects the transition process without affecting the ultimate configuration. Compare the configuration bifurcation plot of the center defect geometry shown in Fig.5.7 with the uniform cohesive surface plots shown in Fig.5.3. It is apparent that regardless of the introduction of a cohesive surface defect, the symmetric and asymmetric branches, as well as the overall physical behavior, are very similar (barring minor differences in the transition branch). These differences in the transition branch include, i) for the uniform cohesive surface, an almost straight line connecting the symmetric and asymmetric branches (the transition branch of the nonuniform cohesive surface geometry has a wiggle), ii) a sharpness to the wiggle that increases with decreasing layer thickness and, which may cause a second displacement jump ($h=0.1$ case in Fig.5.7). However, for the ductile cohesive surface case, the behavior of the thin layer case ($h=0.1$) is similar to its counterpart in the uniform cohesive surface case (Fig.5.3). The middle sublayer starts to diverge smoothly and notably away from the abscissa when the applied R.B.T is close to δ. However, as the thickness increases, the distinctive displacement jump behavior in previous brittle cases start to show up in the nonuniform ductile case. This transition, for increasing layer thickness (equivalent to decreasing characteristic force length in the uniform cohesive surface case shown in Fig.5.3), from smooth to abrupt asymmetric configurations is also observed in the uniform case as well.

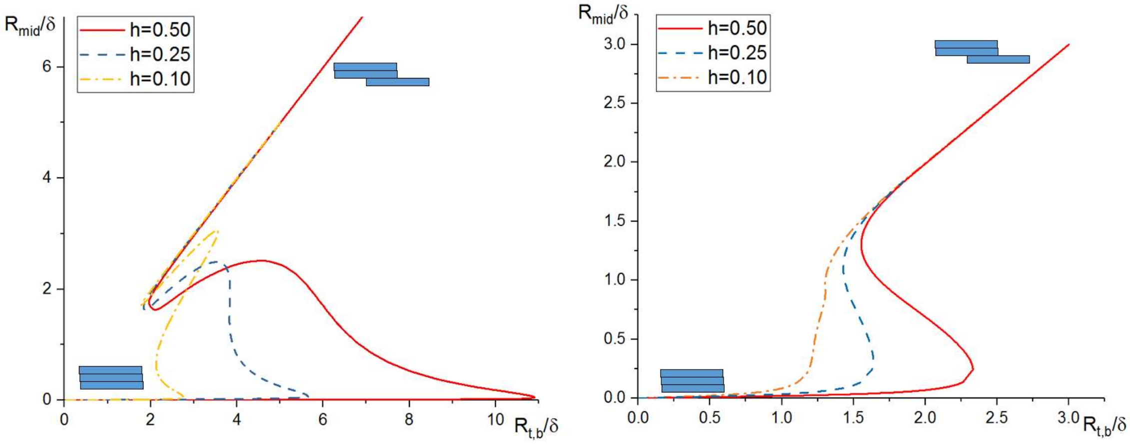

Fig.5.7 a) Brittle cohesive surface ($\delta=0.001$). b) Ductile cohesive surface ($\delta=0.01$).

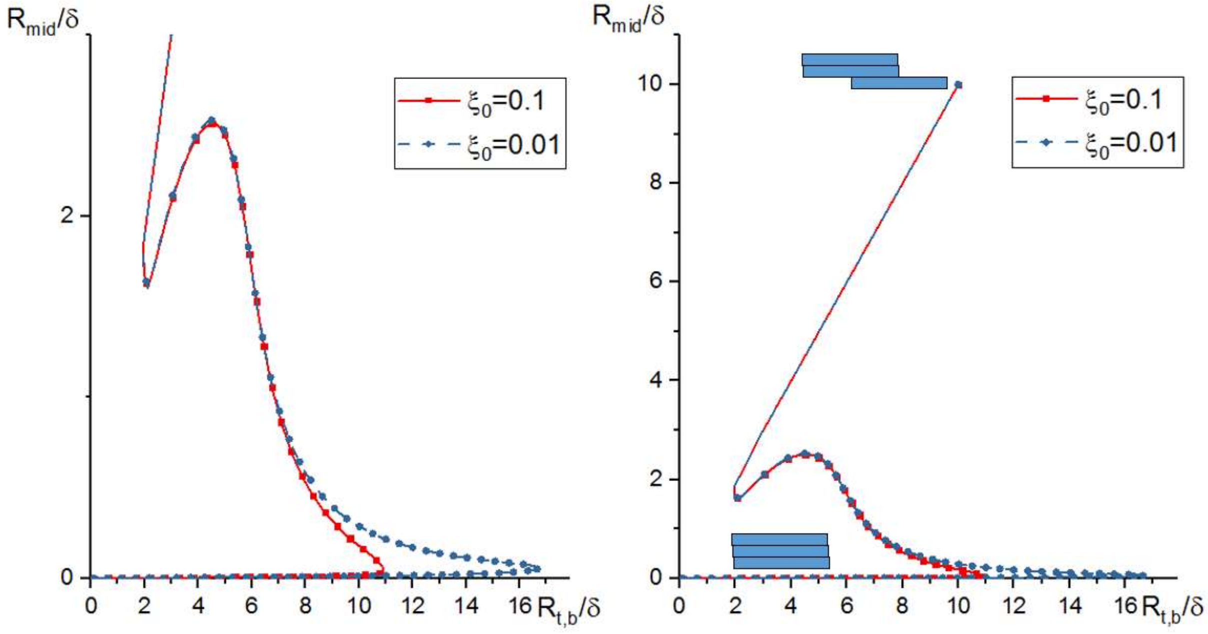

Fig.5.8 Brittle thick layer (varying defect size)

Figure.5.8 shows how the initial defect size affects the bifurcation behavior. Both cases presented here have small defects so boundary effects are negligible. The figure shows that the transition wiggle almost overlaps which means the transition process from symmetric configuration to ultimate asymmetric configuration through abrupt displacement jump is not affected by the size of defect. However, the controlled displacement which trigers the displacement jump and the asymmetric configuration, is different. It makes sense that the cohesive surface with a smaller initial defect can withstand a larger controlled displacement before the system becomes unstable and asymmetric.

5.3 Crack interaction and shielding in the tri-sublayer system

Analyses of an elastic solid containing non-dilute distributions of cracks (Fig.5.9) have been a problem of keen interest to the mechanics community ever since it was discovered that the elastic fields of a single crack will fundamentally change the general macroscopic behavior of the solid. Problems of this type have focused on either the change in SIF (Karihaloo [119]) due to crack-

crack interaction or the effective elastic properties of a solid containing a non-dilute distribution of cracks (Kachanov [118]). However, even though Karihaloo's work is superior to LEFM solution in the sense that it takes crack interaction into consideration, it is still limited by its mathematical complexity. Kachanov's work is useful from applications point of view because qualitative analysis can be done with minimal effort, but the smearing out of the details of the fracture process lead to confusing results since most of the crack problems are governed by local fields.

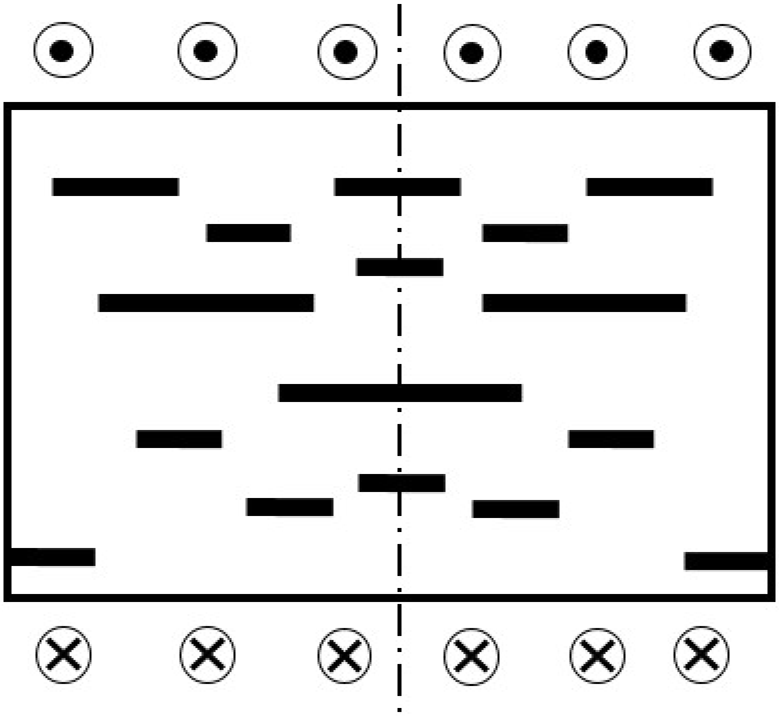

Fig.5.9 Elastic solid containing non dilute distribution of cracks.

In this subsection we focus on the exact solution to the defect tip local field as opposed to the effective property problem. For an example of the later problem including defect propagation see [88]. The analysis presented in this study can be applied to an elastic solid containing several parallel defect planes such that within each defect plane there will be either a single crack-like defect or an array of symmetrically placed defects. Instead of focusing on the distribution of interfacial fields (which has been discussed in detail in Section 4 of the two-sublayer system), this section mainly focuses on defect interaction and related issues. Based on the onset criterion for defect growth (i.e., a defect initiates when the critical slip or equivalently a critical cohesive surface traction is obtained), it is reasonable to take the maximum traction at the defect tip as a quantity that captures the near-tip field. This traction can then be used to compare the degree of stress concentration between different defect tips ultimately giving insight into defect plane behavior. The computational program has been verified by considering geometries which can degenerate to a two-sublayer system whose solution is known from previous sections. However, the validation of solutions for other defect geometries are limited by what is available in the literature.

5.3.1 Single-single defect, varying middle layer thickness (h^2).

In this subsection, the thicknesses of top and bottom sublayers are set to be equal, i.e., ($h^1 = h^3 = 0.5$), while the defect lengths are taken to be $\xi^{1,2} = \xi^{2,3} = 0.1$. Under these conditions, tuning the middle sublayer thickness can lead to two important geometries: i) for a relatively large middle sublayer thickness, the system can be reduced to a simpler one (two-sublayer with one defect) based on Saint-Vernant's Principal (Fig.4.5), ii) a reduction of the middle sublayer thickness, increases the effects of interlaminar defect interaction such that defect tip stress concentrations change leading to a change in the general defect growth behavior. Figure 5.10 shows that by utilizing symmetry in the thickness direction and making an imagined cut at the middle of the system, the tri-sublayer problem can be reduced to a two-sublayer problem with a slightly different boundary condition. The new surface created by the imaginary cut serves as the lower boundary of the simplified geometry. The two different limiting behavior can be distinguished by whether or not the new lower boundary (imagined cut) can be reduced to a uniform traction boundary condition. In other words, whether the middle layer is thick enough such that, regardless of the stress field perturbation of the other defect plane, the shear traction on that imagined cut plane asymptotically approaches the uniform distribution.

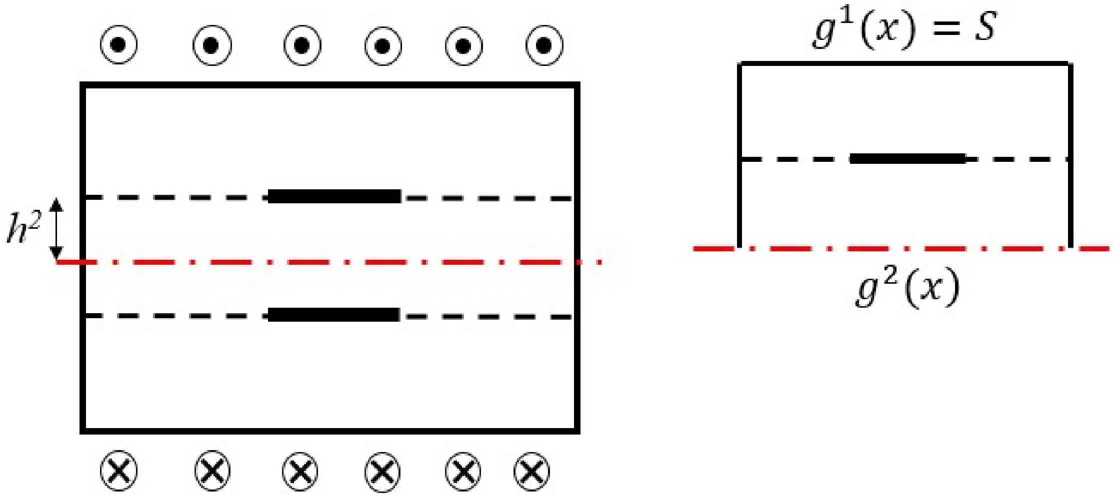

Fig.5.10 Tri-sublayer geometry and corresponding simplified two-sublayer subproblem.

In order to address the preceding concerns, the defect plane maximum stress ($\tau_{\max}$) of tri-sublayer geometries with different middle sublayer half thickness (h^2) has been plotted in Fig.5.11a. It clearly shows that when h^2 is more than 0.3 (three times the size of defect), the curve is close to a horizontal line which means the stress concentration is no longer changing with variation of middle sublayer thickness. This can be treated as a rule of thumb for neglecting defect interaction and for simplifying the complicated multi-sublayer system to a much simpler one without hurting accuracy. As the thickness decreases, the defect plane maximum stress decreases due to crack shielding. Figure 5.11b depicts crack shielding from the point of view of defect plane loading capacity ($S_{\max}$). As the thickness decreases, the maximum applied shear ($S_{\max}$) that the defect plane can carry increases which can only be explained by a reduced stress concentration since the defect geometries are exactly the same.

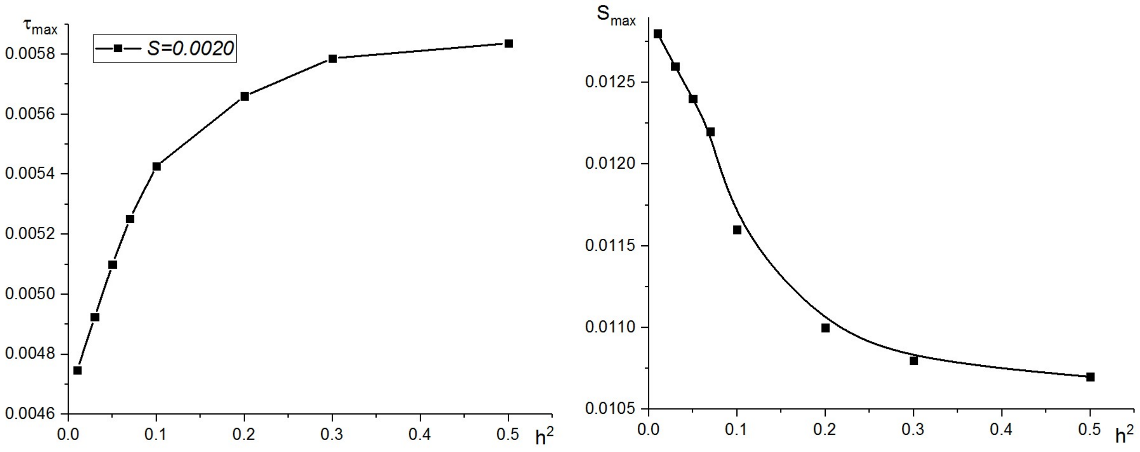

Fig.5.11 a) Defect plane maximum traction ($\tau_{\max}$) vs middle sublayer thickness. b) Defect plane critical load ($S_{\max}$) vs middle sublayer thickness ($h^1 = h^3 = 0.5$, $\mu^1 = \mu^2 = \mu^3 = 1.0$, $\tau_m^{1,2} = \tau_m^{2,3} = 0.018$, $\delta^{1,2} = \delta^{2,3} = 0.001$)

5.3.2 Single-single defect, varying bottom defect length ($\xi^{2,3}$)

The previous section contained an analysis of the effect of sublayer thickness and defect interaction and when it cannot be ignored. However, defect sizes were constrained to be the same which is not realistic. In order to study the effects of defect tip offset on the two planes, the middle sublayer is chosen to be thin enough (based on previous section, h^2 is chosen to be 0.05) so that the effect of interlaminar defect interaction is significant (Fig.5.12).

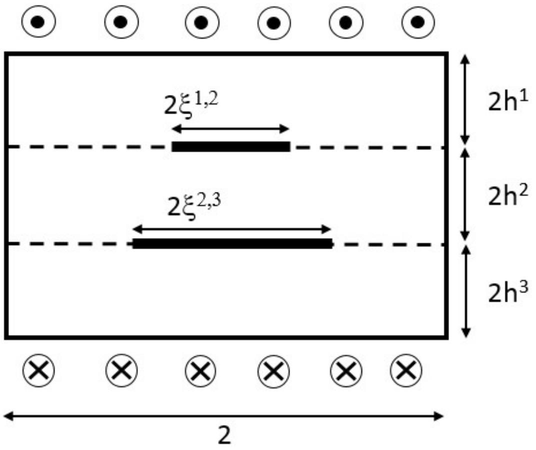

Fig.5.12 Tri-sublayer system with different defect sizes.

The defect of the 1st cohesive surface is set to the fixed value $\xi^{1,2} = 0.1$ while the size of the defect on the 2nd plane is changed in order to see its impact on the distribution of the 1st cohesive surface. There are two important factors that govern the shear distribution on the 1st cohesive surface, i) the direct presence of the defect on the top defect plane (which tends to cause a spike of cohesive surface shear traction around the defect tip), ii) the indirect perturbation by the nonuniform shear traction distribution on the 2nd cohesive surface. Figure 5.13a shows two qualitatively different distributions. For cases where the defect on the 2nd cohesive surface ($\xi^{2,3}$) is smaller than on the 1st cohesive surface, the shear traction distribution of the 1st cohesive surface is similar to the two-sublayer single defect cases (Fig.4.7). That is, the highest shear traction is located around the defect tip which means the presence of the defect on 1st cohesive surface dominates the shear distribution. However, for larger values of $\xi^{2,3}$, the shear traction field the of 2nd cohesive surface significantly affects the shear distribution of the 1st cohesive surface by suppressing the 2nd defect tip concentration and mapping its own larger defect tip stress concentration onto 1st cohesive surface. Under such circumstances, the defect on the 1st cohesive plane would not propagate before the 2nd one.

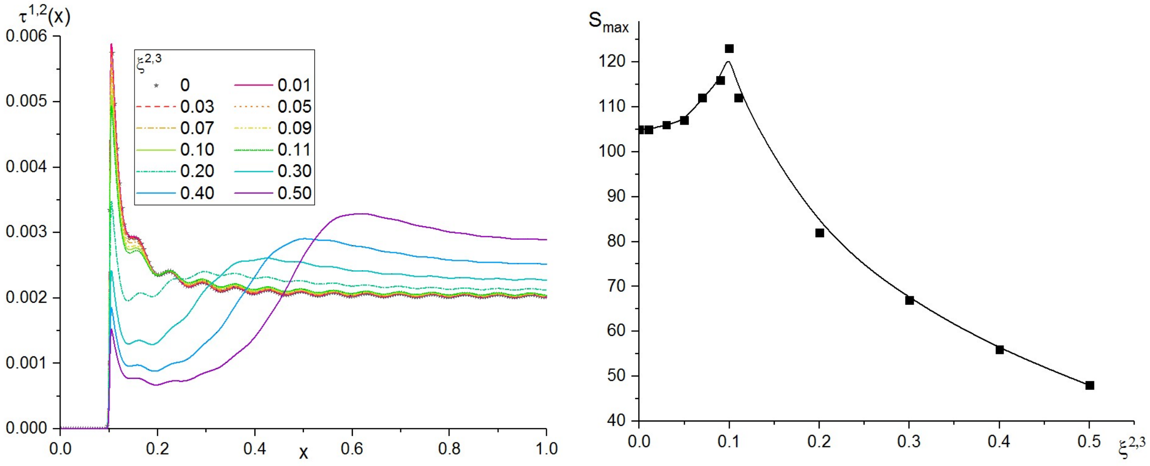

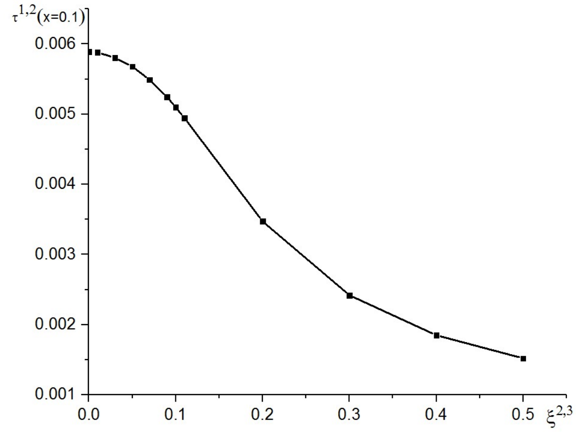

Fig.5.13 a) Shear traction on the first defect cohesive surface. b) Critical load ($S_{\max}$) vs size of defect on the second cohesive surface. c) Shear traction value at first cohesive surface defect tip ($h^1 = h^3 = 0.5$, $h^2 = 0.05$, $S = 0.0020$, $\mu^1 = \mu^2 = \mu^3 = 1.0$, $\tau_m^{1,2} = \tau_m^{2,3} = 0.018$, $\delta^{1,2} = \delta^{2,3} = 0.001$, $\xi^{1,2} = 0.1$).

The qualitative change (with the second defect size) of the shear distribution leads to the behavior of load capacity behavior shown in Fig.5.13b. The maximum point coincides with the equal defect length case where $\xi^{1,2} = \xi^{2,3} = 0.1$. For larger $\xi^{2,3}$, it is obvious that the load capacity drops since the intact region of the second cohesive surface is reduced and the second defect cohesive surface fails first. However, this argument is unable to explain the load capacity drop when $\xi^{2,3}$ is small since it's counterintuitive that a system with less defect can withstand less applied load. In fact, when $\xi^{2,3} < \xi^{1,2}$, the 1st cohesive surface fails first. Figure.5.13c shows that reducing $\xi^{2,3}$ to values smaller than $\xi^{1,2}$ leads to increasing stress concentration on the 1st cohesive surface which makes it more vulnerable to defect propagation.

5.3.3 Double-single defect, varying crack spacing.

An interesting modification of the previous single-single defect geometry is to split the defect on the 1st cohesive surface into two defects (Fig.5.14). The questions about defect behavior and defect tip stress concentration are not easy to answer since at least two antagonistic mechanisms are active.

First, splitting the defect would definitely introduce a new bonded region within the two inner defect tips. There will be defect interaction between the two inner defect fronts (suppose they are close enough) which may introduce a higher stress concentration within the bonded region (as discussed in Section 4.6) and, lead to a change in defect growth behavior. However, the newly introduced region (suppose its size does not exceed the bottom defect) is subject to a free boundary below it since it sits on top of the initial defect region of the second cohesive surface and this may act to relieve the stress concentration.

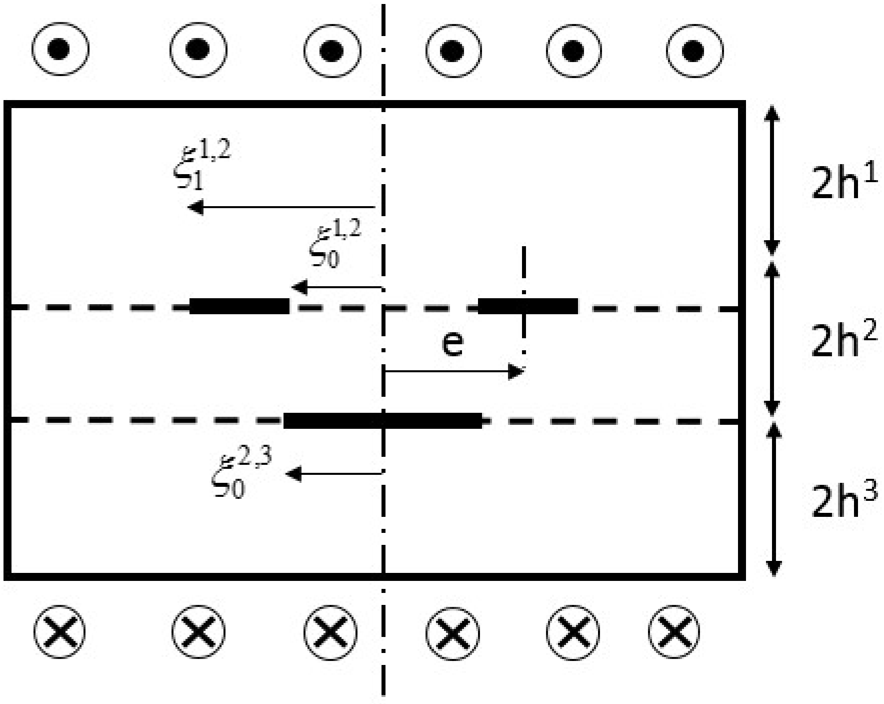

Fig.5.14 Double-single defect configuration

To study these two antagonistic mechanisms, and their effects on the stress redistribution on the top cohesive plane, keep the defect size and location on the bottom cohesive surface fixed ($\xi_0^{2,3} = 0.2$) and fix the defect size on the top cohesive surface ($\xi_1^{1,2} - \xi_0^{1,2} = 0.1$) as well, only vary the spacing ($\xi_0^{1,2}$). Note that in what follows, the following values of the parameters are fixed, i.e., $S = 0.0020,\ \tau_m = 0.018,\ h^2 = 0.05$.

For the most brittle case of Fig.5.15a, the figure shows that where the defect regions on the 1st cohesive surface are enclosed by the defect region of 2nd cohesive surface ($e \leq 0.15$, e is the location of the center line of defects on the 1st cohesive plane), the overall stress concentration (at the inner or outer defect tip) is relatively small compared to geometries with larger *e*'s. Furthermore, the outer defect tips ($\xi_1^{1,2}$) which are closer to the defect tip of 2nd cohesive surface ($\xi_0^{2,3}$) has a higher stress concentration than the inner ones. This behavior indicates the effect of the boundary (the nonuniform shear traction on the 2nd cohesive surface) dominates the in-plane two inner defect tip interactions. As the defect region of the 1st cohesive surface moves outward, the inner bonded region of the 1st cohesive surface is wider than the defect region of the 2nd cohesive surface, the stress concentration of the inner defect tip of the 1st cohesive surface is elevated and the relative magnitude of the shear stress at the two defect tips can also be switched ($e \geq 0.35$). This indicates that the inner defect tip would propagate first. However, for the case considered here (brittle cohesive surface with small δ), the defect will not propagate through the inner bonded region which indicates the defects on the 1st cohesive surface would not coalesce into one larger defect before the defect plane becomes unstable. It is also worth noting that when the outer defect tip approaches the side boundary, the overall stress concentration is reduced due to minimum defect interaction, but the outer tip which is close to the free boundary has higher stress concentration than that of the inner tip (similar to Fig.4.18b) due to the traction free boundary effect.

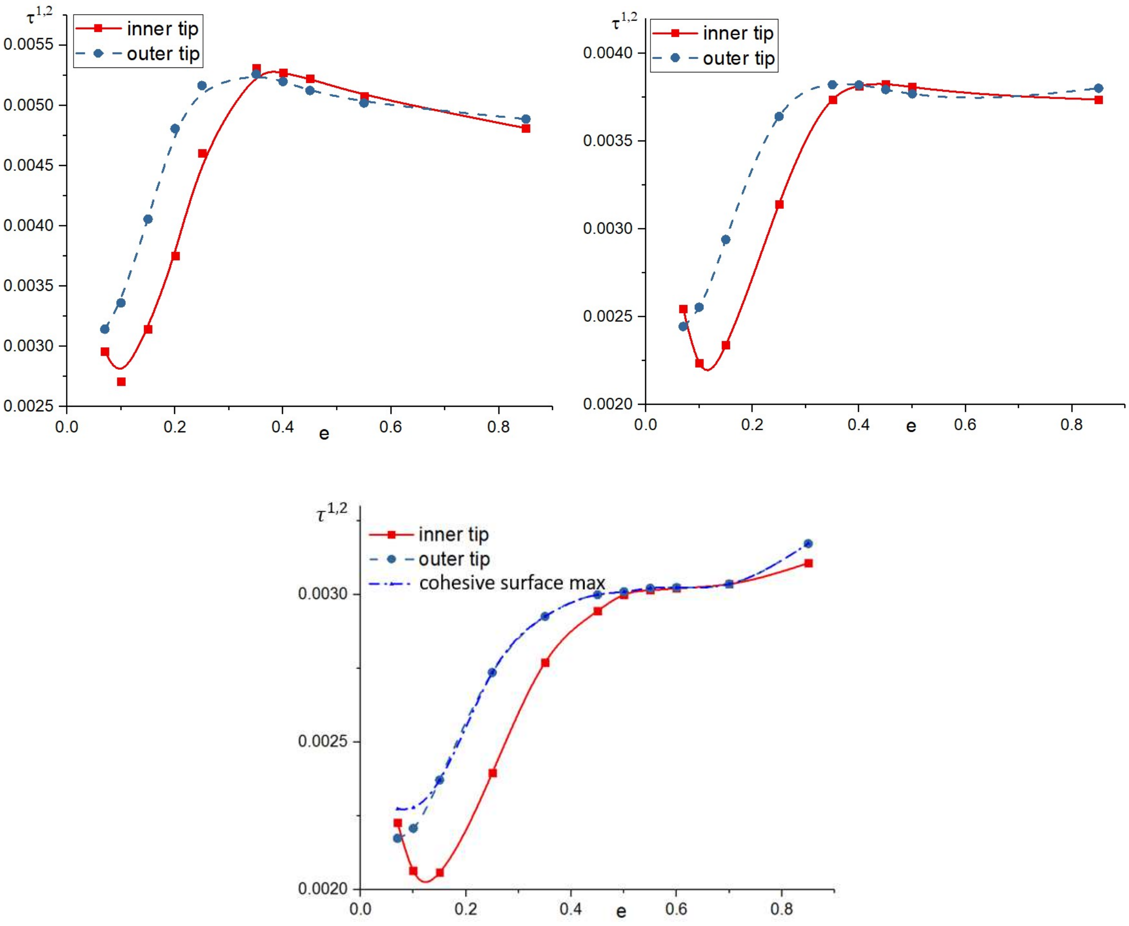

Fig.5.15 The maximum traction at both defect tips on the top cohesive plane. a: $\delta=0.001$. b: $\delta=0.003$. c: $\delta=0.010$.

The CFS can also be applied to more ductile cohesive planes without introducing any additional difficulties. Figure 5.15 b and c are plots for more ductile cohesive surfaces. There are generally two differences. The first one where the inner tips are closely located, (left most point for both plots, $e=0.07$), the inner tip has a higher stress concentration. This can be explained by the change of cohesive surface ductility. For the brittle cohesive plane, the traction decreases quickly from the maximum value at the defect tip. Once the spacing of in-plane defects is larger than the localized zone of elevated traction, defect interaction is not obvious. However, the more ductile cohesive surface has a more distributed stress pattern which leads to a more obvious in-plane defect interaction when they are closely located. The other difference is that for the most ductile case (Fig.5.15c), the cohesive surface maximum shear traction is no longer necessarily located at either original defect tip. The coupling effect leads to an unusual pattern for the cohesive plane shear traction redistribution as shown in Fig.5.16.

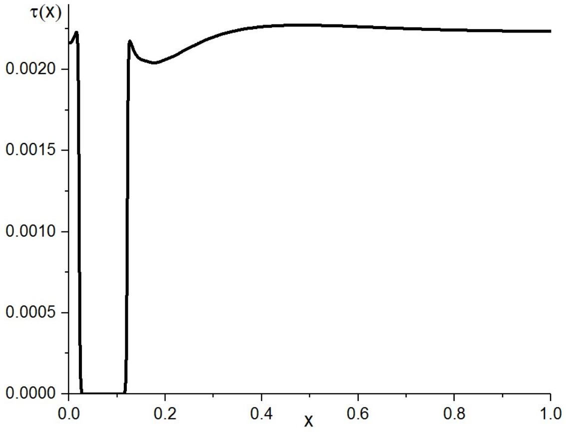

Fig.5.16 Traction distribution ($S = 0.0020,\ \delta = 0.010,\ \tau_m = 0.018,\ h^2 = 0.05,\ e = 0.07$).

In order to have the merging of defects on the 1st cohesive plane, several conditions need to be satisfied. These are,

i) ductile cohesive surfaces (same δ for both cohesive surfaces) which enables longer defect growth.

ii) a relatively small inner bonded region on the 1st cohesive surface such that limited defect growth can propagate through the inner bonded region.

iii) an even smaller center defect on the 2nd cohesive plane which strengthens the stress concentration at the two inner defect tips of the 1st cohesive plane which ensures that the inner tips would propagate first.

iv) A 1st cohesive surface that is weaker than the 2nd one so that the second cohesive surface would not fail before defect propagation through the inner bonded region of the 1st cohesive surface.

One defect geometry/cohesive plane that satisfies all of the above conditions is,

$$\begin{aligned} &\xi_0^{1,2} = 0.03,\ \xi_1^{1,2} = 0.13,\ \xi_0^{2,3} = 0.02 \\ &\tau_m^{1,2} = 0.010,\ \tau_m^{2,3} = 0.018 \\ &\delta^{1,2} = \delta^{2,3} = 0.005 \end{aligned} \tag{5.12}$$

Figure.5.17a shows that for a relatively small applied load (dashed line), the inner tip has a higher traction which indicates that the inner tip will propagate first as expected. For relatively high applied load (solid line), the inner bonded region has already reached the cohesive strength which means that the initial inner bonded region is compromised. This argument is made clearer by checking the cohesive surface slip field shown in Fig.5.17b which shows that when S=0.0080, the shear slip value of any point within the initial inner bonded region has passed the threshold of characteristic length ($\delta = 0.005$). Based on the defect tip definition introduced in the previous section (any point on the cohesive surface with a shear slip larger than the characteristic length, or equivalently, a cohesive surface shear traction exceeding the cohesive strength), the inner defect tip will propagate through the inner bonded region. It also shows that at S=0.0080, the shear slip of the outer tip has not reached the critical value which means the outer tip has not propagated yet. Only after the inner bonded region is totally compromised does the outer defect tip rapidly propagate from its initial position of $\xi_1^{1,2} = 0.13$ to almost 0.25 from which the defect plane becomes unstable.

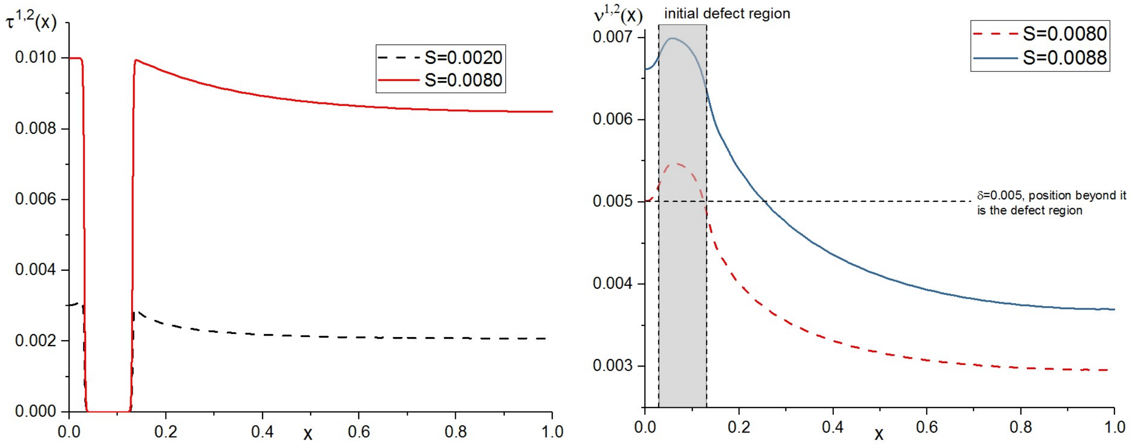

Fig.5.17 1st cohesive surface a) shear traction distribution. b) shear slip distribution.

5.3.4 Columns of defects of identical size but variable thickness

The purpose of this section is to determine the behavior of layered systems with columns of defects. Similar crack geometries have been considered by Kachanov [117], [118] and Karihaloo [119]. Kachanov [117] carried out a mode-I and mode-II stress analysis of a medium containing multiple collinear cracks employing superposition. His approximate analytical solution can be applied to both two and three-dimensional crack arrays of arbitrary geometry and, the approximate SIFs are accurate for closely spaced cracks. Apart from this study on the impact of interactions on individual cracks (especially SIFs), Kachanov also looked at the effective elastic properties of solids containing multiple cracks [118]. Kachanov's work revealed that the effect of introducing cracks into an elastic medium resulted in a reduction of the SIF while simultaneously reducing the stiffness of the material. Kachanov's work did not focus on anti-plane shear loading and this "paradoxical" effect is worth studying in that context. Figure.5.18 shows two geometries that will be analyzed in this subsection. Since the geometries considered by Kachanov are for the infinite domain, the cases considered here will minimize finite domain effects based on two different strategies. In the first case, the defect is located far from the traction free sides while the the second case satisfies a periodic condition.

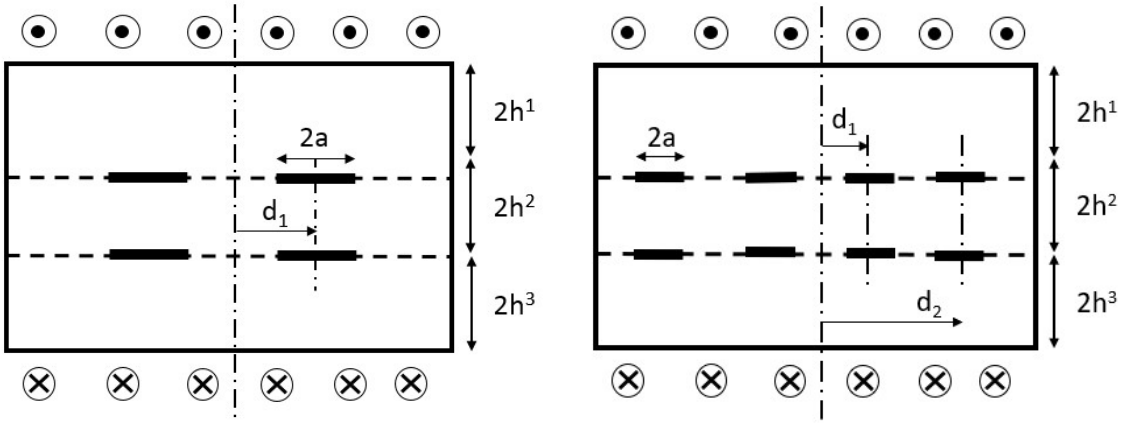

Fig.5.18 a. Two columns of defects ($2a=0.1,\ d_1=0.25$). b. Four columns of defects ($2a=0.1,\ d_1=0.25,\ d_2=0.75$).

Figure.5.19a shows the interlaminar defect shielding phenomenon that has been examined previously in the single defect geometry shown Fig.5.11a. However, the double column geometry has a smaller maximum cohesive shear traction than the single defect geometry (note they have the same defect region length) since the original defect was split into two smaller and well separated ones which would reduce the local stress concentration. Figure 5.19a plots the cohesive surface maximum shear traction ($\tau_{\max}$) versus middle sublayer thickness (h^2) for two columns and four columns of defect geometries. It shows that the four columns defect geometry has a slightly higher traction than the double column defect geometry. This behavior clearly shows the difference between SCS and CFS. From the point of view of SCS, remotely located defect tips should have negligible crack interaction. The local stress concentration is governed by the local defect geometry. However, the CFS governs the cohesive shear traction based on the argument of global equilibrium which takes the reduced bonded region into consideration automatically. Figure 5.19b shows the cohesive surface load capacity for the two geometries. Regardless of geometry, they all show that with decreasing middle sublayer thickness, the defect plane load capacity increases, which is similar to the single column defect geometry (Fig.5.11b). By checking the two curves, it shows that the two columns model always has a higher load capacity than its counterpart which is intuitive from the point of view of global equilibrium. However, compared to the two column model, the defect length in the four columns model doubled but the load capacity decrease is not proportion to the reduction of area of the initially bonded region. This behavior can be explained by the defect driven cohesive failure of a brittle cohesive surface which mostly is based on local field rather than a ductile linear spring like cohesive plane.

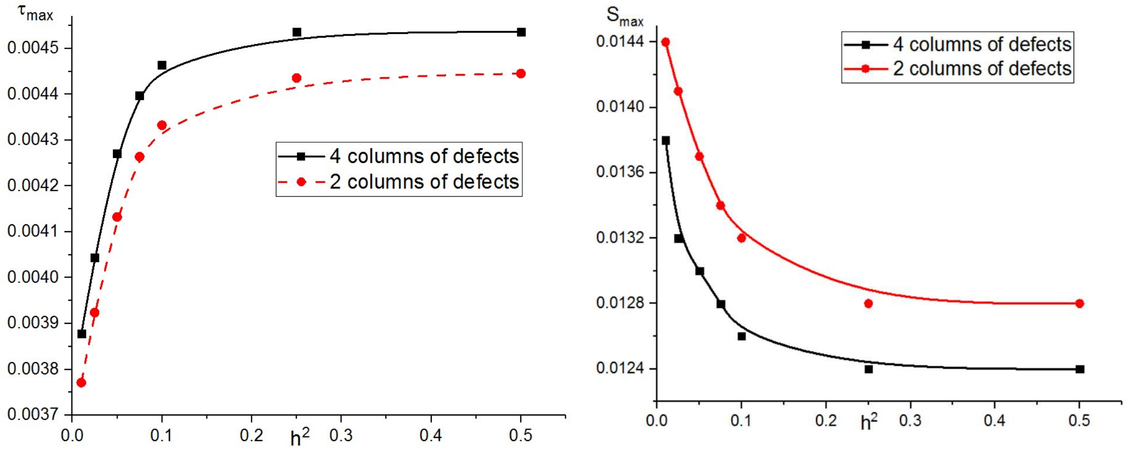

Fig.5.19 a) Cohesive surface maximum shear traction ($\tau_{\max}$) vs second sublayer thickness (h^2).

b) Cohesive surface maximum load ($S_{\max}$) vs second sublayer thickness.

5.4 Defect interaction and shielding in the four-sublayer system

In the previous section concerning the tri-sublayer system, the work focused primarily on interlaminar and intralaminar defect interaction. This was accomplished by studying the local stress concentration (which can be measured by cohesive surface maximum traction) when the system is subject to same small amount of applied load. However, the number of cohesive surfaces was limited to two which does not allow for consideration of more complex defect geometries with interlaminar symmetry, e.g., the diamond pattern and the columnar pattern of defects. In this subsection, the study mainly focuses on the effects of introducing a third nonuniform cohesive surface.

5.4.1 Single column of defects

The geometry of a single column of defects in a four-sublayer system is shown in Fig.5.20 and can be regarded as an extension of the corresponding tri-sublayer geometry by introducing another nonuniform cohesive surface. The modification seems trivial but in fact, it raises several interesting questions that are difficult or impossible to treat by other methods. These include i) what is the effect of introducing a new columnar cohesive defect, ii) are there any changes in the resulting defect propagation process, iii) what are the effects of changing the sublayer thicknesses in i) and ii).

In the following analysis, all sublayer thicknesses in each geometry were constrained to be identical. In other words, defects are spaced uniformly in the thickness direction. The cohesive strengths and characteristic lengths are set to be the same ($\tau_m = 0.018, \delta = 0.001$).

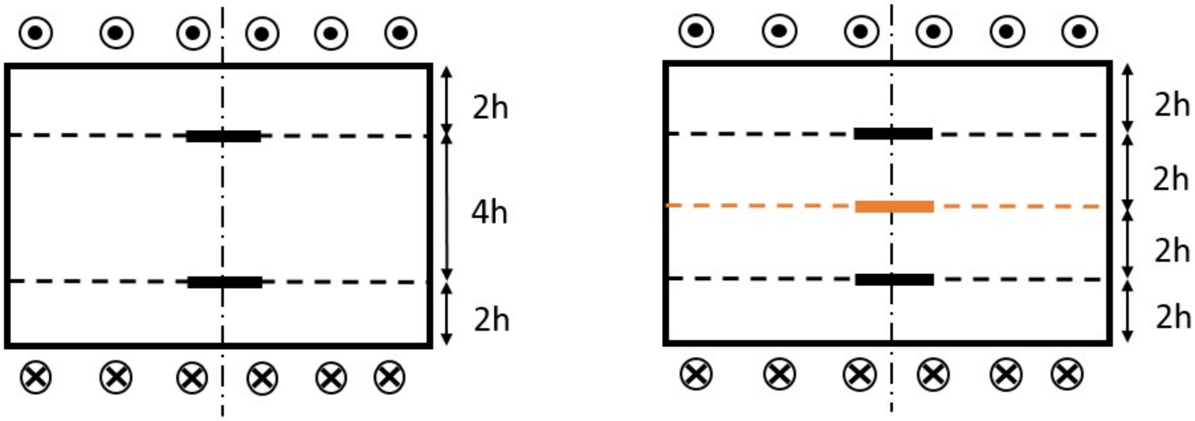

Fig.5.20 The four-sublayer geometry and the tri-sublayer geometry.

Single column of defects. The first case analyzed is a comparison between the four-sublayer system and the tri-sublayer system. This is done by requiring that the bulk material and cohesive surface properties be the same, including the defect sizes ($\xi_0 = 0.1$). Additionally, the thickness of the middle sublayer of tri-sublayer system will be assumed to be twice that of the top and bottom sublayers (Fig.5.20). One can expect that for thick sublayers, the introduction of a middle cohesive surface defect would have little impact on the stress redistribution of the other two existing cohesive surfaces. For thick sublayers, as one horizontal plane (parallel to the *x-z* plane) moves away from the top or bottom boundary in thickness direction, the shear traction on that plane reduces asymptotically to a uniform field. As long as such a horizontal plane with uniform shear traction in the media can be found between two cohesive surfaces, no matter how complicated the defect geometry of middle cohesive surface is, the traction of the top and bottom cohesive surfaces can be expected to reduce to a two-sublayer problem with an initial defect. Figure 5.21 indicates the correctness of this assumption since, for higher values of *h*, the curve for the maximum shear of the top cohesive surface converges to the same value regardless of the number of sublayers. By comparing the shape of the two curves, it is clear that they generally have the same behavior as predicted by the nonuniform two-sublayer problem (reducing the thickness tends to increase the stress concentration shown in Fig.4.14). The dash curve characterizing the tri-sublayer is always on top of the solid line. An examination of the two curves for the identical overall thickness shows that the maximum shear for the four-sublayer system is always lower than its counterpart tri-sublayer system. This seems counterintuitive since one might expect that the introduction of another defect to the system will generally tend to soften the system which would lead to failure at an earlier stage. However, this argument is based on a global point of view. From a local perspective, for the initial defect region, the introduction of a new middle nonuniform cohesive surface changes the corresponding top and bottom cohesive surface boundary conditions within the defect region ($-0.1 \le x \le 0.1$) from a distributed shear traction to a partially traction free region.

Locally, the newly introduced nonuniform cohesive surface reduces the amount of boundary traction to be compensated which in turn reduces the shear maximum. Globally, with a reduced maximum cohesive surface traction, it precipitates a more distributed shear traction field such that global equilibrium is satisfied. Figure 5.21 plots the maximum shear traction on top cohesive surface ($\tau_{\max}^{1,2}$) vs sublayer thickness (h). Since defect propagation is driven by local factors, the behavior in Fig.5.21 is reasonable.

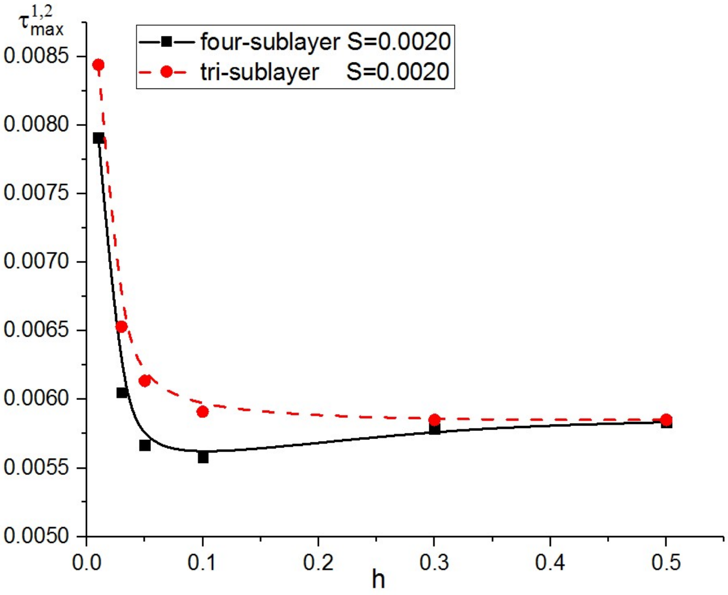

Fig.5.21 Single column defect geometry (tri-sublayers vs four-sublayers).

Single column of defects, varying middle defect size. The previous geometry restricted all defects to be the same size, i.e., $\xi_0 = 0.1$. In the following subsection, the middle defect size is altered and the effect on behavior is studied for different sublayer thicknesses. Here, all sublayer and cohesive surface properties are set to the same parameter values ($\mu=1.0,\ \tau_m=0.018,\ \delta=0.001$). Furthermore, the loading is assumed unchanged ($S=0.0020$). As in previous sections, the maximum shear tractions on the cohesive surfaces are compared and contrasted. Note that the sizes of the defects on the top and bottom cohesive surfaces are kept the same, their location fixed such that the traction distribution follows a similar pattern as the basic single defect fields (it's worth pointing out that when the sublayers are relatively thin and the middle defect is very large, the stress pattern has greatly changed and this argument no longer hold, refer Fig.5.24). Hence the cohesive surface maximum shear ($\tau_{\max}^{1,2}$) can be treated as an indicator of the local stress concentration. Comparing the maximum shears on different cohesive surfaces ($\tau_{\max}^{1,2}$ vs $\tau_{\max}^{2,3}$) resolves the issue of defect propagation sequence.

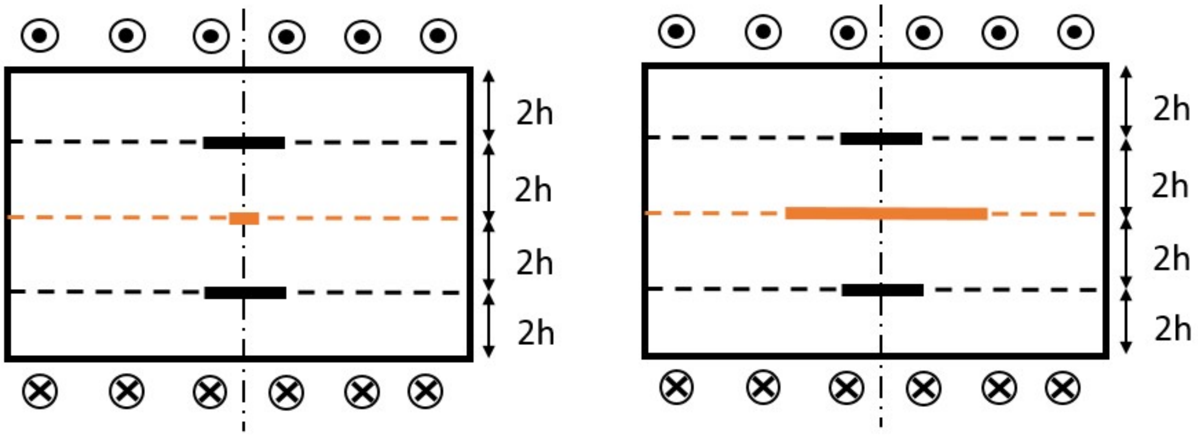

Fig.5.22 Four-sublayer system with columnar defect geometry for two middle layer defect sizes.

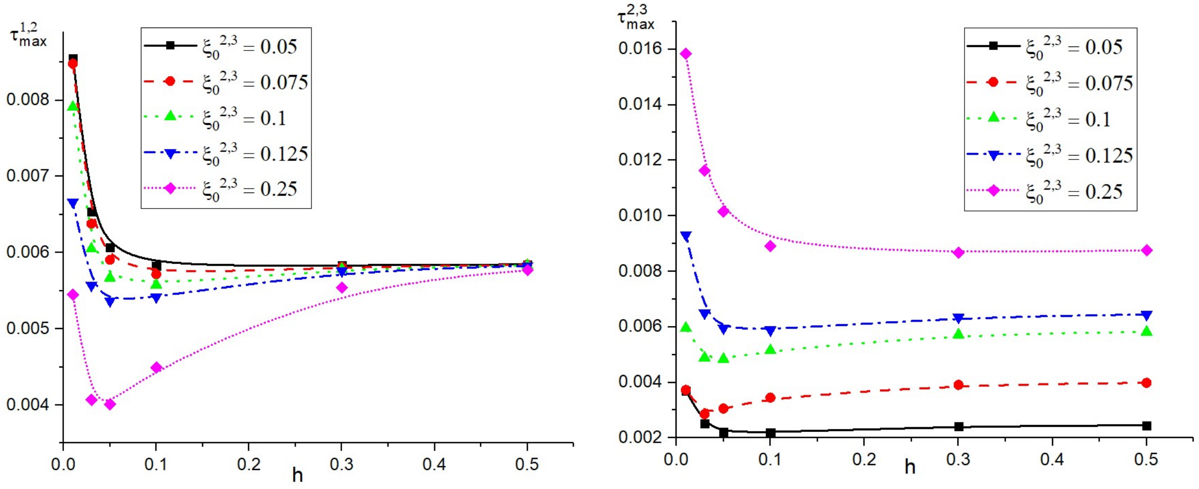

Fig.5.23 Maximum shear traction for different sublayer thicknesses and defect sizes.
a) 1st cohesive surface. b) 2nd cohesive surface.

Figure 5.23a shows that when the middle defect is no larger than top/bottom defect (top three curves), the top and bottom cohesive surfaces follow a similar pattern of behavior as the nonuniform bilayer geometry considered in Section 4.5, i.e., shrinking the sublayer thickness would increase the traction concentration which is manifested by an increasing maximum traction around the defect tip. However, when the middle defect is relatively large ($\xi_0^{2,3} = 0.25$), the bottom two curves indicate qualitatively different behavior. That is, under increasing thickness the traction concentration initially decreases, attains a minimum and then increases. This can be explained by checking the traction distribution of the first cohesive surface for those cases. Figure 5.24 shows the traction distribution for the bottom curve case in Fig.5.23a ($\xi_0^{2,3} = 0.25$). There are generally two competing factors governing the traction concentration. One is as discussed in previous sections, i.e., decreasing the thickness leads to increasing concentration. The other is that as the thickness decreases, the traction distribution of the second cohesive surface would project itself onto the first cohesive surface which, in the case of a relatively large second cohesive surface defect, would create a new traction pattern on the first cohesive surface with a second peak at the location where the second cohesive surface defect tip is located. The new stress pattern with two peaks would generally decrease the stress concentration at its original defect tip when the sublayer thickness is not considerably small (check cases of $h = 0.05,\ 0.03$ in Fig.5.24).

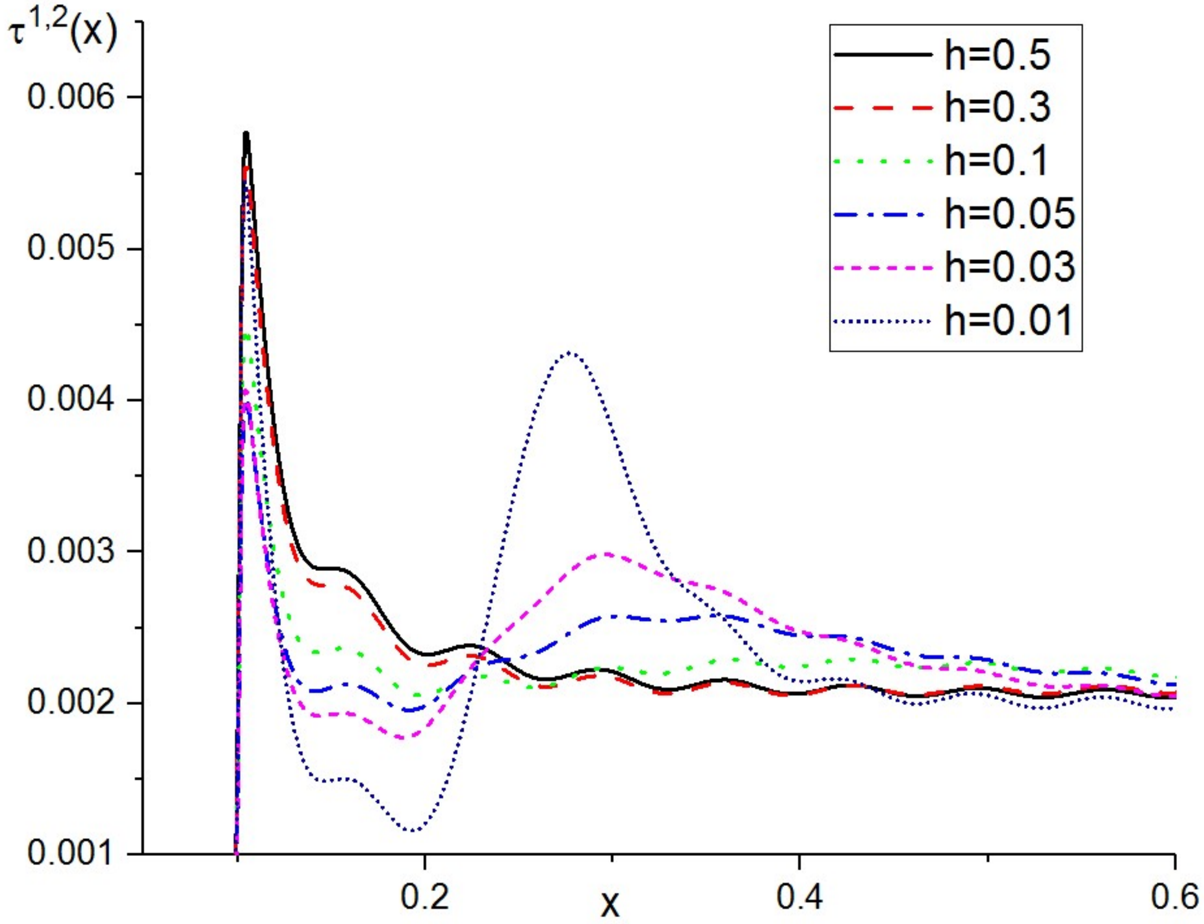

Fig.5.24 First cohesive surface shear traction ($\xi_0^{2,3} = 0.25$, $S = 0.0020$)

For geometries with a single column of defects, when the size of a certain defect is noticeably larger than the other two, the propagation initiates first from the larger defect. However, for a single column of defects of identical size, the defect propagation process is difficult to predict by simply examining the defect geometry. Figure 5.25 shows the cohesive surface maximum shear for different sublayer thicknesses with exactly the same defect geometry ($\xi_0 = 0.1$). Due to perfect symmetry in thickness direction, the 1st and 3rd cohesive surface should have exactly the same traction and slip fields. Figure 5.25 shows that the maximum shear traction on 1st (3rd) cohesive surface is always higher than their counterpart on the middle cohesive surface which indicates that the middle cohesive surface is stronger, and defects will propagate either from the 1st or 3rd cohesive surface. In Fig.5.25b the applied shear traction has been increased (the critical load of the thinnest sublayer system). The graph clearly shows that for the thinnest case at some particular point on the 1st and 3rd cohesive surfaces, the shear traction has reached its cohesive strength ($\tau_m = 0.018$) meaning that defects have already propagated whereas for the middle layer, they have not.

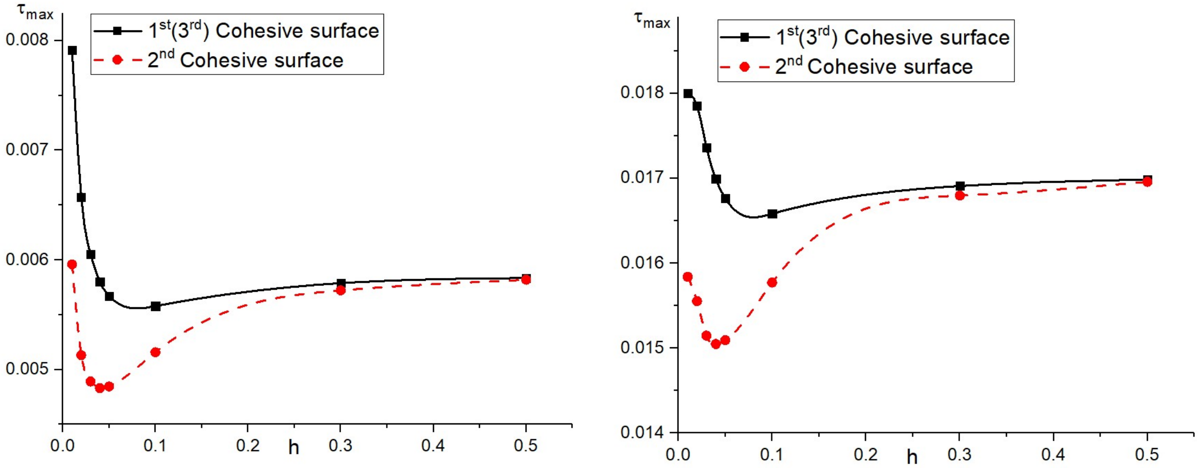

Fig.5.25 Cohesive surface maximum traction vs layer thickness. a) $S = 0.0020$, b) $S = 0.0070$

Note that the columnar defect geometry (Fig.5.22) can be generalized to multiple columns of defects as long as the geometry to be studied can be cut into simplified single defect columns provided that,

i) Each column of defects has a line of symmetry.

ii) The center line between the two new cut surfaces (dotted line) coincide with the line of symmetry of defects.

iii) The two new cut surfaces both have vanishing tractions. This can be satisfied by either cutting at the middle line between two adjacent columns of defects or, cutting is far from any defect tip such that the traction converges to the applied shear.

Figure 5.26 shows how a double column geometry can be reduced to a simpler problem that can be analyzed as a single column geometry (portion encircled by dotted line). However, sometimes conditions ii) and iii) cannot by both satisfied at the same time and, in those cases, the geometry cannot be simplified. In that case the complete geometry has to be considered. In general, the geometries that can be simplified are cases for which defects are well separated within the cohesive surfaces and far from the boundaries.

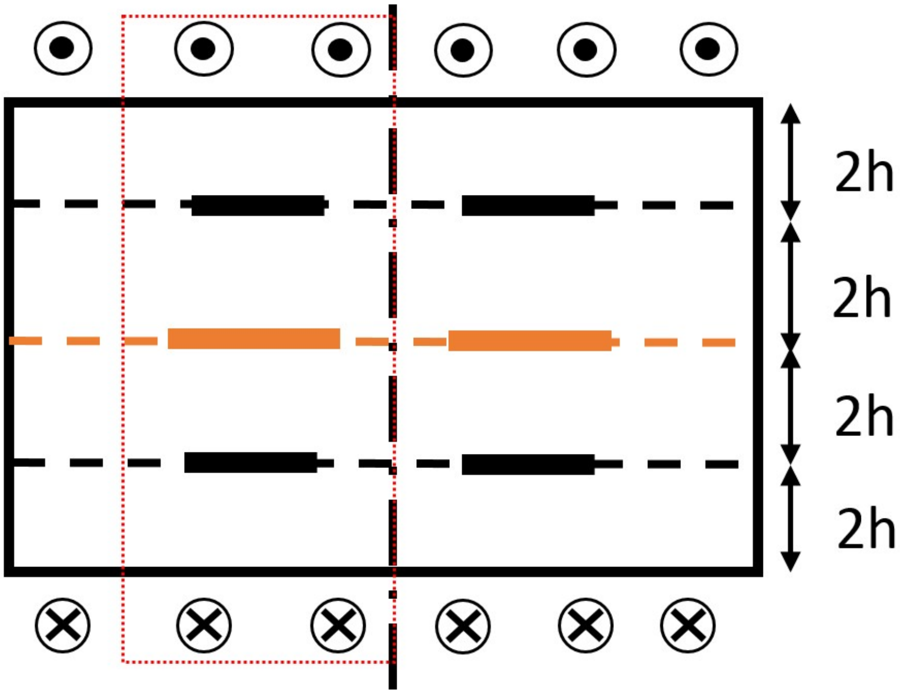

Fig.5.26 Analysis of two column geometry by a single column geometry.

Principal directions. Analogous to Section 4.8, this subsection concerns the orientation of potential mode-I micro cracks based on the same assumptions i.e., micro cracks are formed by maximum principal tensile stress. Recall that the mode multipliers govern the cohesive surface slip field rather than the actual deformation field of either sublayer. In order to obtain the stress component (σ_{xz}) related to the deformation of a certain sublayer, an algorithm needs to be developed obtaining the deformation field from the calculated multipliers. It is worth pointing out that for the middle cohesive surface which has top and bottom sublayers with perfect symmetry (including boundary conditions), the deformation field of its two constituent sublayers should be the same (Fig.5.27 right bottom). Hence, it is reasonable to distribute the calculated mode multipliers that govern the cohesive slip evenly to each sublayer's deformation field. However, this argument is not adequate for the top or bottom cohesive surface since the boundary conditions for the top and bottom sublayer are different (one is a uniformly distributed applied shear traction, while the other one is a non-uniformly distributed cohesive surface shear traction. These arguments are summarized in Fig.5.27).

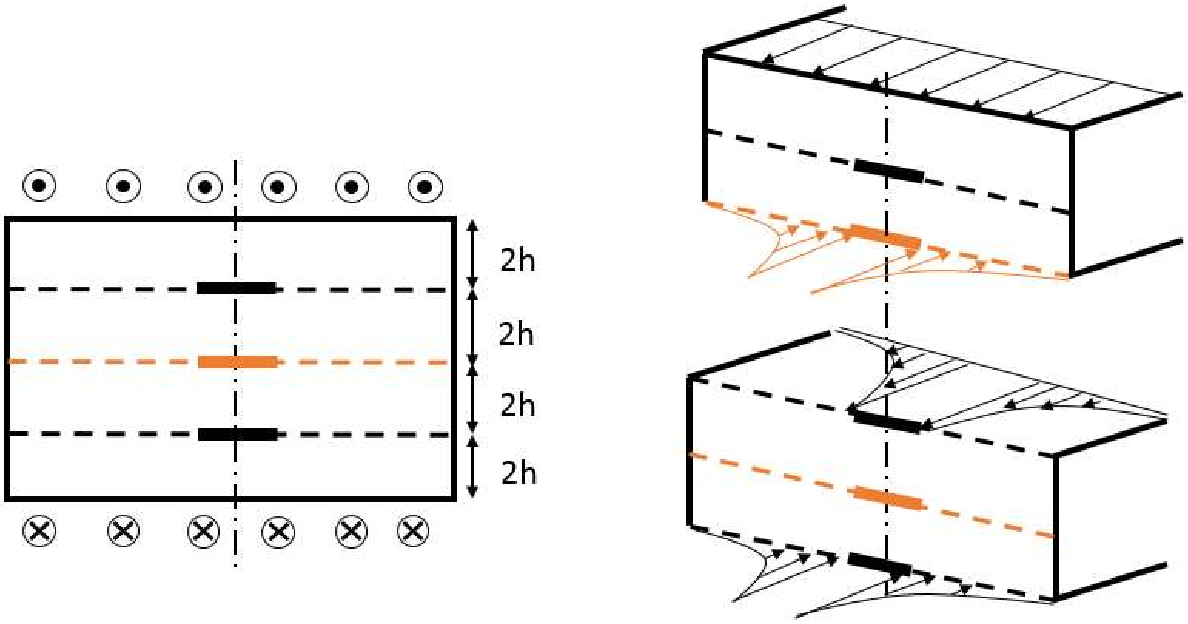

Fig.5.27 Four-sublayer center defect geometry with same sublayer thickness and defect size. Corresponding two-sublayer model for top and middle cohesive surface.

In such cases, the deformation field of each sublayer can only be calculated exactly by (4.8) and (4.9). Note that the higher order terms in (4.8) can be obtained by orthogonality process of (4.9). However, $D_0 + C_0 y$ does not contribute to σ_{xz}, so there is no need to go through the process to calculate it.

Because the defect geometry is similar to the two-sublayer centered defect geometry (Section 4.4), the stress fields have a similar distribution. It can be expected that the general trend for the principal direction varying W.R.T cohesive surface location should be the same as Fig.4.22, i.e., start from 90 degrees in the initial defect region since the governing stress component is σ_{xz} and converge to 45 degrees in the bonded region away from the defect tip because the governing component changes to σ_{yz}. Close to the defect tip, there will be a smooth but steep transition from 90 degrees to 45 degrees. Figure 5.28 shows the orientation of mode-I micro cracks of all cohesive surfaces with different sublayer thicknesses. It can be expected that when the layers are relatively thick, interlaminar defect interaction is negligible and all cohesive surfaces share similar cohesive surface tractions which are manifested by curves for different cohesive surfaces overlapping each other ($h = 0.5$ and $h = 0.3$ case) in Fig.5.28. However, when the layer is relatively thin, there will be significant differences in traction distributions between cohesive surfaces. The top and bottom layers tend to have stronger traction concentrations and the middle layer is affected by interlaminar defect shielding with less traction concentration. The cohesive surface with the stronger concentration has high values of gradient $\partial v / \partial x$ which is proportion to σ_{xz}. Because the relative magnitude of σ_{yz} and σ_{xz} governs the orientation, the top/bottom cohesive surfaces of the thin layer cases with comparable σ_{xz} would deviate more substantially from 45 degree and therefore would take longer to converge to the stable value of 45 degrees. The preceding discussion also explains why, for thinner layers, the principal direction of the middle cohesive surface converges to 45 degrees more rapidly than other cohesive surfaces. This argument can be studied by checking single sublayers of the system (Fig.5.29). Note that the stress component σ_{xz} on a cohesive surface is basically compensating the difference between shear force (integration of applied shear) on the corresponding boundary and the reactive cohesive surface shear force. Proceed as discussed in Section 3.5, make a fictitious vertical cut closely ahead of the defect tip (dashed line on Fig.5.29). Fig.5.29 shows the single sublayer configuration and the corresponding shear traction distribution on each surface, the shear tractions on top and bottom surface for each configuration are combined and plotted on the right within one coordinate. For the top sublayer, the deficit of the shear force on the cohesive surface (compared to top surface) caused by introducing a defect can be expressed by the difference of the area between region 1 and region 2 labelled on Fig.5.29. However, for the middle sublayer (both top and bottom boundaries having a defect), the shear traction distribution for those two surfaces are very similar (Fig.5.29 bottom) and a relatively small deficit is obtained. The unbalanced shear force deficits can only be obtained by another stress component (σ_{xz}) on the fictitious cut surface, and the magnitude of σ_{xz} is proportion to the deficit. Hence, for the middle sublayer which a smaller shear force deficit introduces a smaller σ_{xz} , the orientation of mode-I micro cracks should converge to its stable value of 45 degrees faster. Note that for relatively thick sublayers, the interlaminar interaction is negligible and regardless of which cohesive surface is considered, they all can be reduced to the same two-sublayer system. This argument is also shown in Fig.5.28 by checking cases $h=0.3$ and $h=0.5$.

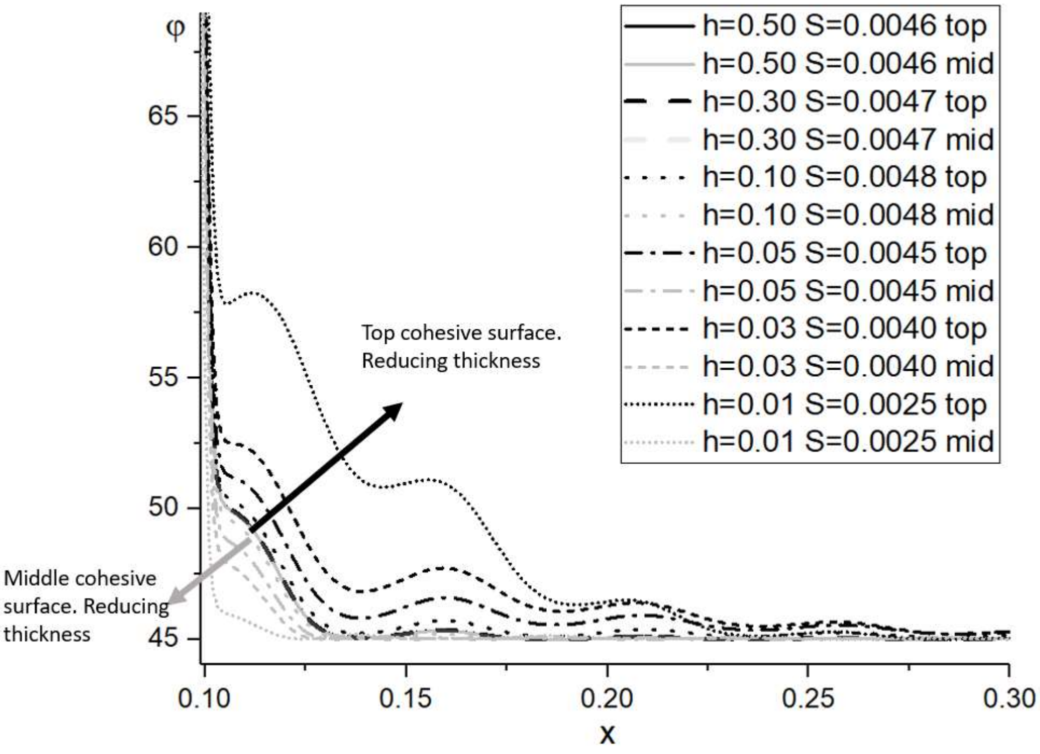

Fig.5.28 Distribution of principal tensile stress orientation φ.

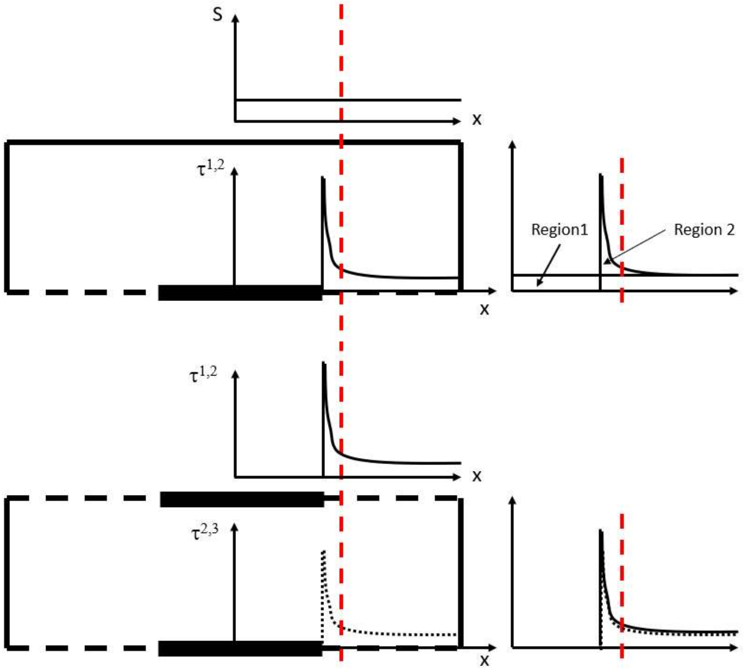

Fig.5.29 Single sublayer configuration and shear traction distribution.

Defect propagation process. This section serves as an extension of Section 4.7 which mainly concerns the criteria for primary defect propagation based on the traction and slip fields obtained by CFS. This section mainly focuses on more complex propagation phenomena, the comparison between the location of the primary defect tip and the potential location of mode-I micro cracks are addressed. Related topics include, i) the sequence of propagation (micro cracking vs primary defect propagating on a particular cohesive surface) and ii) comparison between the sequence of propagation between different cohesive surfaces and, how changes in the constitutive parameters alter the prediction of two different propagation processes. Before any discussion of the propagation process, it is first necessary to clearly define the propagation criteria for primary defect growth and mode-I micro cracking. These include, i) the primary defect propagation criterion, which is closely related to the cohesive law, ii) the mode-I micro crack initiation criterion that characterizes a bulk material's resistance to tensile fracture. Note that the CFS determines the traction fields and because of this, stress-based (or critical slip criteria) propagation criteria are chosen for consistency. For the primary defect, the propagation criterion is defined as in Section 4.7 and once the cohesive shear traction reaches its maximum value (τ_m) or equivalently the cohesive surface slip value reaches the characteristic length (δ), the primary defect propagates. Note that the parameters of the propagation criterion for the primary defect is directly related to the cohesive law and cohesive relation is only applicable to the cohesive surface (i.e., the fictitious surface along which the primary defect is assumed to be propagate).

Before defining the criterion for micro crack initiation, it is necessary to understand the fundamental differences. These include, i) the fact that a mode-I micro cracks arise from an imperfection of the bulk material in the vicinity of the cohesive surface rather than a clearly predefined and easily modelled initial defect, ii) a matrix where the micro cracks initiate is the bulk material as opposed to the fictitious cohesive surface on which the primary defect propagates. The first difference means that the CFS analysis of mode-I micro cracks cannot follow the procedure used in studying primary defect. Unlike the primary defect whose calculated fields can be used to define the current primary defect tip (based on certain criterion), mode-I micro cracking is a much complicated phenomenon. Because of this, the calculated fields can only give a prediction about the region where certain micro cracking criterion is satisfied (characterized by potential micro cracking boundary ξ_m). Some researchers did study the propagation process, orientation and shape of micro cracks by introducing predefined inclined notches. The orientation of these notches is predetermined by testing. The criterion for micro crack propagation is based on the fracture toughness in the vicinity of perturbed notches [120]. The same group of researchers also carried out phase field analysis by introducing randomly distributed small imperfections (rather than predefined notches near the primary defect tip). This was done in order to study the orientation and merging of micro cracks. The phase field formulae accounting for damage is also based on the maximum tensile stress criterion ($\sigma_p = \sigma_m$) [121], where σ_p is the maximum principal stress and σ_m is the tensile strength of the bulk material.

The second difference suggests that mode-I micro cracks are governed by a different set of parameters rather than what has been used to characterize the primary defect plane. The relation between the parameters characterizing cohesive surface behavior, and a new set of parameters characterizing the resistance to tensile fracture can be different based on the actual problem. If the cohesive surface is a fictitious one, the two sets of parameters are characterizing the same material and need to be consistent (τ_m and σ_m, the cohesive strength of the surface and the tensile strength of the bulk material, are related by certain yield criteria depending on different types of bulk material). However, if the cohesive surface is an actual surface of adhesion that bonds two distinct layers, the two sets of parameters characterize two different materials (bulk and adhesion), and their relation has to be built by setting the shear modulus of the bulk material as a primary parameter and the relative magnitude of cohesive strength of the adhesion has to be derived.

In this subsection, the method of characterizing micro cracking by maximum tensile stress criterion ($\sigma_p = \sigma_m$) is applied. No distinction is made about whether the cohesive surface is fictitious or not. The study mainly is focused on defining a region in the vicinity of the propagating primary defect tip such that the principal tensile stress within it exceeds a certain value, i.e., the maximum tensile stress criterion is met. The cohesive surface is taken to be brittle ($\delta = 0.001$) and the cohesive strength is assumed to be the same as in previous calculations, i.e., $\tau_m = 0.018$. Thus, existing results can be used for comparison. The following results focus on three aspects, i) differences between the top and middle cohesive surfaces, ii) how a change in sublayer thickness affects cohesive surface behavior, and most importantly, iii) the effects of the ratio $\eta = \tau_m / \sigma_m$ which measures the resistance to failure in two different ways (τ_m characterizes the resistance to shear failure on the cohesive surface, σ_m characterizes the resistance to normal failure in the bulk material).

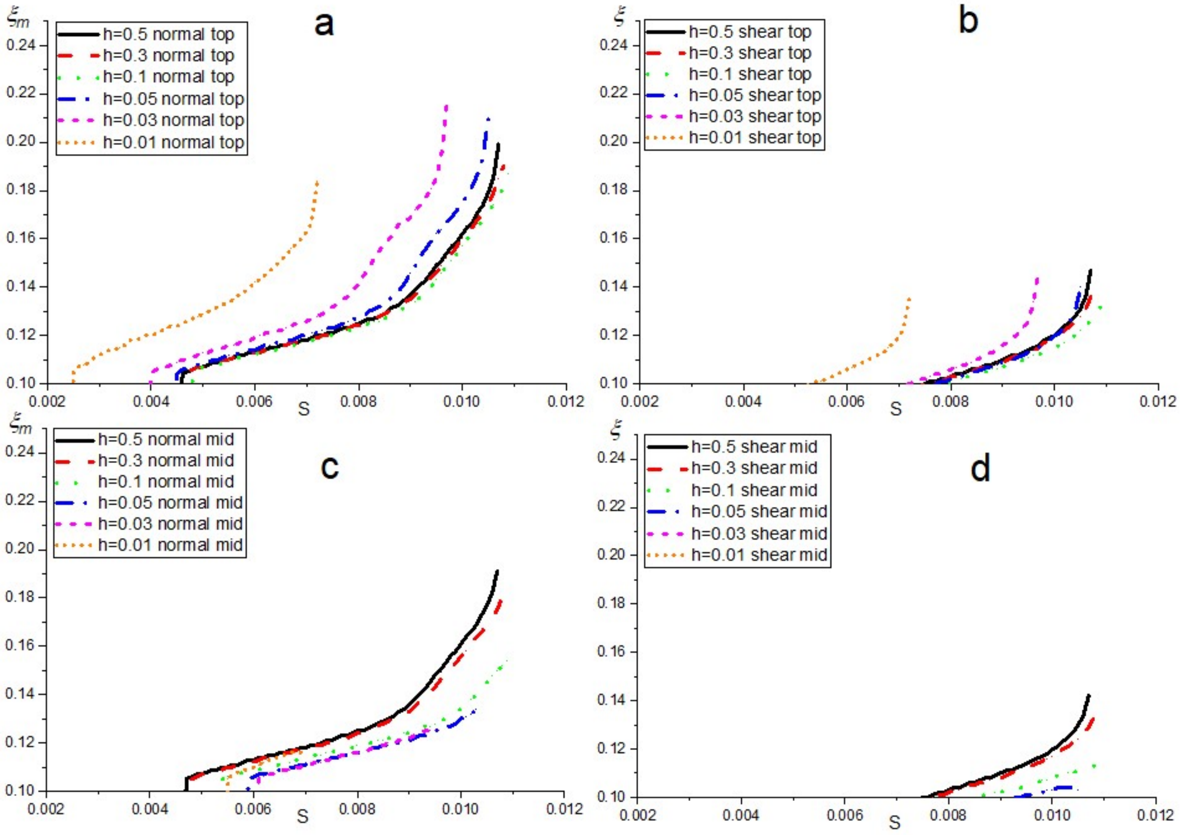

Fig.5.30 Location of primary defect tip (shear) and boundary of potential micro cracking (normal) for top and middle cohesive surface. ($\eta = 1.2$) a) top cohesive surface, normal failure. b) top cohesive surface, shear failure. c) middle cohesive surface, normal failure. d) middle cohesive surface, shear failure.

In order to answer i) and ii) of the previous paragraph, the primary defect tip location (ξ) and potential micro cracking boundary (ξ_m) has been plotted separately in Fig.5.30, based on the cohesive surface defect propagation criteria given above. First compare graphs on the same column (same propagation criterion, either potential micro cracking boundary or defect tip of shear failure), note that when h is relatively large, the behavior of crack propagation of the middle cohesive surface is almost the same as its counterpart on the top cohesive surface ($h = 0.5$ or 0.3). Graphs in the same row (same cohesive surface) shows that the potential micro cracks caused by a normal criterion propagate first and will propagate deeper into the initially intact region. This behavior is observed in various brittle material testing including both torsion of a cylindrical bar and the shearing of layered systems [27], [33], [37]. For a discussion about thickness effects, focus on Fig.5.30b first since it is directly related to the cohesive shear field.

In previous section, Figure.5.21 clearly shows how the cohesive traction concentration changes with respect to a changing thickness. From $h = 0.5$, the local traction concentration slightly decreases until $h = 0.05$. After that, the traction concentration tends to increase, when $h = 0.03$ it has already surpassed the starting value becoming significantly larger as the thickness further decreases. Note that the local traction concentration is measured by the maximum shear traction under the same load which is also the criterion for primary defect propagation. The above argument can be used to explain the why reducing sublayer thickness first delayed primary defect propagation and then stimulates it.

Fig.5.30b shows that from $h = 0.5$ to $h = 0.05$, defect initiation is slightly delayed and, for the case of $h = 0.01$, the defect propagates much earlier than the other cases. Similar behavior also appears in Fig.5.30a, the boundary of potential mode-I micro cracking. The above argument also provides an explanation for the behavior of the middle cohesive surface (Fig.5.30 second row). Figure 5.23b ($\xi_0^{2,3} = 0.125$) shows a similar change in stress concentration for $h \geq 0.03$, but not a rapid increase for case $h = 0.01$. The defect propagation process follows a similar pattern with one exception. For $h = 0.01$, no curve for $h = 0.01$ is observed in Fig.5.30d which means that the primary defect will not propagate at all due to the interlaminar shielding effect.

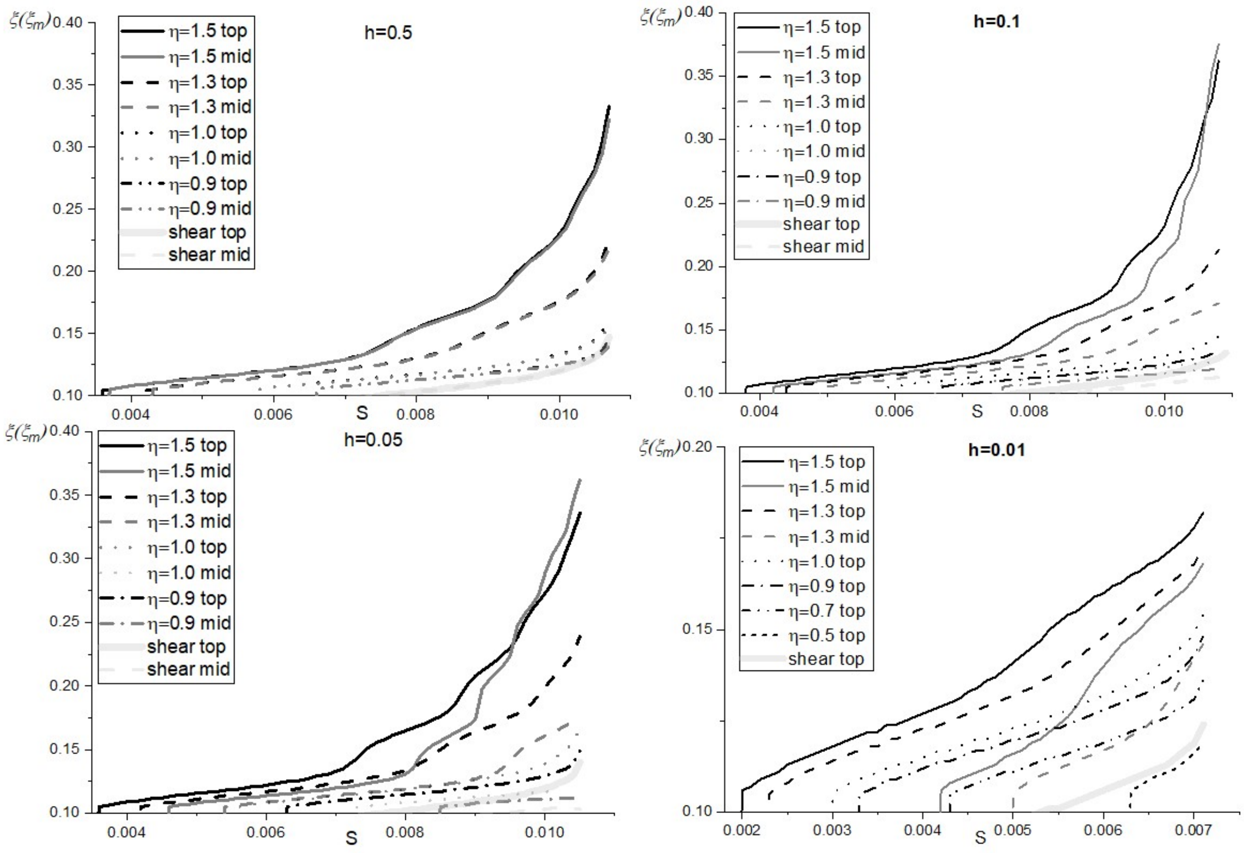

Fig.5.31 Location of primary defect tip (ξ) and boundary of potential micro cracking (ξ_m) for top and middle cohesive surface.

Figure 5.31 shows the defect tip location of both top and middle cohesive surfaces for different values of η and sublayer thicknesses. For a fixed cohesive strength, higher values of η leads to smaller value of σ_m which makes the micro crack propagation criterion more easily to be satisfied. An examination of the figure indicates that those curves with higher η values generally are on top of their counterparts. Therefor a smaller value of applied shear (*S*) is required to trigger the micro cracking and the potential micro cracking boundary departs from the initial defect location ($\xi = 0.1$). Note that the light grey lines labelled "shear top" and "shear mid" represent the primary defect propagation process due to shear which will not change with varying η. They indicate that the tips of primary defects are generally always behind the potential boundary of micro cracks.

This result is consistent with the commonsense notion that the propagation of a primary defect is driven by the coalescence of existing micro cracks ahead of it. How far the micro cracks are ahead of the current primary defect is largely dependent on the relative magnitude of the parameters $\eta(=\tau_m / \sigma_m)$ characterizing the resistance of tensile failure of the bulk material and cohesive shear strength within the potential micro cracking region. The first three cases in Fig.5.31 show the discrepancy (distance between micro cracks and primary defects) increase as the primary defect propagates. This fact is consistent with results from the literature that assert that the discrepancy is proportional to the characteristic length of the primary defect ([120]).

5.4.2 Diamond pattern of defects

Apart from the columnar defect geometry, another interesting geometry that consists of multiple sublayers system is the diamond pattern array of defects ([117], [118], [119]). The fundamental difference between the two geometries is that in the columnar pattern, the defects line up by the same center line, whereas for the diamond array, the defects on the middle cohesive surface are offset by a certain distance from their counterparts on the 1st and 3rd cohesive surface. Figure 5.32 shows the most basic unit that characterizes one "diamond" pattern.

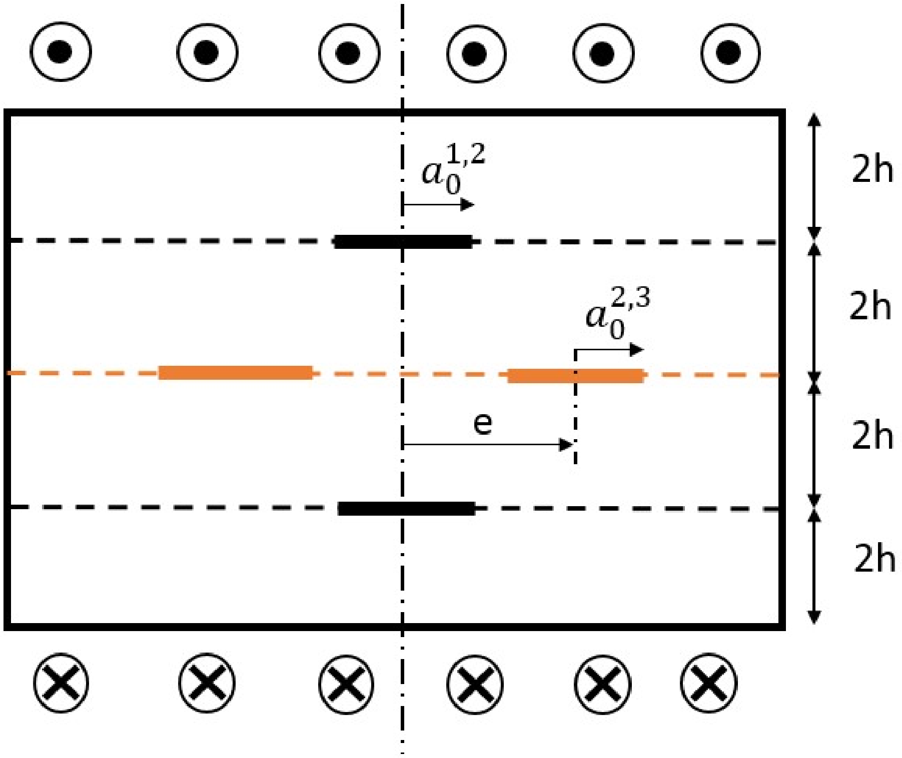

Fig.5.32 Schematic sketch for a single-double-single (S-D-S) diamond array of defects.

Although defects formed during the manufacturing process or during service are randomly distributed, nonuniform cohesive surfaces with predesigned patterns take advantage of certain symmetries. These may be reduced to one of the following three, i) the most basic geometry of a two-sublayer system containing a center defect (well-separated defects and relatively thick sublayers), ii) a columnar defect pattern (defects line up in thickness direction), iii) a geometry constructed by stacking the basic "diamond pattern" side by side (satisfying certain periodicity conditions). In this subsection the diamond pattern geometry is considered to be perfectly symmetric with respect to the middle cohesive surface (1st and 3rd cohesive surfaces are exactly the same), and the total size of the defect region (two defect sizes combined on the middle cohesive surface) on each cohesive surface is the same. In this subsection, $a_0^{1,2}$ represents the defect half length on the top cohesive surface between the 1st and 2nd sublayer, and $a_0^{1,2} = a_0^{3,4}$ will be assumed due to an enforced symmetry in the thickness direction. The quantity $a_0^{2,3}$ is the defect half length of the middle cohesive surface which can be different from its counterpart on the other two cohesive surfaces. The offset distance of defects' centerline is labeled as *e*[12]. Note that this set of parameters ($a_0^{1,2}$, $a_0^{2,3}$ and *e*) can also be transformed into a set that describes defect fronts (i.e., $\xi_0^{1,2}$, $\xi_0^{2,3}$ and $\xi_1^{2,3}$). Analogous to Section 5.3, the following section mainly focusses on stress concentrations for various defect geometries.

Varying offset distance "e": The offset distance *e* of the 2nd cohesive surface affects the cohesive traction distribution as follows. First, the offset distance controls the defect geometry of the second sublayer, for $e = 0.05,\ a_0^{1,2} = 0.1,\ a_0^{2,3} = 0.05$ the defect pair of the second cohesive surface degenerates to a single defect. In that case, the geometry can be treated as single column of defects. Second, for offset values slightly greater than 0.05, there will be a small bonded region within the two inner defect tips which should experience an increased stress concentration due to interactions of the defect tips. Finally, a relatively thin sublayer thickness will cause defect interaction in the thickness direction as well.

Figure 5.33 shows the traction distributions of two cohesive surfaces for different offset values. Note that the geometry of the 1st cohesive surface is held fixed ($a_0^{1,2} = 0.1$). Regardless of different defect states of the 2nd cohesive surface, the defect tip on the 1st cohesive surface always has the strongest traction concentration (similar to single column defect geometry shown in Fig.5.25a). It is worth noting that small wiggles can be detected near the location where there is a defect tip on the 2nd cohesive surface. However, these small wiggles do not affect the general shape of the traction pattern and cause no ambiguity in the defect driven 1st cohesive surface behavior. For the

---

[12] The offset distance is also nondimensionalized by layer half-length.

second cohesive surface, the response is quite different in the sense that, i) there can be either one or two defect tips (depending on the offset distance) leading to qualitatively different traction distributions, ii) the traction distribution and the local traction concentration at the tip is greatly affected by the defect geometry of the 1st and 3rd cohesive surface. The two values of e ($e = 0.05, 0.95$) in Fig.5.33b are limiting cases and are such that there is only one defect tip observed on one half of the 2nd cohesive surface. Though the traction distributions are similar as long as the *x*-axis is translated, the degree of stress concentration is different. The left and right most red dot points in Fig.5.35 (e=0.075) clearly shows that when the 2nd cohesive defect is located near the free side surface, it's maximum cohesive shear (which is generally lower than that on the 1st cohesive surface) becomes equal to its counterpart on the first cohesive surface. This can be explained by, i) instead of four, now there are just two defect tips on the middle cohesive surface which resembles its counterpart on the 1st cohesive surface, ii) distantly located defect tips minimize interlaminar defect interaction.

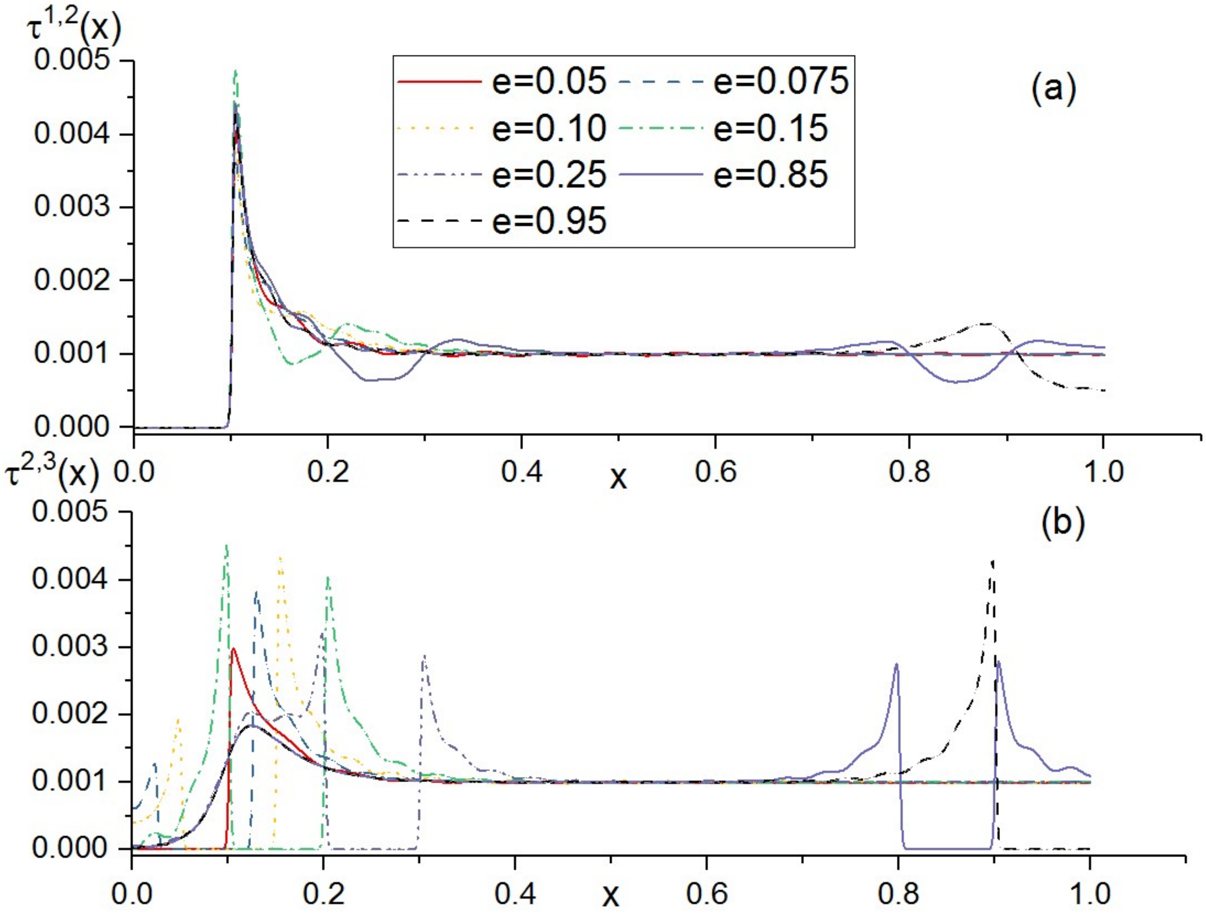

Fig.5.33 Traction distribution (S-D-S, $S=0.001, h=0.01, a_0^{1,2}=0.1,\ a_0^{2,3}=0.05$)

The degree of stress concentration is directly related to complex questions such as whether or not all defects will propagate (generally not) and, if multiple defects propagate, what is the corresponding propagation sequence. A relatively simple initial study can be carried out by comparing the maximum cohesive traction under exactly the same loading for different geometries as shown in Fig.5.34.

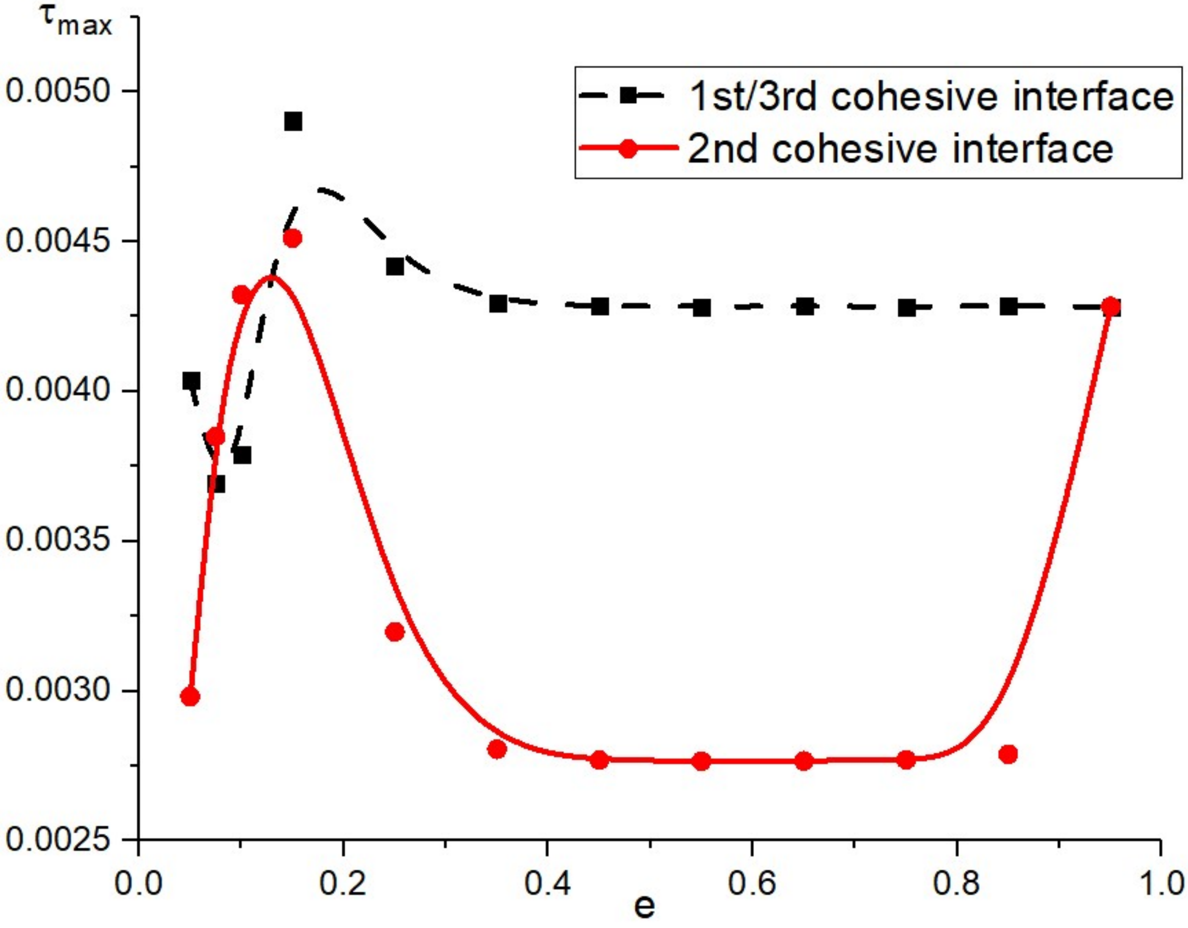

Fig.5.34 The cohesive surface maximum shear traction vs offset distance *e* (S-D-S, $S = 0.001, h = 0.01$)

Figure 5.34 shows the local stress concentration for different defect configurations. Except for the discussion of the special case that both cohesive surfaces have almost the same degree of stress concentration ($e = 0.95$, 2nd cohesive surface has edge defect), Fig.5.34 also provides other useful information. First, excluding the two special cases where e=0.075 or e=0.1, the curve of maximum stress of the 1st and 3rd cohesive surface is almost always on top of the corresponding second cohesive surface curve. This indicates that the 1st and 3rd cohesive surfaces have relatively higher traction concentration and therefore are more vulnerable to defect propagation as the applied load increases. The special cases of e=0.075 and e=0.1, where the maximum cohesive traction on second cohesive surface is higher than its counterpart on the other surfaces, can be explained by checking the second cohesive shear traction from other cases. For the case of e=0.05, the geometry is columnar and interlaminar crack shielding suppresses the traction concentration on 2nd cohesive surface. The next two groups of points correspond to the two special cases of e=0.075 and e=0.1. Note these two special cases have different traction distributions than the others shown in Fig.5.33, i.e., the outer tip of the 2nd cohesive surface has a higher traction concentration than that of the inner tip. Fig.5.35 shows how introducing a small bonded region affects the local stress concentration. Recall that for CZM, the local stress concentration can be explained from the global equilibrium point of view, compensating the deficit between applied load and reactive traction within defect region. Focusing on the primary defect tip (i.e., the defect tip with the stronger stress concentration, in this case at $x=0.125$), to the left of it is a small initially defective region ($0.025 \le x \le 0.125$) with zero shear traction. The difference between the "shear force" (integration of traction within certain region) within the initial defective region forms the main body of stress concentration at the primary defect tip (as single columnar model). To the left of the small defect region ($x \le 0.025$) is the inner bonded region. Within that region, take the applied load line ($S=0.0010$) as reference line, every point above is surplus while any point below is deficit. This clearly shows that within the inner bonded region, there is overall deficit which can only be compensated by raising the primary defect stress concentration. When e=0.15, the defect tip of 1st and 3rd cohesive surfaces line up with the inner defect of the 2nd cohesive surface. Interlaminar defect interaction elevates the traction concentration for both cohesive surfaces such that the most vulnerable case is observed with the highest traction values for all cohesive surfaces. For the other cases, the inner defect tip has a higher traction concentration within the 2nd cohesive surface. As the defect on the middle cohesive surface moves out towards the edge, defect interaction is negligible, and the solutions converge to stable behavior (horizontal line portion in Fig.5.34) regardless of a change in defect configuration.

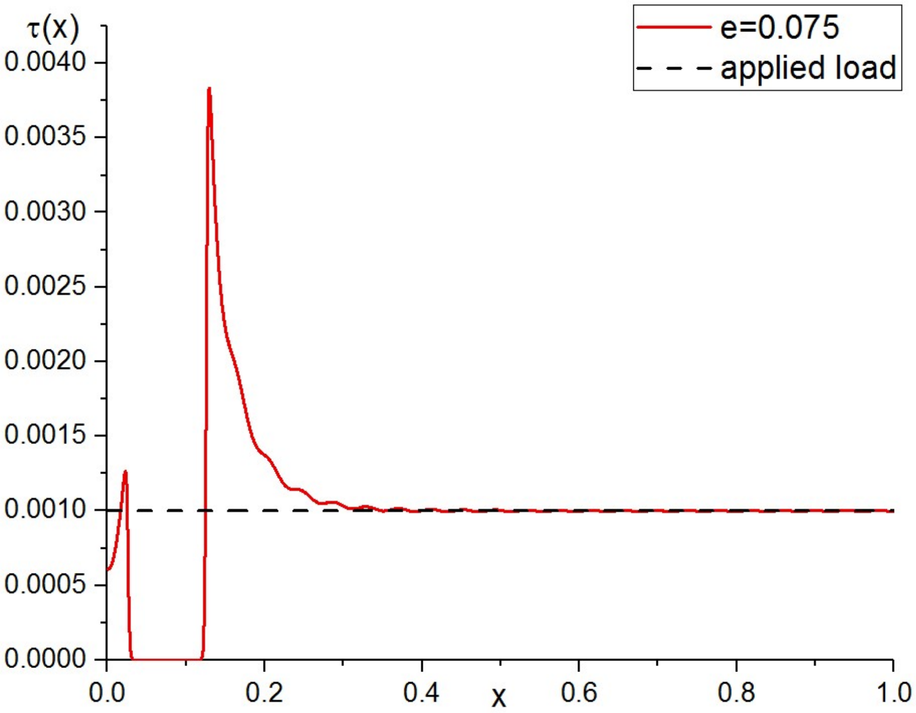

Fig.5.35 shear stress and applied load distribution.

However, determining the defect propagation process based simply on the stress concentration under relatively low loading has its limitations. First, not all cohesive surfaces have the same resistance to shear deformation, i.e., a multilayer composite system consists of multiple adhesive layers with different bonding strengths. Secondly, there is no guarantee that the basic pattern of the shear traction distribution would remain similar up to failure, i.e., more ductile cohesive surfaces fail like linear spring interfaces which resemble an interfacial softening. Under these circumstances, the study of defect propagation has to be done by computing and investigating stress fields up to failure. Figure 5.36 shows one example (e=0.1), assuming a relatively small applied load (S=0.001). From the solid curves, it can be concluded that the outer defect tip on the 2nd cohesive surface propagates first. In Fig.5.36, $S = 0.0056$ is the initiation load when the outer defect tip on the 2nd cohesive surface begins to propagate (as predicted by the simple argument above based on fields of S=0.001) whereas the value of the shear traction of inner tip is far from the cohesive strength. The cohesive shear of the defect tip on the 1st cohesive surface is close to the cohesive strength but has not propagated yet. The group of dash-dot lines (S=0.0070 ultimate load) shows that the defect on the 1st cohesive surface eventually will propagate but the inner defect on the 2nd cohesive surface will not.

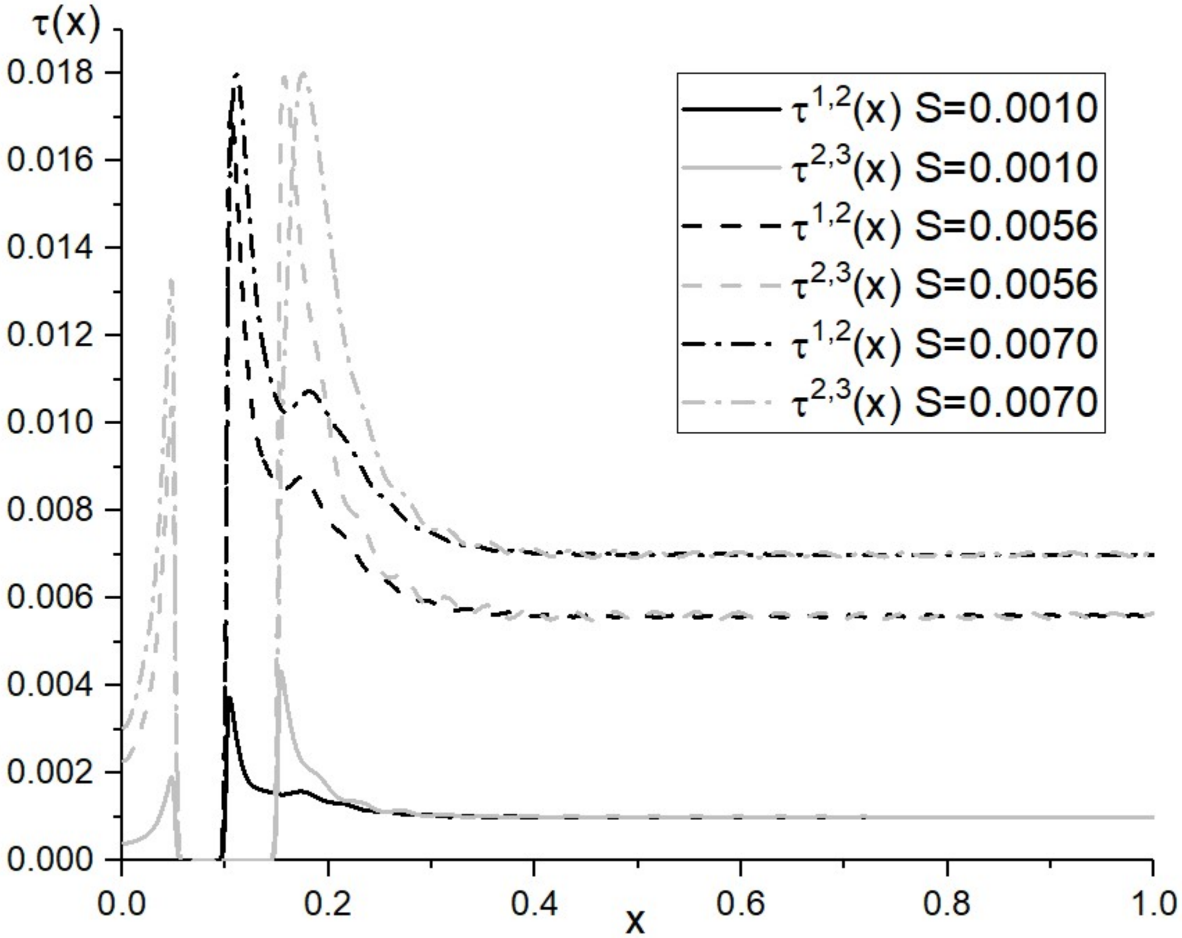

Fig.5.36 Interfacial shear distribution ($e=0.1, h=0.01, a_0^{1,2}=0.1,\ a_0^{2,3}=0.05$)

Another form of the diamond array pattern can be obtained by simply switching the stacking sequence as shown in Fig.5.37. A discussion of this case proceeds in a way that is parallel to that of the previous section.

Figure 5.38 shows the traction distribution for different offset distance e under the same applied load ($S = 0.0010$). The figure indicates that there are several differences as compared with Fig.5.33. First, for the cohesive surface with moving defect fronts, the case that $e = 0.05$ (single columnar defect geometry, left most point on Fig.5.34) has the second strongest traction concentration (second to edge defect geometry) rather than in the previous case in which several cases have stronger concentrations (Fig.5.33 bottom). Second, as the cohesive surface with a single defect tip has been moved to the middle in the thickness direction, none of its boundary is subjected to strong uniform shear traction. Instead, both of its boundaries are subject to nonuniform cohesive shear traction and the stress oscillation (the wiggle) is strengthened since both boundaries of the cohesive surface are perturbed by the introduction of defects.

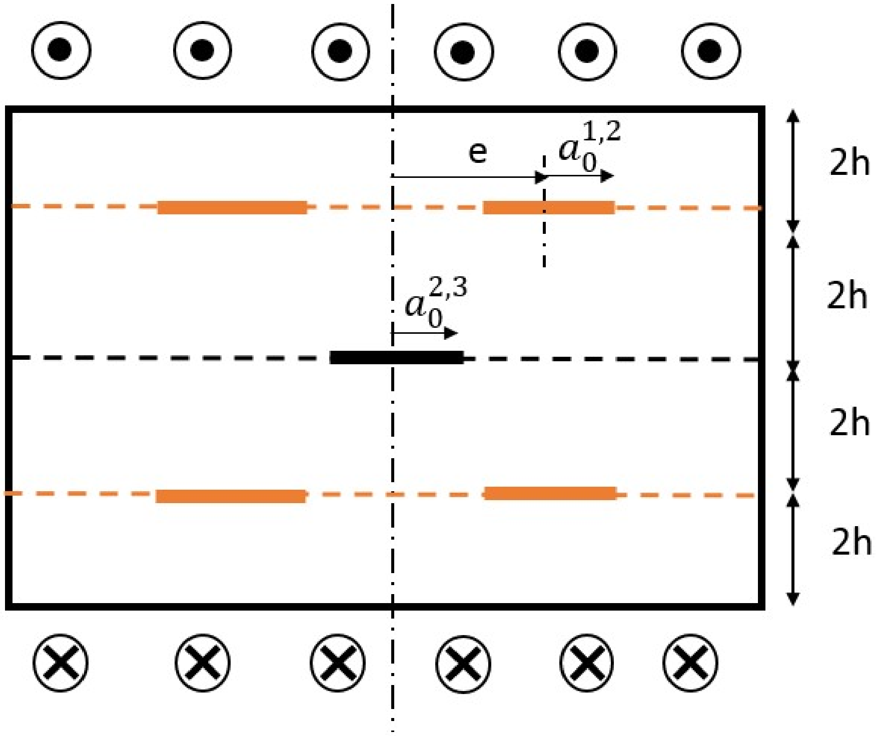

Fig.5.37 Schematic sketch for a double-single-double (D-S-D) diamond array of defects.

Comparing Fig.5.34 with Fig.5.39, one can readily draw the conclusion that when defect tips are well separated ($e \geq 0.35$), regardless of the defect pattern, the general cohesive surface behavior converges such that the cohesive traction distribution mainly depends on the size of defects (the cohesive surface with a single defect has a stronger traction concentration and would fail first) since defect interaction can be neglected. However, for cases where the offset distance is relatively small, the cohesive surface behavior should be studied by keeping track of the traction field for each step.

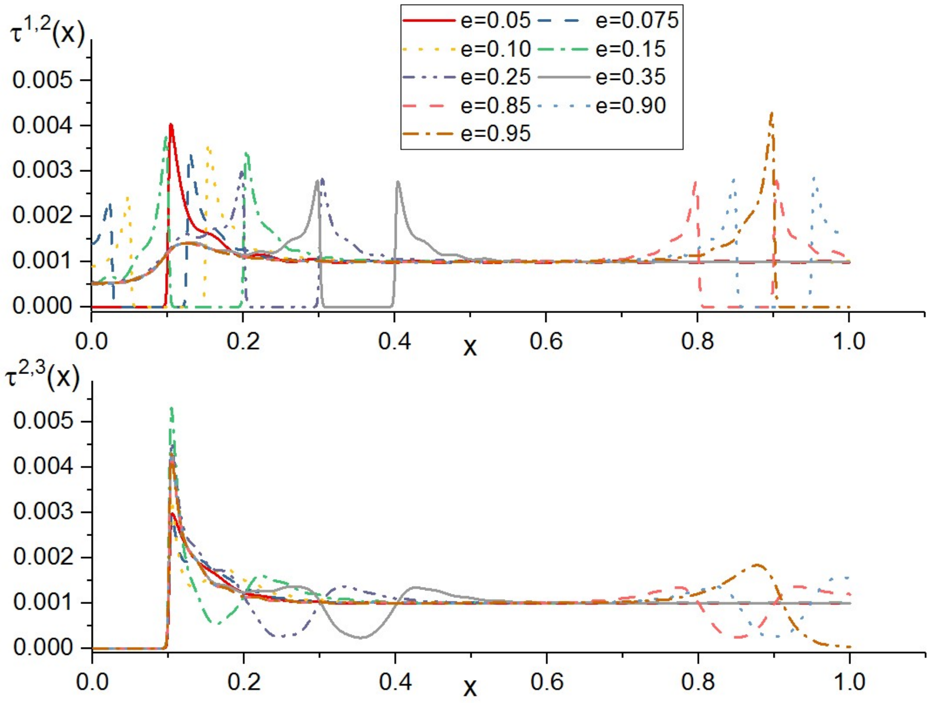

Fig.5.38 Traction distribution (D-S-D, $S = 0.001, h = 0.01, a_0^{1,2} = 0.05, a_0^{2,3} = 0.1$)

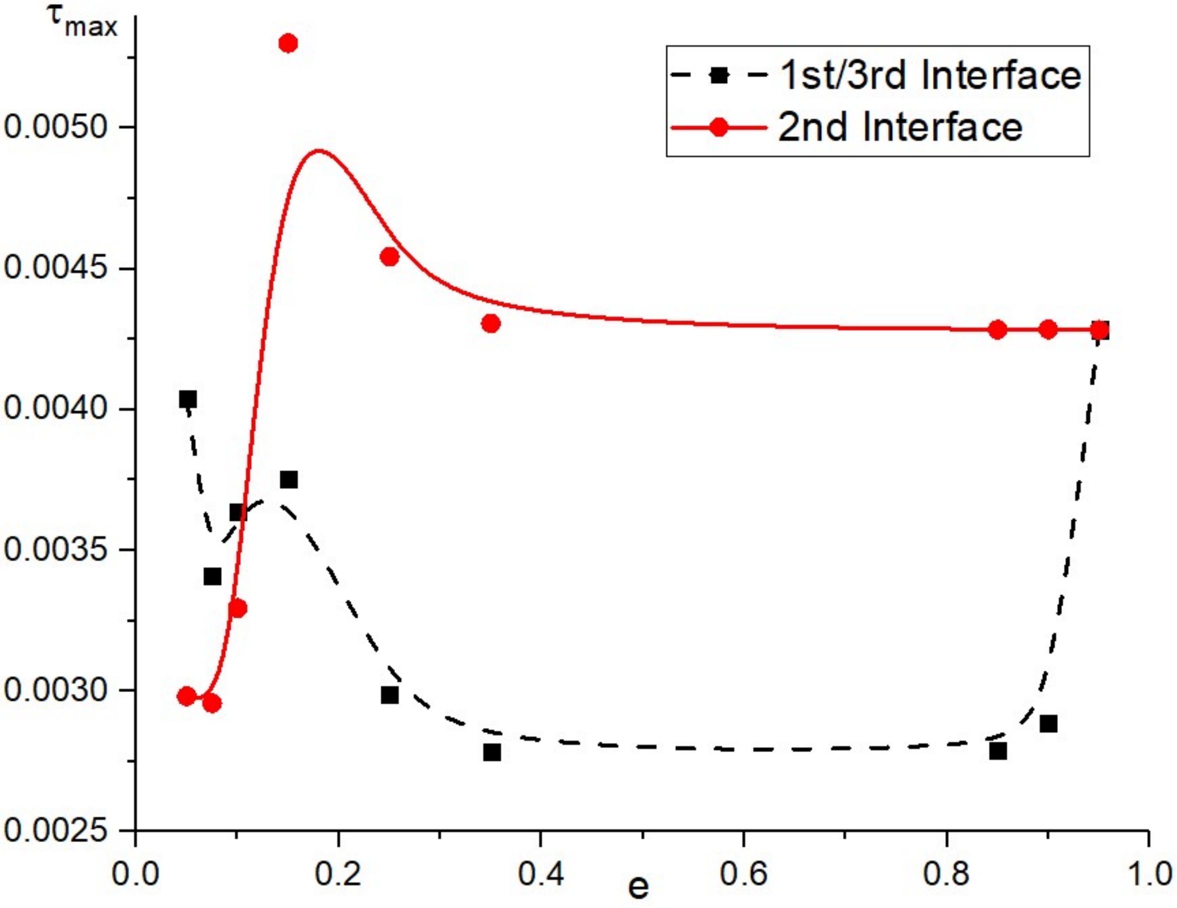

Fig.5.39 The interfacial maximum shear stress vs offset distance e (D-S-D, $S = 0.001, h = 0.01$)

It is worth pointing out that under certain circumstances, the two basic configurations of the diamond array degenerate to a single one. Similar to the argument made about Fig.4.12, due to perfect symmetry, the central plane is stress free. Then the boundary conditions of the right half of Fig.5.40a is exactly the same as left half of Fig.5.40b and, based on the uniqueness theorem of linear elasticity [110], so is the stress and deformation field. Based on above argument, Fig.5.40 shows two defect geometries that look different but are mathematically equivalent. Their solution can be obtained by solving one model and translating the coordinate system accordingly.

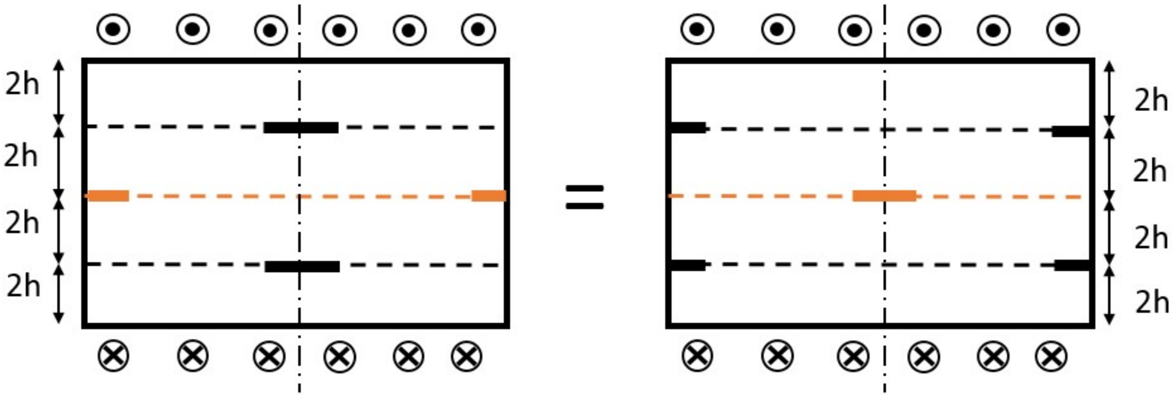

Fig.5.40 Equivalence of diamond pattern configurations.

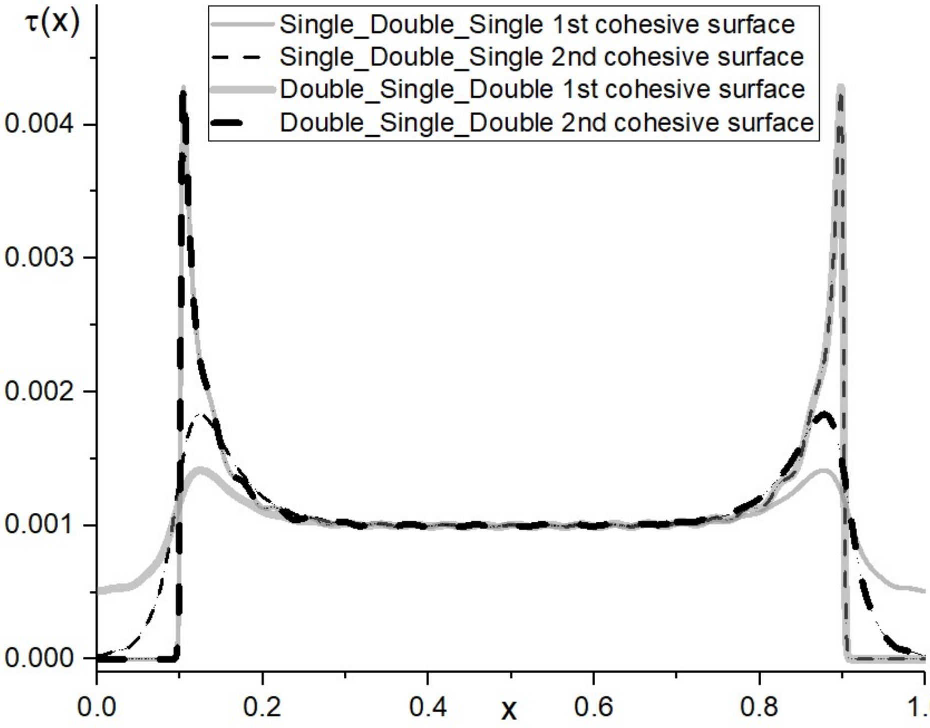

Fig.5.41 Traction field for defect geometry in Fig.5.40. $S = 0.0010$.

Figure 5.41 shows that a full cohesive fracture analysis (not taking the above argument into consideration) verifies the prediction. The lines with the same line shape represent the equivalent defective cohesive surface, the two configurations have exactly the same traction distribution as long as the *x*-axis is translated as stated. For a system with a periodicity condition in the *x*-

coordinate direction, the argument above can be used to simplify the calculation by scaling a sub-problem to a simpler geometry.

6 Conclusions

This dissertation has been concerned with the fundamental mechanical behavior of mode-III cohesive fracture in two basic geometries, the long slender cylindrical bar and the N-sublayer system subject to anti-plane loading. To circumvent the restriction from LEFM (simple defect geometries) and testing (difficulties in getting pure mode-III fracture), a general theory has been developed beginning with the exact solution to the equations of linear elasticity and proceeding with an integral equation formulation for the two pure mode-III cohesive fracture problems. Superior to the LEFM solution whose application is limited by crack tip plasticity and the unphysical crack tip stress singularity, the theory developed in this study takes advantage of both conciseness (exact behavior describable as a low order set of nonlinear integral equations) and flexibility (it can be implemented with to a wide range of cohesive force laws).

The first geometry considered in the study (Section 3) focuses on the cohesive fracture of a long slender cylinder containing an axisymmetric defect on a cross section. The governing equations are in the form of nonlinear integral equations that takes full consideration of the displacement field (including rigid body displacement). In this dissertation, a novel computational method based on the Newton Raphson (NR) method has been employed to solve the integral equations. The method reduces the equations to a finite set of nonlinear algebraic equations which can be truncated and solved depending on the precision needed.

Figure 3.3 and 3.6 shows that both uniform and the defective cohesive surfaces go through a similar interfacial stability behavior such that a critical load separates a stable (increasing slip under increasing load) and unstable (increasing slip under decreasing load) branch. However, a more brittle cohesive surface is more susceptible to the introduction of defects which is manifested by a more significant drop in critical load compared to the corresponding uniform cohesive surface.

The slip and traction fields for different cohesive surface ductilities and defect geometries are plotted in Fig.3.7-8 (center defect) and Fig.3.11-12 (edge defect). As expected, ductile cohesive surfaces have a more distributed field whereas brittle ones have more a concentrated local field. Within the regime in which they are comparable (stiff cohesive surface under small loading), the solution is in excellent agreement with LEFM solutions in the neighborhood of the crack tip. The nature of cohesive fracture solutions enables the modelling of brittle and ductile defect growth within the same framework and, can account for defect interaction. This fact motivates the study of cohesive surfaces with multiple defect fronts. Figure.3.14 shows that CFS compares well with SCS when the defect tips are well separated. However, when the two defect tips are close or the domain is finite, CFS is more accurate. This is because SCS neglects crack interaction and is largely based on an infinite or semi-infinite domain which neglects boundary effects. Because the history of the traction field under monotonically increasing load is computed, the implementation of certain stress-based defect propagation criteria can be used to predict the defect propagation process. Figure.3.9 shows the difference between a brittle and a ductile cohesive surface for the same single defect geometry, i.e., the differences between defect driven behavior as opposed to compliant “linear spring” type behavior. For cohesive surfaces with multiple defect tips, a direct extension is the comparison of propagation behavior between tips. This includes addressing the question of defect tip propagation sequence and its relationship to cohesive surface stability. Figure.3.15 shows defect tip locations vs applied load for several cases, each of which has 0.1 width of annular bonded region but at different radial locations. Figure.3.15 clearly shows that the inner tip resists propagation since it bears a lower traction (recall the classic linear stress distribution for a cylinder under torsional loading [101]). As the bonded region moves radially outward, the inner tip may start to propagate but it will still occur later and be shorter of length than the outer defect.

The flexibility of the cohesive constitutive relation enables the study of more complicated behavior such as a materially nonuniform bi-cylinder and frictional cohesive surfaces. Figure.3.16 shows that a materially nonuniform bi-cylinder has similar stability behavior as the uniform cylinder. However, the introduction of a new bulk material makes the corresponding material properties come into effect. Under such circumstances, reducing the shear moduli of one of the cylinders will soften the system leading to a reduction in critical load. The orientation of mode-I micro cracks can be predicted by studying the traction field along the cohesive surface. Depending on the relative magnitude between the two traction components, the potential orientation of mode-I micro crack plane (which is perpendicular to the principal tensile stress direction) varies from 90 degrees (behind the primary defect tip) to 45 degrees (ahead of primary defect tip). Frictional response can be coupled with the cohesive response by superimposing a friction law to the cohesive relation. By tuning the relative magnitude of the cohesive and the frictional response two qualitatively different behaviors can be observed. The stability response of the decohesion dominated case is similar to previous results but with a nonvanishing reactive traction. In contrast, the friction dominated case no longer has a critical load since decohesion softening response is followed by significant frictional response.

The second geometry considered in this dissertation (Section 4) deals with the two-sublayer composite system. The development parallels that of the cylinder analysis, i.e., nonlinear integral equations are derived from the exact elasticity solution of a single sublayer subject to arbitrary but equilibrated shear tractions on top and bottom surfaces. The main difference is that unlike the cylinder analysis which requires the cylinder to be semi-infinite (or long enough so that weak boundary conditions can be prescribed on the ends), the sublayer solution is obtained for finite layer thicknesses with strong boundary conditions applied to all surfaces. In Fig.4.3, it has been demonstrated that the uniform cohesive surface should have a uniform traction distribution and therefore, the stability analysis of the two-sublayer system can be obtained simply by inversing the cohesive force law. For the two-sublayer system with nonuniform cohesive surface (i.e., one with initial defects), the study parallels that of the cylinder geometry and they share many similarities. The cohesive surface stability behavior is similar to the cylinder geometry which consists of a stable and an unstable branch separated by a load maximum. The single defect near tip stress field also shows consistency with SCS, multiple defect stress fields give a more reasonable prediction with defect interaction effects included. CFS of periodic defect geometries show consistency with existing SCS, both of which gives the same amount of stress concentration for each defect tip. By changing the defect spacing, size and location, general conclusions regarding intralaminar defect interaction can be drawn. Closely located defect tips, tips of larger defects and tips close to free boundaries have stronger stress concentrations. The solution can be applied to study subsurface defects situated in a materially nonuniform bilayer in which a stiffer or thicker coating layer leads to a reduced stress concentration. Other topics such as defect propagation processes, the orientation of mode-I micro cracks and frictional cohesive surfaces are basically the same as for the cylinder case.

The third geometry considered, i.e., the N-sublayer system (Section 5) is a direct extension of the two-sublayer system considered in Section 4. Based on the exact solution for the uniform cohesive surface, a stability analysis of an N-sublayer system can be carried out in a similar fashion to the two-sublayer systems but leads to more complicated results as shown in Fig.5.3-5. This includes the configuration transition from simple shear deformation (shearing of a deck of card) to an asymmetric configuration (when interlaminar cohesive strength perturbations exist). The cause of this behavior comes from imperfections of the system, e.g., perturbations of cohesive strength between different cohesive surfaces. The transition from an initial symmetric configuration to an asymmetric configuration can be obtained by either an abrupt snap-type transition (brittle) or a smooth transition (ductile). However, the stability analysis of systems with nonuniform cohesive surface needs to be done by full CFS analysis with perturbations to trigger a certain configuration (solving a set of nonlinear integral equations) rather than inversing the cohesive force law.

Section 5.3 focusses on interlaminar defect interaction of a tri-sublayer system. The conclusions that can be drawn are as follows, i) for a single-single defect geometry (each cohesive surface has only one defect situated in the middle, shown in Fig.5.10) with same defect size, reducing the middle sublayer thickness (closely located defects in thickness direction) leads to a reduction of stress concentration, ii) keeping the sublayer thicknesses relatively thin and fixed, changing one of the defect sizes would greatly change the stress pattern. If the offset distance between the defect tip on 1st and 2nd cohesive surface is relatively small, the larger defect will be affected by the concentrated tip stress of its counterpart. Whereas the smaller defect is encircled by the larger defect, its stress concentration is reduced. A similar argument is also valid for double-single (the 1st cohesive surface has two defects of the same size situated symmetrically, and the 2nd cohesive surface has only one defect, shown in Fig.5.14) defect geometry. The relative tip location and boundary condition has a strong effect on the stress redistribution. It is worth pointing out that this dissertation also discussed the possibility of diminishing the small inner bonded region. In such cases, the CFS model could be used to predict single defect propagation, defect coalescence and subsequent growth within the same framework.

The four-sublayer geometry was considered in order to study a multi-sublayer system with thickness direction symmetry (columnar or diamond pattern of defects). For a single column of defects, the study has made a comparison with that of the tri-sublayer system such that the effect of introducing a new defect surface (interlaminar crack shielding) is observed. However, this is an ideal scenario because the newly introduced defect is exactly the same as the other. The effect of the size of the newly introduced defect is given in Fig.5.21-23, the discussion includes local traction concentration, cohesive surface traction fields and defect propagation sequences. It’s worth pointing out that under two circumstances, the multiple defect column geometry can be reduced to a single column of defects approximately or exactly, i) defect tips are well separated (approximately) or ii) a certain periodic condition is satisfied (exactly). The four-sublayer system is used to study geometries with both interlaminar symmetry and defect tip offsets. The effects of geometries on local stress concentration is shown in Fig.5.34 and Fig.5.39 for two different types of diamond patterns. The explanation for the behavior is obtained by examining the stress distributions shown in Fig.5.33 and Fig.5.38. Two types of diamond pattern can be equivalent under certain circumstances, the criteria and computational proof required for this to be true is also presented.

This dissertation extends existing cohesive fracture analyses, that have been used to study the debonding of inclusions and the planar delamination of layered composites, to the realm of mode-III cohesive fracture. The two geometries considered are the torqued cylinder and the N-sublayer composite. The advantage of the methodology includes the mathematical clarity of an analytical solution, fully account for rigid body displacement, the versatility of being able to employ different cohesive relations that can be used to characterize different response, no unphysical stress singularity, a full field description which takes defect interaction and boundary effects into consideration automatically, etc. However, there are limitations and drawbacks that may have room for improvement. First, the geometry has certain limitations. The sublayer system and cylinder geometry need to be long enough to ensure that the weak boundary condition has no effect on the cohesive surface. Second, due to difficulties in mode-III testing, the characterization of pure mode-III cohesive law is rather difficult. Without efficient and accurate testing methodologies characterizing the cohesive force law, the theory developed here can only provide insights into the qualitative behavior rather than give quantitative information for a real engineering problem. It also needs to be mentioned that the analytical methodology is rather efficient in handling simple defect geometries. However, for more complicated defect geometries with characteristic lengths of the geometry decreasing, the fields require higher order terms to capture reasonable behavior. The increasing computational burden and precision needed also slows down the convergence rate of CFS. In such case, CFS loses some of its advantages over FEA.

7 Future Work

The method developed in this study has two important elements that differentiate the various problems which can be solved by it. The first, is that the solution of the displacement field of a component sub-problem should be obtainable as an expansion in eigenfunctions. The component sub-problem can be defined as that part of the solid body of interest that lies on one side of the surface/interface on which the defect is presumed to propagate. Arbitrary but equilibrated surface/interface tractions are assumed to be prescribed pointwise. The other element is that a cohesive force law connects two or more sub-problems and, governs the cohesive surface behavior. In this section these two key elements are examined in order to provide a brief overview of some other problems that can be explored by the method applied in this dissertation.

Note that the solution to a component sub-problem consisting of an elastic solid subject to equilibrated but otherwise arbitrary strong traction boundary conditions is very difficult to obtain. Figure 7.1 shows an example of a pressure vessel with two symmetric inner cracks and the corresponding component sub-problem that would be required to be solved. The system can be reduced to analyzing a quarter circular domain subject to mixed boundary conditions. The boundary condition of the inner and outer circular surface is relatively simple, i.e., the inner surface is subject to applied pressure and the outer surface is traction free. However, the boundary conditions of the two imaginary radial cuts are complicated. Symmetry considerations force those two surfaces to be free of shear traction and to have zero circumferential displacement ($\sigma_{\theta r} = 0,\ u_\theta = 0$ at $\theta = 0, \pi/2$). The traction on the defect plane is assumed arbitrary in the formulation process and can only be obtained by numerical computation procedure. Due to Saint-Venant's Principle, traction on the vertical plane is unknown but can be approximated by the similar geometry without defects. Note that the pure mode-III problems presented in this dissertation are unidirectional in both the deformation field and the cohesive relation. The example shown in Fig.7.1 has two deformation components (u_θ and u_r) but only a single component of cohesive traction is needed since the unknown traction and deformation fields are unidirectional on the cohesive surface. More general problems with multi-directional deformation fields and mixed-mode fracture processes such as mode-I/II coupled fracture of layered systems, can be studied in a similar manner but with more complicated mixed-mode cohesive relations. Related work on this problem can be found in [78], [79], [80].

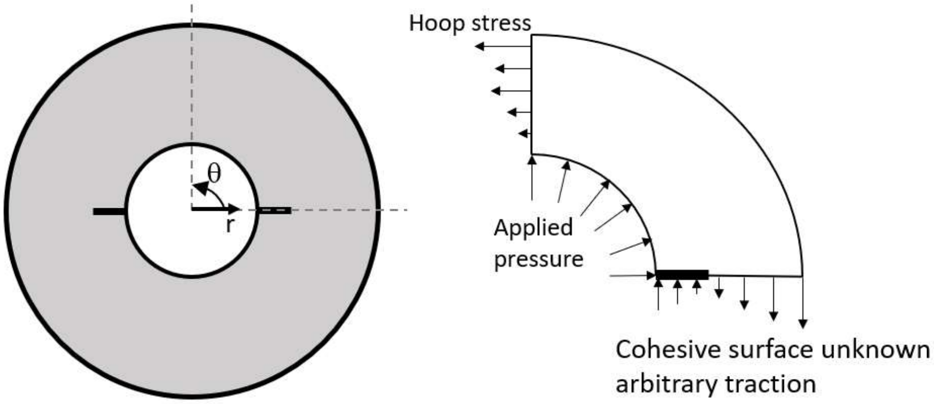

Fig.7.1 Schematic figure of sub-problem of a cracked pressure vessel.

An interesting direct extension of the current study with a more complicated deformation field, is the cohesive fracture of a notched cylinder subject to mode-I/III loading as shown in Fig.7.2.

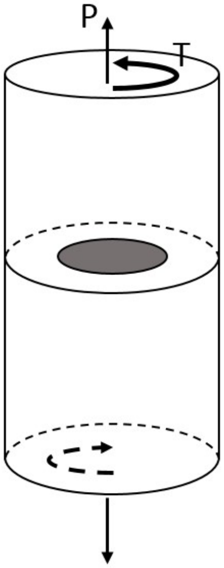

Fig.7.2 Schematic figure of notched cylinder subjects to mode-I/III loading.

This geometry has been utilized in testing and results indicate two different kinds of fracture processes with different primary fracture planes, i.e., spiral and flat [30], [31]. It has been demonstrated that whether or not the one or the other occurs depends upon the loading (or equivalently the mode-mixity) and the geometry (depth of initial defect, shape and sharpness of notch). However, the quantitative study of the transition between the two primary fracture propagation modes can be analyzed by a comprehensive parametric study of the mathematical analysis proposed in this study. Even though the mode-I fracture testing of a cylindrical bar is very common in industry, it is worth pointing out that extra attentions should be given to the cohesive fracture formulation. This is because nonuniform normal traction on the cohesive surface leads to additional displacement in the radial direction due to Poisson's effect and, a mixed-mode (mode-I/II) cohesive force law is needed for characterizing the cohesive surface.

Another popular topic related to mode-III layered geometries is the wrinkling of materially nonuniform composites subject to compressive loading. Note that the current work on wrinkling problems is mostly global wrinkling and assumes that the rigid coating and soft substrate are ideally bonded as shown in the top figure of Fig.7.3. Some researchers have proposed applying CZM and Föppl-von Kármán plate theory [124] to study the transition from wrinkling to buckle-delamination as shown in Fig.7.3. However, the equations of Föppl-von Kármán plate theory are notoriously difficult to solve, and it is an idealized 2D model. In order to study local wrinkle and buckle-delamination that is likely to be triggered by local defects, analytical solutions to the layered system under mode-I/III loading should be developed. Wrinkling can be induced by adding perturbation of the cohesive surface, the effect of local defects and the formation process from wrinkle to delamination can be obtained. The theory applied in this dissertation may be applicable to analysis of incipient wrinkling by adding an additional displacement component and introducing mixed-mode cohesive force laws.

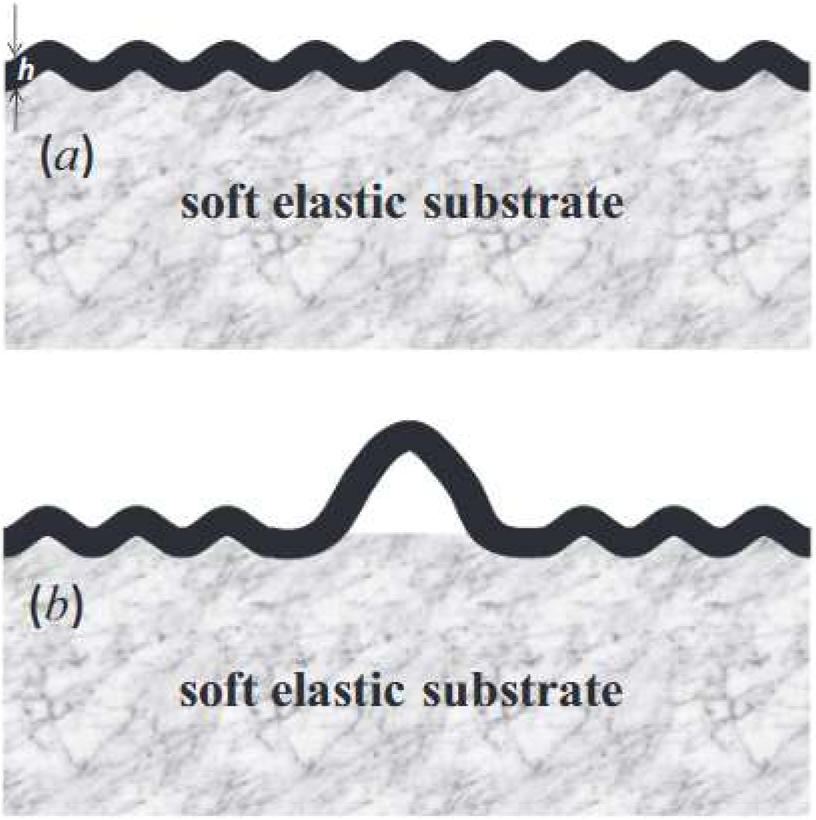

Fig.7.3 Materially nonuniform bi-layer, wrinkle to delamination transition [125].

For the same geometry and response, the methodology applied in the study is largely independent of the cohesive law and in this dissertation three have been used, i.e., piecewise linear, exponential, and modified exponential. These interface constitutive models are relatively simple in the way that they are reversible, modified exponential with friction is dissipative and can only be applied to problems related to monotonic loading. By examining other cohesive laws, the solution can be used to study more complicated processes such as cyclic loading. Modification to cohesive laws has to be made such that they can capture complicated material response for loading, unloading and cyclic procedures. Extensive development of cohesive laws has been carried out, most of this work is based on hysteretic model to capture irreversible dissipative process as [126], [127], [128]. The methodology developed in this dissertation, incorporating cohesive relations (that captures cyclic response), can be a powerful tool for studying interfacial stability analysis under cyclic loading.

References:

[1] Sun, C. and Jin, Z. (2012). *Fracture mechanics*. Waltham, MA: Academic Press.

[2] Aliha, M., Bahmani, A. and Akhondi, S. (2015). Determination of mode III fracture toughness for different materials using a new designed test configuration. *Materials & Design*, 86, pp.863-871.

[3] En.wikipedia.org. (2018). Fracture mechanics. [online] Available at: https://en.wikipedia.org/wiki/Fracture_mechanics#/media/File:Fracture_modes_v2.svg [Accessed 10 Jan. 2018].

[4] G.I. Barenblatt, The Mathematical Theory of Equilibrium Cracks in Brittle Fracture, *Advances in Applied Mechanics*, Volume 7, 1962, Pages 55-129, ISSN 0065-2156

[5] Dugdale, D. (1960). Yielding of steel sheets containing slits. *Journal of the Mechanics and Physics of Solids*, 8(2), pp.100-104.

[6] Muskhelishvili, N. (2010). *Some basic problems of the mathematical theory of elasticity*. Leyden: Noordhoff.

[7] Sneddon, I. (1979). *The use of integral transforms*. New Delhi: TATA McGraw-Hill.

[8] Hills, D. (2010). *Solution of crack problems*. Dordrecht: Springer.

[9] Sih, G. and Benthem, J. (1973). *Methods of analysis and solutions of crack problems*. Leyden: Noordhoff International Publishing.

[10] Sneddon, I. and Lowengrub, M. (1969). *Crack problems in the classical theory of elasticity* [by] I.N. Sneddon [and] M. Lowengrub. New York: Wiley.

[11] Bakr, A. and Fenner, R. (1983). Use of the Hankel transform in boundary integral methods for axisymmetric problems. *International Journal for Numerical Methods in Engineering*, 19(12), pp.1765-1769.

[12] Tricomi, F. (2012). *Integral Equations*. Newburyport: Dover Publications.

[13] Erdogan, F. (1983). Stress Intensity Factors. *Journal of Applied Mechanics*, 50(4b), p.992.

[14] Sih, G. (1973). *Handbook of stress-intensity factors*. Bethlehem, Pa.: Lehigh Univ., Inst. of Fracture and Solid Mechanics.

[15] Shlyannikov, V. (2016). Nonlinear stress intensity factors in fracture mechanics and their applications. *Procedia Structural Integrity*, *2*, 744-752. doi: 10.1016/j.prostr.2016.06.096

[16] Rice, J. and Sih, G. (1965). Plane Problems of Cracks in Dissimilar Media. *Journal of Applied Mechanics*, 32(2), p.418.

[17] Erdogan, F. (1963). Stress Distribution in a Nonhomogeneous Elastic Plane With Cracks. *Journal of Applied Mechanics*, 30(2), p.232.

[18] Hutchinson, J., Mear, M. and Rice, J. (1987). Crack Paralleling an Interface Between Dissimilar Materials. *Journal of Applied Mechanics*, 54(4), p.828.

[19] Chien-Ching, M. and Bao-Luh, H. (1990). Antiplane problems in composite anisotropic materials with an inclined crack terminating at a bimaterial interface. *International Journal of Solids and Structures*, 26(12), pp.1387-1400.

[20] Wu, K. and Chiu, Y. (1991). Antiplane Shear Interface Cracks in Anisotropic Bimaterials. *Journal of Applied Mechanics*, 58(2), p.399.

[21] Jiun-Der, Y. and Kuang-Chong, W. (1993). Anti-plane shear crack in a sandwich composite. *Engineering Fracture Mechanics*, 44(6), pp.875-885.

[22] Matallah, M. and La Borderie, C. (2009). Inelasticity–damage-based model for numerical modeling of concrete cracking. *Engineering Fracture Mechanics*, 76(8), pp.1087-1108.

[23] Long, R., Krishnan, V. and Hui, C. (2011). Finite strain analysis of crack tip fields in incompressible hyperelastic solids loaded in plane stress. *Journal of the Mechanics and Physics of Solids*, 59(3), pp.672-695.

[24] Allegri, G. and Scarpa, F. (2014). On the asymptotic crack-tip stress fields in nonlocal orthotropic elasticity. *International Journal of Solids and Structures*, 51(2), pp.504-515.

[25] Khoshravan, M. and Moslemi, M. (2014). Investigation on mode III interlaminar fracture of glass/epoxy laminates using a modified split cantilever beam test. *Engineering Fracture Mechanics*, 127, pp.267-279.

[26] Yangyang Ge, Xiaojing Gong, Anita Hurez, Emmanuel De Luycker. Test methods for measuring pure mode III delamination toughness of composite. *Polymer Testing*, Elsevier, 2016, 55, pp.261-268.

[27] Berto, F., Elices, M., Lazzarin, P. and Zappalorto, M. (2012). Fracture behaviour of notched round bars made of PMMA subjected to torsion at room temperature. *Engineering Fracture Mechanics*, 90, pp.143-160.

[28] Neuber, H. (1961). Theory of Stress Concentration for Shear-Strained Prismatical Bodies With Arbitrary Nonlinear Stress-Strain Law. *Journal of Applied Mechanics*, 28(4), p.544.

[29] Berto, F. and Lazzarin, P. (2009). The volume-based Strain Energy Density approach applied to static and fatigue strength assessments of notched and welded structures. *Procedia Engineering*, 1(1), pp.155-158.

[30] Mitchell, D., Makabe, C., Anggit, M., Sueyoshi, T. and Yafuso, T. (2006). The Formation Mechanism of the Factory-Roof Pattern in a Torsional Fatigue Specimen with Circumferential Notch. *Journal of Testing and Evaluation*, 34(5), p.100101.

[31] Yu, G., Gao, X. and Song, Y. (2017). Experimental investigation of the tension-torsion coupling behavior on needled unidirectional C/SiC composites. *Materials Science and Engineering*: A, 696, pp.190-197.

[32] Zehnder, A. and Zella, N. (2015). Spiral to flat fracture transition for notched rods under torsional loading. *International Journal of Fracture*, 195(1-2), pp.87-92.

[33] Cox, S. and Scholz, C. (1988). On the formation and growth of faults: an experimental study. *Journal of Structural Geology*, 10(4), pp.413-430.

[34] Mitchell, D., Makabe, C., Anggit, M., Sueyoshi, T. and Yafuso, T. (2006). The Formation Mechanism of the Factory-Roof Pattern in a Torsional Fatigue Specimen with Circumferential Notch. *Journal of Testing and Evaluation*, 34(5), p.100101.

[35] Horner, A., Czabaj, M., Davidson, B. and Ratcliffe, J. (2015). Three-dimensional crack surface evolution in mode III delamination toughness tests. *Engineering Fracture Mechanics*, 149, pp.313-325.

[36] Ritchie, R., McClintock, F., Nayeb-Hashemi, H. and Ritter, M. (1982). Mode III fatigue crack propagation in low alloy steel. *Metallurgical Transactions* A, 13(1), pp.101-110.

[37] Czabaj, M., Ratcliffe, J. and Davidson, B. (2014). Observation of intralaminar cracking in the edge crack torsion specimen. *Engineering Fracture Mechanics*, 120, pp.1-14.

[38] Yoshihara, H. (2006). Examination of the 4-ENF test for measuring the mode III R-curve of wood. *Engineering Fracture Mechanics*, 73(1), pp.42-63.

[39] Leung, A. and Su, R. (1995). Mixed-mode two-dimensional crack problem by fractal two level finite element method. *Engineering Fracture Mechanics*, 51(6), pp.889-895.

[40] Needleman, A. (1990). An analysis of decohesion along an imperfect interface. *International Journal of Fracture*, 42(1), pp.21-40.

[41] Park, K., Paulino, G. and Roesler, J. (2009). A unified potential-based cohesive model of mixed-mode fracture. *Journal of the Mechanics and Physics of Solids*, 57(6), pp.891-908.

[42] Park, K. and Paulino, G. (2013). Cohesive Zone Models: A Critical Review of Traction-Separation Relationships Across Fracture Surfaces. *Applied Mechanics Reviews*, 64(6), p.060802.

[43] Abanto-Bueno, J., & Lambros, J. (2005). Experimental determination of cohesive failure properties of a photodegradable copolymer. *Experimental Mechanics*, *45*(2), 144-152. doi: 10.1007/bf02428187

[44] Choi†, S., & Kim, K. (2007). Nanoscale planar field projections of atomic decohesion and slip in crystalline solids. Part I. A crack-tip cohesive zone. *Philosophical Magazine*, *87*(12), 1889-1919. doi: 10.1080/14786430601110372

[45] Jung Lee, M., Min Cho, T., Seock Kim, W., Chai Lee, B., & Ju Lee, J. (2010). Determination of

cohesive parameters for a mixed-mode cohesive zone model. *International Journal Of Adhesion And Adhesives*, *30*(5), 322-328. doi: 10.1016/j.ijadhadh.2009.10.005

[46] Alfano, M., Furgiuele, F., Leonardi, A., Maletta, C., & Paulino, G. (2008). Mode I fracture of adhesive joints using tailored cohesive zone models. *International Journal Of Fracture*, *157*(1-2), 193-204. doi: 10.1007/s10704-008-9293-4

[47] Gustafson, P., & Waas, A. (2009). The influence of adhesive constitutive parameters in cohesive zone finite element models of adhesively bonded joints. *International Journal Of Solids And Structures*, *46*(10), 2201-2215. doi: 10.1016/j.ijsolstr.2008.11.016

[48] Donaldson, S. (1988). Mode III interlaminar fracture characterization of composite materials. *Composites Science And Technology*, *32*(3), 225-249. doi: 10.1016/0266-3538(88)90022-x

[49] Muthupandian, J., & Pradeep, K. (2018). Characterization of Exponential Cohesive Zone Model for Fracture Assessment of De-Bonded Composite Panels. *Applied Mechanics And Materials*, *877*, 436-445. doi: 10.4028/www.scientific.net/amm.877.436

[50] Tvergaard, V. and Hutchinson, J. (1993). The influence of plasticity on mixed mode interface toughness. *Journal of the Mechanics and Physics of Solids*, 41(6), pp.1119-1135.

[51] Needleman, A. (1987). A Continuum Model for Void Nucleation by Inclusion Debonding. *Journal of Applied Mechanics*, 54(3), p.525.

[52] Ferrante, J. and Smith, J. (1979). Theory of metallic adhesion. *Physical Review* B, 19(8), pp.3911-3920.

[53] Ferrante, J., Smith, J. and Rose, J. (1984). *Universal Binding Energy Relations in Metallic Adhesion*. MRS Proceedings, 40.

[54] Banerjea, A. and Smith, J. (1988). Origins of the universal binding-energy relation. *Physical Review* B, 37(12), pp.6632-6645.

[55] Bozzolo, G., Ferrante, J. and Smith, J. (1991). Universal behavior in ideal slip. *Scripta Metallurgica et Materialia*, 25(8), pp.1927-1931.

[56] Xu, X., & Needleman, A. (1994). Numerical simulations of fast crack growth in brittle solids. *Journal Of The Mechanics And Physics Of Solids*, *42*(9), 1397-1434. doi: 10.1016/0022-5096(94)90003-5

[57] Xu, X. and Needleman, A. (1993). Void nucleation by inclusion debonding in a crystal matrix. *Modelling and Simulation in Materials Science and Engineering*, 1(2), pp.111-132.

[58] Raous, M., Cangémi, L. and Cocu, M. (1999). A consistent model coupling adhesion, friction, and unilateral contact. *Computer Methods in Applied Mechanics and Engineering*, 177(3-4), pp.383-399.

[59] Raous, M., Schryve, M., Cocou, M., 2006. Restorable adhesion and friction, in: Nonsmooth/Nonconvex Mechanics with Applications in Engineering, Baniotopoulos (Ed.), Ziti

Publisher, Thessaloniki, 165-172.

[60] Tvergaard, V. (1990). Effect of fibre debonding in a whisker-reinforced metal. *Materials Science and Engineering*: A, 125(2), pp.203-213.

[61] Chaboche, J., Girard, R. and Schaff, A. (1997). Numerical analysis of composite systems by using interphase/interface models. *Computational Mechanics*, 20(1-2), pp.3-11.

[62] Raous, M. (2011). Interface models coupling adhesion and friction. *Comptes Rendus Mécanique,* 339(7-8), pp.491-501

[63] Liu, P., Gu, Z. and Peng, X. (2016). A nonlinear cohesive/friction coupled model for shear induced delamination of adhesive composite joint. *International Journal of Fracture*, 199(2), pp.135-156.

[64] Jin, Z. and Sun, C. (2006). A comparison of cohesive zone modeling and classical fracture mechanics based on near tip stress field. *International Journal of Solids and Structures*, 43(5), pp.1047-1060.

[65] Needleman, A. (1990). An analysis of tensile decohesion along an interface. *Journal of the Mechanics and Physics of Solids*, 38(3), pp.289-324.

[66] Tvergaard, V. and Hutchinson, J. (1993). The influence of plasticity on mixed mode interface toughness. *Journal of the Mechanics and Physics of Solids*, 41(6), pp.1119-1135.

[67] Tabaković, A., Karač, A., Ivanković, A., Gibney, A., McNally, C. and Gilchrist, M. (2010). Modelling the quasi-static behaviour of bituminous material using a cohesive zone model. *Engineering Fracture Mechanics*, 77(13), pp.2403-2418.

[68] Xu, X. and Needleman, A. (1994). Numerical simulations of fast crack growth in brittle solids. *Journal of the Mechanics and Physics of Solids*, 42(9), pp.1397-1434.

[69] Zhang, Z. and Paulino, G. (2005). Cohesive zone modeling of dynamic failure in homogeneous and functionally graded materials. *International Journal of Plasticity*, 21(6), pp.1195-1254.

[70] Q.D. Yang, M.D. ThoulessMixed-mode fracture analyses of plastically-deforming adhesive joints. *Int. J. Fract*., 110 (2) (2001), pp. 175-187

[71] Geißler, G. and Kaliske, M. (2010). Time-dependent cohesive zone modelling for discrete fracture simulation. *Engineering Fracture Mechanics*, 77(1), pp.153-169.

[72] Kanninen, M.F. , 1973. An augmented double cantilever beam model for studying crack propagation and arrest. *Int. J. Fract*. 9 (1), 83–92 .

[73] Olsson, R. , 1992. A simplified improved beam analysis of the DCB specimen. *Com- pos. Sci*. Technol. 43 (4), 329–338 .

[74] Xu, W. and Waas, A. (2017). Multiple solutions in cohesive zone models of fracture. *Engineering Fracture Mechanics*, 177, pp.104-122.

[75] de Morais, A.B. , 2011. Novel cohesive beam model for the end-notched flexure (ENF) specimen.

Eng. *Fract. Mech*. 78 (17), 3017–3029 .

[76] Bennati, S., Fisicaro, P. and Valvo, P. (2013). An enhanced beam-theory model of the mixed-mode bending (MMB) test—Part I: Literature review and mechanical model. *Meccanica*, 48(2), pp.443-462.

[77] Levy, A. (1994). Separation at a circular interface under biaxial load. *Journal Of The Mechanics And Physics Of Solids*, *42*(7), 1087-1104. doi: 10.1016/0022-5096(94)90061-2

[78] Nguyen, C. and Levy, A. (2009). An exact theory of interfacial debonding in layered elastic composites. *International Journal of Solids and Structures*, 46(13), pp.2712-2723.

[79] Nguyen, C. and Levy, A. (2011). Mechanics of interface failure in the trilayer elastic composite. *International Journal of Solids and Structures*, 48(18), pp.2467-2484.

[80] Nguyen, C. and Levy, A. (2013). Cohesive fracture of plane orthotropic layers. *International Journal of Solids and Structures*, 50(9), pp.1266-1284.

[81] Xu, X.P., Needleman, A., 1993. "Void Nucleation by Inclusion Debonding in a Crystal Matrix," *Modeling and Simulation in Materials Science and Engineering* 1: 111–132.

[82] Carpinteri A. Post-peak and post-bifurcation analysis of cohesive crack propagation. *Engng Fract Mech* 1989;32:265 78.

[83] Reich R, Cervenka J, Saouma V. Merlin: a computational environment for 2d/3d discrete fracture analysis. In: Mang H, Bicanic N, de Borst R, editors. *Computational modeling of concrete structures. Swansea*: Pineridge press; 1994. p. 999 1008.

[84] Lofti HR, Shing PB. Embedded representation of fracture in concrete with mixed finite element. *Int J Numer Meth Engng* 1995;38:1307 25

[85] Mo€es N, Dolbow J, Belytschko T. A finite element method for crack growth without remeshing. *Int J Numer Meth Engng* 1999;46:131 50.

[86] Mikhlin, S. (1987). *Linear integral equations*. New York: Gordon and Breach.

[87] Boyce, W., DiPrima, R. and Meade, D. (n.d.). *Elementary differential equations and boundary value problems.*

[88] Xie, M. and Levy, A. (2007). Defect propagation at a circular interface. International *Journal of Fracture*, 144(1), pp.1-20.

[89] Wazwaz, A. (2011). *Linear and nonlinear integral equations*. Berlin: Springer.

[90] Levy, A.J. and Hardikar, K., "The Inclusion Pair Interaction Problem with Nonlinear Interface," *Journal of the Mechanics and Physics of Solids* 47, 1477-1508 (1999).

[91] Levy, A.J., "The Affect of Interfacial Shear on Cavity Formation at an Elastic Inhomogeneity," *Journal of Elasticity* 50, 49-85 (1998).

[92] Song, Y., & Levy, A. (2019). Exact Analysis of Mode-III Cohesive Fracture of a Cylindrical Bar in Torsion. *Journal Of Applied Mechanics*, 1. doi: 10.1115/1.4044384

[93] Levy, A.J. Journal of Elasticity (2001) 64: 131. https://doi.org/10.1023/A:1015274605075.

[94] Levy, A.J., "Bifurcation Phenomena in the Rigid Inclusion Power Law Matrix Composite Sphere," *International Journal of Solids and Structures*, 40, 2535-2561 (2003).

[95] Levy, A., & Hardikar, K. (1999). The inclusion pair interaction problem with non-linear interface. *Journal Of The Mechanics And Physics Of Solids*, *47*(7), 1477-1508. doi: 10.1016/s0022-5096(98)00115-x

[96] Song, Y., & Levy, A. (2020). Exact Analysis of Mode-III Cohesive Fracture in Layered Elastic Composites. *International Journal of Fracture,* (under review).

[97] Bertoldi, K., Bigoni, D., & Drugan, W. (2007). Structural interfaces in linear elasticity. Part I: Nonlocality and gradient approximations. *Journal Of The Mechanics And Physics Of Solids*, *55*(1), 1-34. doi: 10.1016/j.jmps.2006.06.004

[98] Bigoni, D., & Movchan, A. (2002). Statics and dynamics of structural interfaces in elasticity. *International Journal Of Solids And Structures*, *39*(19), 4843-4865. doi: 10.1016/s0020-7683(02)00416-x

[99] Nguyen, C., & Levy, A. (2010). The mechanics of atherosclerotic plaque rupture by inclusion/matrix interfacial decohesion. *Journal Of Biomechanics*, *43*(14), 2702-2708. doi: 10.1016/j.jbiomech.2010.06.012.

[100] Lurie, A., A. (2005). *Theory of Elasticity*. Berlin, Heidelberg: Springer-Verlag Berlin Heidelberg.

[101] Barber, J. (2010). *Elasticity*. Dordrecht: Springer Netherlands.

[102] Watson, G. (1966). *A treatise on the theory of Bessel functions*. Cambridge: Univ. Pr. Press, W. (2007).

[103] *Numerical Recipes 3rd Edition: The Art of Scientific Computing*. New York: Cambridge University Press.

[104] Koiter, W.T. and Benthem, J.P. 1973. "Asymptotic Approximations to Crack Problems," *Mechanics of Fracture*, G.C. Sih (ed.), Noordhoff: Leyden, vol. 1, pp. 131-178.

[105] Knauss, W. (1970). An observation of crack propagation in anti-plane shear. *International Journal of Fracture Mechanics*, 6(2).

[106] Erdogan, F., & Sih, G. (1963). On the Crack Extension in Plates Under Plane Loading and Transverse Shear. *Journal Of Basic Engineering,* 85(4), 519-525. doi: 10.1115/1.3656897

[107] Mitchell, D., Makabe, C., Anggit, M., Sueyoshi, T. and Yafuso, T. (2006). The Formation Mechanism of the Factory-Roof Pattern in a Torsional Fatigue Specimen with Circumferential Notch. *Journal of Testing and Evaluation*, 34(5), p.100101.

[108] Zehnder, A. and Zella, N. (2015). Spiral to flat fracture transition for notched rods under torsional loading. *International Journal of Fracture*, 195(1-2), pp.87-92.

[109] Snozzi, L. and Molinari, J. (2012). A cohesive element model for mixed mode loading with frictional contact capability. *International Journal for Numerical Methods in Engineering*, 93(5), pp.510-526.

[110] Sokolnikoff, I. (1987). *Mathematical theory of elasticity*. Malabar, Fla.: R.E. Krieger..

[111] Tsai, J., Patra, A. and Wetherhold, R. (2005). Finite element simulation of shaped ductile fiber pullout using a mixed cohesive zone/friction interface model. Composites Part A: *Applied Science and Manufacturing*, 36(6), pp.827-838.

[112] Corless, R.M., G.H. Gonnet, D.E.G. Hare, D.J. Jeffrey, and D.E. Knuth. (1996) On the Lambert W Function. *Advances in Computational Mathematics*, 5, 329–35

[113] Jin, Z., & Batra, R. (1996). Interface cracking between functionally graded coatings and a substrate under antiplane shear. *International Journal Of Engineering Science*, *34*(15), 1705-1716. doi: 10.1016/s0020-7225(96)00055-9

[114] Pollard, David D., Paul Segall, and Paul T. Delaney. (1982). Formation And Interpretation of Dilatant Echelon Cracks. Geological Society of America Bulletin, 93(12), 1291.

[115] Goldstein, R. and Osipenko, N. (2012). Fracture structure near a longitudinal shear macrorupture. Mechanics of Solids, 47(5), 505-516.

[116] Hull, D. (1995). The effect of mixed mode I/III on crack evolution in brittle solids. International Journal of Fracture, 70(1), 59-79.

[117] Kachanov, M. (1987). Elastic solids with many cracks: A simple method of analysis. *International Journal of Solids and Structures*, 23(1), pp.23-43.

[118] Kachanov, M. and Montagut, E. (1986). Interaction of a crack with certain microcrack arrays. *Engineering Fracture Mechanics*, 25(5-6), pp.625-636.

[119] Karihaloo, B. (1979). Fracture of solids containing arrays of cracks. *Engineering Fracture Mechanics*, 12(1), pp.49-77.

[120] Pham, K., & Ravi-Chandar, K. (2016). On the growth of cracks under mixed-mode I + III loading. *International Journal Of Fracture*, *199*(1), 105-134. doi: 10.1007/s10704-016-0098-6

[121] Pham, K., & Ravi-Chandar, K. (2017). The formation and growth of echelon cracks in brittle materials. *International Journal Of Fracture*, *206*(2), 229-244. doi: 10.1007/s10704-017-0212-4

[122] Sun, J., Xia, S., Moon, M., Oh, K., & Kim, K. (2013). Folding wrinkles of a thin film stiff layer on a soft substrate. *Proceedings Of The Royal Society A: Mathematical, Physical And Engineering Sciences*, *469*(2151), 20120742. doi: 10.1098/rspa.2012.0742

[123] Harper, P., & Hallett, S. (2010). A fatigue degradation law for cohesive interface elements – Development and application to composite materials. *International Journal Of Fatigue*, *32*(11), 1774-1787. doi: 10.1016/j.ijfatigue.2010.04.006

[124] Pan, K., Ni, Y., He, L., & Huang, R. (2014). Nonlinear analysis of compressed elastic thin films on elastic substrates: From wrinkling to buckle-delamination. *International Journal Of Solids And Structures*, *51*(21-22), 3715-3726. doi: 10.1016/j.ijsolstr.2014.07.005

[125] Pan, K., Ni, Y., He, L., & Huang, R. (2014). Nonlinear analysis of compressed elastic thin films on elastic substrates: From wrinkling to buckle-delamination. *International Journal Of Solids And Structures*, *51*(21-22), 3715-3726. doi: 10.1016/j.ijsolstr.2014.07.005

[126] Zhang, W., & Tabiei, A. (2018). Improvement of an Exponential Cohesive Zone Model for Fatigue Analysis. *Journal Of Failure Analysis And Prevention*, *18*(3), 607-618. doi: 10.1007/s11668-018-0434-4

[127] Li, H., Li, J., & Yuan, H. (2018). Application of a Cohesive Zone Model for Simulating Fatigue Crack Growth from Moderate to High ΔK Levels of Inconel 718. *International Journal Of Aerospace Engineering*, *2018*, 1-13. doi: 10.1155/2018/4048386

[128] Roe, K., & Siegmund, T. (2003). An irreversible cohesive zone model for interface fatigue crack growth simulation. *Engineering Fracture Mechanics*, *70*(2), 209-232. doi: 10.1016/s0013-7944(02)00034-6

Vita

Education:

Syracuse University 2014-2020

Ph.D., Mechanical and Aerospace Engineering

Dalian University of Technology (DUT) 2009-2014

B.S., Mechanical Engineering (Minor in English)

Publications

Song, Y., & Levy, A. (2019). Exact Analysis of Mode-III Cohesive Fracture of a Cylindrical Bar in Torsion. *Journal of Applied Mechanics*, doi: 10.1115/1.4044384

Song, Y., & Levy, A. J. (2016). Mode-III cohesive fracture of a cylindrical bar in torsion. *In Proceedings of the American Society for Composites - 31st Technical Conference*, ASC 2016 DEStech Publications Inc..

Luo, Y., Yang, C., Song, Y. and Wang, X. (2014). Stress Forming of Fine Metal Wire Based on Ultrasonic Vibration. *Applied Mechanics and Materials*, 599-601, pp.587-590.

Song, Y., & Levy, A. (2020) Exact Analysis of Mode-III Cohesive Fracture in Layered Elastic Composites. *International Journal of Fracture* (under review)